Using medical data to adjust flow boundary conditions in computational hemodynamics

Madalena Beirão da Veiga da Silva Dias

Thesis to obtain the Master of Science Degree in

Biomedical Engineering

Supervisors:
Prof. Jorge Filipe Duarte Tiago
Dra. Sílvia Aguiar Rosa

Examination Committee

Chairperson: Prof. João Miguel Raposo Sanches
Supervisor: Dra. Sílvia Aguiar Rosa
Member of the Committee: Prof. Telma Cotovio Guerra Santos

January 2021

Declaration

I declare that this document is an original work of my own authorship and that it fulfils all the requirements of the Code of Conduct and Good Practices of the Universidade de Lisboa.

Preface

The work presented in this thesis was performed at Instituto Superior Técnico (Lisbon, Portugal), during the period July 2019 - December 2020, under the supervision of Prof. Jorge Tiago and Dra. Sílvia Aguiar Rosa.

Resumo

A coarctação da aorta (CoA) é uma das cardiopatias congénitas mais comuns e consiste num estreitamento na aorta torácica proximal. Pode ser tratada por meio de cirurgia ou colocação de stent. Melhoramentos nas imagens médicas e em técnicas computacionais oferecem à comunidade científica uma oportunidade única de investigar doenças cardiovasculares, com os modelos de dinâmica de fluidos computacional (CFD) abrindo novas formas de estudar doenças cardiovasculares. Devido à complexidade do sistema cardiovascular, é comum modelar apenas a região de interesse e representar o restante da circulação por meio de condições de fronteira (CF), cuja escolha é crítica para a CFD, pois diferentes CF podem resultar em diferenças quantitativas nas soluções.

O objectivo deste trabalho foi desenvolver um método para ajustar o parâmetro da lei de Murray nas condições de fronteira, utilizando o método de optimização. Considerou-se o parâmetro da lei de Murray como o controle, e utilizou-se uma abordagem de primeiro discretizar e depois optimizar, para resolver numericamente o problema.

O método foi testado usando um conjunto de dados gerados *in-silico* e, em seguida, aplicada a uma geometria realista 3D representando uma CoA, usando dados específicos do paciente, para validação. Os resultados mostram pequenos erros no domínio, com erros absolutos < 1% e erros relativos <10%. Os erros relativos mais significativos encontram-se nas fronteiras supra-aórticas quando a CF atribuída é diferente nos dados *in-silico* e no problema com o control, apesar de o erro absoluto manter-se pequeno (1.5%). Para a aorta normal e CoA, os parâmetros da lei de Murray obtidos são diferentes dos encontrados na literatura, com maiores valores de parâmetros encontrados para CoA, o que pode ser explicado pelo comportamento do fluxo.

Este trabalho é a primeira etapa de desenvolvimento de um método para avaliação da anatomia e impacto no fluxo e circulação, e consequentemente entender a gravidade da doença, e também ajudar no planeamento cirurgico, inclusivamente na decisão de implantação de prótese endovascular.

Palavras-chave: sistema cardiovascular, coartação da aorta, dinâmica de fluidos computacional, condições de fronteira, lei de Murray, optimisação

Abstract

The aorta coarctation (CoA) is one of the most common congenital heart diseases (CHDs). It is defined by a narrowing in the proximal thoracic aorta and is treated through surgery or stent placement.

Advances in medical imaging and computational techniques provided the research community with a unique opportunity to investigate CHDs, with computational fluid dynamics (CFD) models opening new ways to understand cardiovascular pathologies. Due to the complexity of the cardiovascular system, it is common to model merely the region of interest and represent the remaining circulation through boundary conditions (BCs), whose choice is critical for CFD since different BCs could lead to quantitative differences in the solution.

This work presents a framework to adjust Murray's law BC, using an optimisation approach. Taking Murray's law parameter as the control, the approach uses a discretise-then-optimise methodology to numerically solve the control problem. The framework was tested using generated in-silico data sets and then applied to a realistic 3D geometry representing a CoA, using patient-specific data, for validation.

The results show small errors over the domain, with relative errors <10%. The largest relative errors were found in the supra-aortic outlets when different types of BCs were attributed in the in-silico data and in the controlled problem. For the normal aorta and CoA, the parameters obtained are different from those found in the literature, with higher parameter values found for the CoA, which can be explained by the flow behaviour.

This work was the first stage of developing a method that could help to analyse the anatomy and flow patterns in the CoA, and potentially evaluate the gravity of the disease, and assist the surgical planning, including the decision of the stent placement

Keywords: cardiovascular system, aortic coarctation, computational fluid dynamics, boundary conditions, Murray's law, optimisation

List of figures

List of tables

List of acronyms

AA – ascending aorta

BA – brachiocephalic artery

BAV – bicuspid aortic valve

BC(s) – boundary condition(s)

CAD – computer-aided design

CFD – computational fluid dynamics

CHD(s) – congenital heart disease(s)

CoA – coarctation of the aorta

CT – computed tomography

CVD(s) – cardiovascular disease(s)

DA – descending aorta

DICOM – digital imaging and communication in medicine

DO - discretise-then-optimize

EU – European Union

FSI – fluid-structure interaction

LCA – left common carotid artery

LSA – left subclavian artery

ML – Murray's law

MLBC(s) – Murray's law boundary condition(s)

MRI – magnetic resonance imaging

NS – Navier-Stokes

PC-MRI – phase-contrast magnetic resonance imaging

PDE(s) – partial difference equation(s)

ROI – region of interest

RTT – Reynolds transport theorem

SNS – Serviço Nacional de Saúde

SQP - sequential quadratic programming

TA – thoracic aorta

TF – traction-free

TFBC(s) – traction-free boundary condition(s)

WHO – World Health Organization

WSS – wall shear stress

Contents

1. Introduction

1.1. Motivation

Cardiovascular diseases (CVDs) are a category of heart and blood disorders, including coronary heart disease, cerebrovascular disease, peripheral arterial disease, rheumatic heart disease, congenital heart disease (CHD), deep vein thrombosis and pulmonary embolism. [1]

According to the World Health Organization (WHO), CVDs are the leading cause of death worldwide, representing a significant cause of morbidity. In 2016, an approximate 17.9 million people died from CVDs, which corresponds to 31% of all world deaths. Within the CVDs deaths, four out of five are due to heart attacks and strokes, and a third of all CVDs deaths occur in people under 70 years old. [1]

In Europe, in 2017, there were 11 million new cases of CVS which added up to the number of total cases to 49 million. CVDs reportedly caused 3.9 million deaths in the region, accounting for 45% of total deaths. CVDs are more prevalent among women, being the main cause of death in all countries except two, in Europe. CVDs could cost up to €210 billion to the European Union (EU) economy yearly [2]. According to the SNS (Serviço Nacional de Saúde), in 2017, 35 thousand Portuguese died with CVDs, representing a third of all deaths in the country. [3]

Congenital Heart Diseases (CHDs), a type of CVDs, correspond to the heart conditions or defects developed in the womb, meaning the condition is present from birth, and its prevalence is around 9 per 1000 new-borns. [4], [5] With the improvement of technology, and medical and surgical evolution, more than 90% of CHD individuals reach adulthood. The aorta coarctation (CoA) is a moderate CHD, defined by a narrowing in the proximal thoracic aorta, and can be treated through surgery or stent placement. It is one of most common CHD, with a prevalence of 3 cases per 10000 births. [6]

In the past decades while some CVDs behavioural risk factors have improved, such as smoking rates, others have worsened, such as eating habits, obesity prevalence, diabetes rates, levels of inactivity and alcohol consumption [1], [7]

On the positive side, many advancements in the diagnosis and treatment of these cardiovascular disorders have been made, but there is still a need for more effective, safe, and affordable therapies. Advances in vascular biology, biomechanics, medical imaging, and computational techniques provided the research community with a unique opportunity to investigate CVDs, with predictive mathematical models and simulations for computer-aided medicine opening new ways to understand the complexity of cardiovascular pathologies and their treatment as well as better surgical planning. These advances can reduce valuable time and financial cost and provide a safer environment compared to experimental studies. [8]–[10]

One of these advancements occurs in the Computational Fluid Dynamic (CFD) field, an area of mechanical engineering that uses numerical methods and algorithms to solve and analyse problems involving fluid flows, heat transfer and associated phenomena computer-based simulation. [9], [11].

Blood flow simulations using patient-specific imaging began by the end of 1990s. However, CFD in biomedical models is still lagging due to human body fluid behaviour's complexity. Including real data in the numerical blood flow simulations increases its complexity but allows for more realistic and accurate results. With the decreasing hardware costs, the improvement in computing times and CFD

technology have made CFD modelling a critical and reliable analysis component in blood flow numerical simulations. [11]–[15] Several studies recently showed the applicability of CFD, which can help understand the pathophysiology and the mechanism of the disease, assist in the preventative and therapeutic measures and understand the outcome of the CoA treatment.[16]–[21]

Nevertheless, performing a numerical simulation in the entire cardiovascular system tree is time-consuming and requires high computational costs. Hence, computational simulations are performed in specific regions of interest. The excluded sections of the cardiovascular system need to be considered using the appropriate inflow and outflow boundary conditions (BCs), which will describe physiological conditions (haemodynamic or structural) acting on those boundaries, replacing the removed part. BCs are an essential part of developing effective CFD and fluid-structure interaction (FSI) models since they are directly related to the simulation's accuracy. [10], [22], [23]

1.2. Objectives

This thesis aims to propose a methodology to automatically adjust Murray's law (ML) boundary conditions to patient-specific data, using an optimisation approach. The framework developed uses a variational approach which takes the ML parameter, in the supra-aortic outlets' boundary conditions, as the control. This approach uses a discretise-then-optimise methodology to solve the control problem numerically. The cost function to be minimised takes as the input the velocity obtained when generating an in-silico flow since patient-specific data was not available.

1.3. Thesis outline

This thesis contains five chapters. In Chapter 1, the motivations and objectives of this work are summarised. In Chapter 2, an overview of the cardiovascular system is given, including a brief insight of the aorta. The concepts of cardiovascular flows modelling, focusing on blood properties in the aorta and the several equations that govern the blood flow are clarified. Finally, a review of previous computational studies of blood flow focused on either boundary conditions or the variational approach, is presented. This work's methodology is explained in Chapter 3, which includes the numerical approximation and the numerical implementation, to develop the framework and its validation. In Chapter 4, numerical results obtained using the introduced methodology are presented and discussed and, ultimately, in Chapter 5, the conclusions concerning this work are drawn, and future work is proposed.

2. State of the art

In this chapter, an overview of the concepts relevant to this work and a summary of the research being done in the field of boundary conditions, for blood flow simulations and the variational approach, are given.

In Section 2.1, an introduction of the cardiovascular system physiology essential to the study of fluid dynamics is explained, emphasising the aorta anatomy and the aorta coarctation (CoA).

In Section 2.2, the mathematical concepts will be addressed starting by the blood flow characterisation, from a mechanical point of view; followed by the equations that modelled blood flow, namely the Navier-Stokes (NS), whose complete demonstration can be found in Annexe A, the Hagen-Poiseuille Law and Murray's Law. Additionally, the Womersley equation for pulsatile flow is addressed in Annexe B. Finally, at the end of this section, the boundary conditions will be reviewed, including the latest research being done in this field.

In Section 2.3, an overview of the optimisation approach is given.

2.1. Anatomy and physiology of the cardiovascular system

The cardiovascular system is composed of the heart and the network of blood vessels of the systemic and pulmonary circulation. Blood collects oxygen in the lungs and nutrients in the intestine and delivers them to the cells in all parts of the body. The blood in circulation removes cellular wastes and carbon dioxide from the cells for excretion through the kidneys and the lung, respectively. It maintains the visceral organs at a constant temperature through vasodilation and vasoconstriction. Another functionality of this system is protecting the body from infection and distributing heat accordingly.

The human heart is placed within the thoracic cavity, in the middle of the lungs in a space denominated the mediastinum. In the mediastinum, the heart is separated from the other mediastinal structures by the pericardium, a serous, inelastic membrane that restricts excessive dilation of the heart and can limit ventricular filling.

The heart comprises four chambers: two atria (singular: atrium) – a left and a right - in its upper portion and two ventricles – a left and a right - in the bottom portion. The atria act as receiving chambers and contract to push blood into the ventricles, which functions as the heart's primary pumping chambers. The right ventricle - a low-pressure pump - supplies the pulmonary circulation, while the left ventricle - a high-pressure pump - supplies the systemic circulation.

The wall that separates the right and left sides of the heart is known as the septum. This structure can be sub-divided into the interatrial septum, separating the atria, and the interventricular septum, separating the ventricles.

The heart contains four valves embedded in the fibrous skeleton of the heart. Each valve is found at the exit of each heart chamber. Valves are designated as mitral, aortic, tricuspid and pulmonary. On the left side of the heart, the mitral valve prevents blood from flowing back from the left ventricle to the left atrium, and the aortic valve prevents it from flowing from the aorta to the left ventricle. On the right side, the tricuspid valve prevents blood from flowing back from the right ventricle to the right atrium, and

the pulmonary valve prevents it from flowing from the root of the main pulmonary artery to the right ventricle.

Three layers compose the heart: the endocardium - a thin membrane that lines the heart's interior; the myocardium - the heart muscle and the thickest layer; and the epicardium - a slim layer on the surface of the heart. The myocardium consists of specialised muscle cells – the cardiomyocytes - that differ from other muscle cells in their inability to contract anaerobically (without oxygen), and higher fatigue resistance. The heart is continuously supplied by coronary vessels - vessels that supply the heart muscle and lie in the epicardium - with oxygen to function.

The blood flows in the body via a series of vessels: arteries, arterioles, capillaries, venules, and veins. Arteries carry blood from the heart to the rest of the body, and branch into smaller vessels – the arterioles - which branch into even thinner vessels – the capillaries. Capillaries join together to form small veins – the venules - which join together to form larger veins and eventually get back to the heart.

There are two linked circuits in the human circulation - the pulmonary and the systemic. The pulmonary circuit transports blood to and from the lungs, where it picks up oxygen and delivers carbon dioxide to be expelled from the body. On the other hand, the systemic circuit carries blood to and from all of the body's remaining tissues, where it delivers oxygen and removes carbon dioxide to be sent back to the pulmonary circulation. [24], [25]

At the beginning of the pulmonary circuit, the right ventricle pumps deoxygenated blood - known as venous blood – towards the lungs through the pulmonary trunk which bifurcates into the left and right pulmonary arteries. These two arteries branch multiple times before reaching the pulmonary capillaries, where the vessel walls are thin enough to allow gas exchange - carbon dioxide exits the blood and oxygen enters. Oxygenated blood – known as arterial blood - returning from the pulmonary capillaries passes through a series of vessels that join to form the pulmonary veins. The pulmonary veins conduct the arterial blood into the left atrium, which pumps the blood into the left ventricle, which in turn pumps the blood out of the heart towards the aorta, initialising the systemic circuit. [24], [25]

From the aorta, arterial blood flows through smaller arteries that branch into arterioles and finally to capillaries, where the exchange with the body's cells occurs. Oxygen and nutrients exit the systemic capillaries to be used by the cells in their metabolic processes. Carbon dioxide and waste products resulting from the metabolic process enter the bloodstream through the capillaries, making the blood more deficient in oxygen. The capillaries will unite to form venules, which will form even larger veins, which will flow into the two major systemic veins - the superior vena cava and the inferior vena cava. The blood in these two major systemic veins flows into the right atrium, where it is pumped into the right ventricle. The pulmonary circulation retakes place, as the following ventricle contraction imposes the next cycle. [26]

These two circulations – systemic and pulmonary - are coordinated by the cardiac cycle, which is the period that begins with the contraction of the atria and ends with the ventricular relaxation. The cardiac cycle lasts between 0.6 to 1 second, and it is comprised of the diastole and the systole. The diastole is the period when the myocardium is relaxing, as the ventricles fill with blood. On the other hand, the systole is the period when the myocardium contracts and the blood is ejected from the ventricle.

The cardiac cycle is pressure driven. It starts with all atria in diastole, allowing blood flow to enter passively from the superior and inferior vena cava into the right atrium, and from the pulmonary veins to the left atrium as the blood flows into the cavities the pressure increases. When this pressure surpasses the ventricles' pressure, the valves open (tricuspid in the right side and mitral in the left side), allowing the blood to flow to the ventricles. During the late diastole, the remaining blood in the atria is forced to flow from the atria to the ventricle, driven by the atria's depolarisation, which contracts the atrial muscles. Then, the ventricles start to contract (systole), increasing its internal pressure. When this pressure becomes higher than the arterial tree's pressure, the two semilunar valves open and the blood moves into the pulmonary trunk and the aorta (ventricular ejection phase). Following ventricular repolarisation (ventricular diastole), the ventricles begin to relax, driving the ventricular pressure down and starting the diastole phase again. [27]

Blood is a fluid connective tissue whose primary function is to deliver oxygen and nutrients and remove wastes from body cells. Other secondary functions include defence, distribution of heat, and maintenance of homeostasis.

Blood is formed of cellular elements that include erythrocytes, leukocytes and platelets. These cellular elements are suspended in an aqueous polymer solution - the plasma – to allow them to circulate through the body within the cardiovascular system. The plasma is composed $\sim$92 % water by weight and constitutes 55% of the blood volume. It contains electrolytes and organic molecules such as metabolites, hormones, enzymes, antibodies, and other proteins. Proteins made up 7% of its volume.

The erythrocytes are the most common cellular element, and they are estimated to make up about 25% of the total cells in the body. The main functions of erythrocytes are the collection of inhaled oxygen from the lungs and its transportation to the body's tissues, and then the collection of part of the carbon dioxide waste at the tissues and its transportation back to the lung, to be expelled from the body. Erythrocytes remain within the vascular network and are continuously generated by the bone marrow.

The leukocytes are a significant component of the body's defences against disease. They can leave the bloodstream to perform their defensive functions in the body's tissues. There are five types of leukocytes: neutrophils, lymphocytes, monocytes, eosinophils and basophils: Neutrophils (50–70% of all leukocytes) can phagocytise foreign cells, toxins and viruses; Lymphocytes (25–35%) play an essential role in the immune response by providing antigen-specific acquired immunity (immunological memory); Monocytes (3–9%) give rise to mature macrophages that reside in the tissues and defend the body against viruses and bacteria; Eosinophils (< 5%) phagocytise antigen-antibody complexes; and basophils (< 1%) release preformed granule-associated mediators, including histamine, serotonin, bradykinin, heparin and cytokines and newly generated mediators, such as prostaglandins and leukotrienes. [24], [25]

The last cellular element is the platelets, which are non-nucleated cells critical to hemostasis and the blood's coagulation. They secrete a variety of growth factors essential for growth and repair of tissue, particularly connective tissue. Once platelets enter the circulation, approximately one-third migrate to the spleen to be store for a future release if a rupture occurs in a blood vessel. They then become activated to perform their primary function, which is to limit blood loss. Platelets remain in circulation for about ten days until macrophages phagocytise them.

2.1.1. The aorta

The aorta is the primary and largest artery in the body, and its branches distribute blood to all tissues of the body. At the top of the left ventricle, the aorta originates at the semilunar aortic valve and descends to the abdominal region up to the aortic bifurcation. The aortic bifurcation is the point where the aorta splits into two smaller arteries - the two common iliac arteries, this usually occurs at the level of the fourth lumbar vertebra. [25], [26], [28]

Four regions can be identified in the aorta: the ascending aorta (AA), the aortic arch, the descending aorta (DA) and the abdominal aorta. The ascending aorta arises from the heart. The first branchings of the aorta are the left and right main coronary arteries; both supply the heart with nutrients and oxygen. The aortic arch gives rise to the brachiocephalic artery (BA), left common carotid artery (LCA), the left subclavian artery (LSA). The ascending aorta, the aortic arch and the descending aorta, curves over the heart and branches into arteries that supply the head, neck, and arms. The descending aorta, which goes through the diaphragm, can be split up into the thoracic aorta and the abdominal aorta. The distal end of the descending aorta is the abdominal aorta which begins at the diaphragm and forms the aortoiliac junction with left and right iliac arteries and its continuation. The majority of organs receive blood from branches of the abdominal aorta. [25], [26], [28]

Several congenital heart diseases (CHD) affect the aorta. One of them is the coarctation of the aorta (CoA), representing 10% of CHD cases. CoA occurs as a discrete stenosis, a narrowing, or as a long hypoplastic aortic (arch) segment, which causes increased blood pressure in the upper body and a decreased pressure in the lower body. [29], [30] CoA is usually located in the insertion of the ductus arteriosus (in very rare cases might occur ectopically in the ascending, descending or abdominal aorta). [5] CoA can be linked to other pathologies such as a bicuspid aortic valve (BAV). [31] It is considered a moderate complex CHD and can be treated surgically or using a stent placement, and it is reported to have successful outcomes. A long-term follow-up in 274 subjects subject to CoA repair, 50 years after surgery, reported that 207 (81%) were still alive. Nevertheless, despite successful treatments, there is decreased life-expectancy due to altered aortic hemodynamics. [32] Many researchers use CFD as a tool to understand the hemodynamics before and after CoA treatment. [17]–[21]

2.2. Modelling cardiovascular flows

2.2.1. Characterisation of the blood flow

A Newtonian viscous fluid is a fluid where the shear stress (τ) is linearly proportional to the strain rate (du/dy), with the proportionality constant (μ). [33]

$$\tau = \mu \, \frac{du}{dy} \tag{1}$$

On the other hand, fluids which do not exhibit this property are named Non-Newtonian fluids. They can be: pseudoplastic fluids (or shear-thinning fluids), which have a large dynamic viscosity at low shear rates and low dynamic viscosity at high shear rates; dilatant fluids (or shear-thickening fluids), where the shear viscosity increases as stress are applied [34]; or Bingham plastic fluids, which are fluids that

resist flowing, behaving as a rigid body until the shear stress reaches a threshold shear stress level. Once the fluid starts to flow, the shear stress becomes linearly proportional to the strain rate. [35]
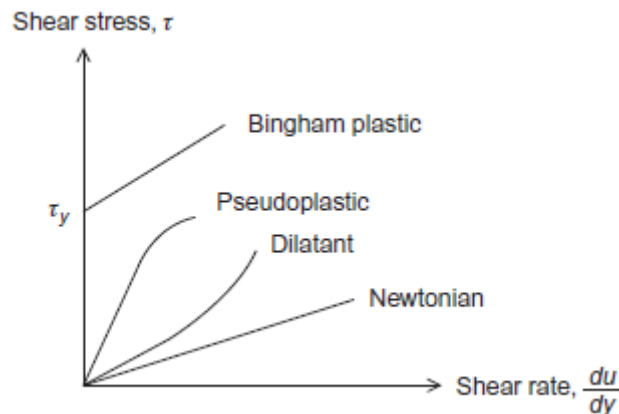
Figure 1: Relationship between shear stress and shear rate for Newtonian and non-Newtonian fluids. Newtonian fluids have a constant viscosity as a function of shear rate. Non-Newtonian fluids have a non-constant viscosity.

As seen in Section 2.1, blood is composed by erythrocytes. The high concentration of erythrocytes, when compared to the remaining formed elements, is thought to be the cause of their significant influence on the mechanical properties of blood. [24]

At low shear rates, blood can be considered a non-Newtonian fluid, while plasma by itself shows a nearly Newtonian behaviour. Consequently, blood must surpass initial yield stress to begin flowing. Once the initial yield stress is reached, the shear rate increases as blood's dynamic viscosity decreases. The non-Newtonian behaviour of blood can be explained by three phenomena that occur with the erythrocytes: their tendency to form a 3D microstructure formation at low shear rates, their deformability and their tendency to align, at high shear rates, with the flow field.

At lower shear rates, the behaviour is controlled by the effect of the 3D erythrocytes microstructure formations on the flow and their ability to deform and store energy. At moderate to high shear rates, these erythrocytes are dispersed in the plasma, and the properties of the blood start being influenced by their deformability and their tendency to align with the flow field, forming layers in the flow. At high shear rates, whole blood behaves like a Newtonian fluid with a constant coefficient of viscosity.

Fluids can also be characterised as compressible or incompressible – a fluid is compressible if its density can vary throughout the flow, for example, due to geometry considerations or thermal consideration. Gases, for instance, are highly compressible. Incompressible fluids have minor changes in density throughout the flow - this suggests that pressure and temperature do not impact density. Blood is considered to be incompressible since, in the human body, core body temperature is constant at 37°C. Therefore, there is no need to account for blood density changes when modelling blood flow through internal organs. [33]

Flows can be characterised based on their regime as laminar or turbulent flows. While laminar regions are characterised by smooth transitions inflow, turbulent regions have random time-dependent fluctuations in fluid properties such as velocity, acceleration, and viscosity. In laminar flow, usually, there

is no mixing of fluid laminae. On the other hand, due to random fluctuations in turbulent flows, there is a mixing of fluid laminae. This mixing of fluid laminae results in a large increase in shear stress since there is a transfer of mass and energy between laminae. Turbulent flows typically have non-zero vorticity. Blood flow in the circulatory system is usually laminar, although in the ascending aorta it can destabilise briefly during the deceleration phase of late systole; however, this period is generally too quick for the flow to become fully turbulent. Nevertheless, certain disease conditions can alter this condition and produce turbulent blood flow - for example, the CoA. The blood is turbulent in a coarctation zone since its narrowing creates a flow jet with high velocity. [24], [36], [37]

2.2.1.1. Dimensionless numbers

There are two types of dimensionless numbers. The first type helps to scale parameters and to simplify numerical analysis. Combining multiple variables into one reduces their number and the amount of experimental data required to make correlations of the physical phenomena. [38] These dimensionless numbers do not change the fluid properties or analysis of the problem. The second type helps understand the correlation between some parameters or forces in the phenomenon and re-scaling. [39] Since this type of dimensionless number provides essential information about the flow conditions, many different dimensionless quantities have been developed. Two of them will be discussed in the next sections: the Reynolds number (Re) and the Womersley number (W_o).

2.2.1.1.1. Reynolds number

The Reynolds number (Re) is a dimensionless number that is important to nearly all biofluid mechanics flows since it allows predicting the flow's behaviour - whether it is laminar or turbulent. It correlates the overall inertial forces that govern the flow with the viscous forces that impede the flow.

The Re parameter naturally arises in the non-dimensionalisation of the NS equations and physically corresponds to the ratio of inertial forces to viscous forces providing a measure of which forces dominate changes to a fluid's velocity. The Re in an internal flow of mean sectional velocity (U) within a pipe or vessel of characteristic diameter (D) is given by:

$$Re = \frac{inertial\ forces}{viscous\ forces} = \frac{\rho U D}{\mu} \tag{2}$$

where μ is the fluid's dynamic viscosity and ρ the fluid's density.

Re gives a measure of flow characteristics. In a flow with a large Re, for example, inertial forces dominate over viscous forces. This dominance naturally leads to considering this number as the key parameter that identifies the transition of the flow to turbulence. One the one hand, if viscous effects are dominants, the fluid will be characterised by a smooth – laminar – flow and the Re is low; on the other hand, if inertial effects are dominant, blood flow is turbulent, which is represented by large values of Re.

The transition between laminar and turbulent flows is difficult to define since many properties affect the overall laminar versus turbulent flow properties. Under most conditions, for some sources, the flow regime is typically divided into three cases based on the value of the Re: for Re <2300 the flow is

laminar; for Re >4000 the flow is turbulent, and for Re ≈2300–4000, the flow falls in an intermediate regime. Other sources assume Re <2100 for laminar and Re >4200 for turbulent. [39], [40]

The Re is difficult to quantify in the aorta, since the parameters stated in the equation (2), vary from region to region in the aorta, as the diameter changes, and in the cardiac cycle timing, since the velocity changes. For example, in the peak velocity, Re in the aorta is calculated as $Re \approx 5250$, while if considering a mean velocity, $Re \approx 1050$. This value means that in systole, the inertial effects are much more important than viscous effects since $Re \approx 5250 \gg 1$. At this point in the cycle, some flow instabilities may occur at the exit of the aortic valve. In fact, in this region, the Re may reach the threshold value for turbulence, but only for the instantaneous period of the cardiac cycle that corresponds to the systolic peak, which does not give enough time for a fully turbulent flow to develop. Therefore, the viscous effects are still predominant for mean velocity, but the flow can be considered laminar [11].

2.2.1.1.2. Womersley number

Another significant dimensionless number for the blood is the Womersley number (W_o), especially when considering unsteady flows. Unsteady flows that have regular oscillating time-dependent components are considered pulsatile. W_o corresponds to the ratio between the fluid's oscillatory inertia and the viscous momentum. While the oscillatory inertia corresponds to the measure of the forces governing the pulsatile flow, the viscous forces are a measure of the fluids' overall resistance to changes in its velocity. W_o can be defined as:

$$W_o = \frac{oscillatory\ inertia}{viscous\ forces} = \frac{D}{2}\sqrt{\frac{2\pi}{\nu T}} \tag{3}$$

Where $\nu = \mu/\rho$ is the kinematic viscosity and T is usually taken as the fundamental period of the oscillatory flow. If a fluid has a low W_o, it is characterised by having virtually no phase difference between the pulsatile pressure waveform, driving the flow, and the pulsatile velocity waveform linked to the flow. For this type of flows, means the viscosity is much higher than unsteady inertial forces, describing a quasi-steady flow. In higher W_o, a phase difference between the pressure and velocity waveform can be detected. This is driven by the inertial of the fluid resisting the pressure waveform changes, and because the pulse frequency is relatively high. This case represents the situations where the unsteady inertial effects become predominant, describing an unsteady flow.

The estimated range of W_o for the aorta is between 16 and 30, a considerably high value, therefore describing the blood flow as unsteady. This description predicts a flattened velocity profile, where inertial forces are dominant in the centre of the vessel, and viscous effects are dominant near the boundary. Experimental studies also report that the average W_o monotonically decreases from the ascending (16.1) towards the descending aorta (12.0), which is consistent with the dependency of the W_o on the vessel diameter and velocity.[24], [36], [41]

2.2.2. Governing equations for blood flow

2.2.2.1. Navier-Stokes equations

The NS equations are a system of partial differential equations, named after Claude-Louis Navier (1785 – 1836), a French mathematician [42], and George Gabriel Stokes (1819-1903), an Irish mathematician [43], that describes the motion of a fluid. [44] These equations - both in their full and simplified forms - describe the physics of multiple physics phenomena in the area of engineering and science. They are one of the most important fluid dynamics concepts, since their solution, with the appropriate boundary conditions and initial values, predicts the fluid velocity and its pressure in every geometry. Nevertheless, the NS equations complexity only allows a limited number of analytical solutions. Whilst the exact solution can be reasonably easy to solve for simple cases, the existence and smoothness of the general solution of the three-dimensional NS equations have not been proven. Clay Mathematics Institute has considered it one of the seven most important problems in mathematics, with its solution or counterexample worth US$1 million. [45].

The NS equations for a fluid with constant density ρ in a domain Ω, are stated as:

$$\begin{cases} \dfrac{\partial u}{\partial t} - \nabla \cdot \left[v\left(\nabla u + \nabla u^T\right) \right] + \left(u \cdot \nabla\right)u + \nabla p = f & \text{in } \Omega \\ \nabla \cdot u = 0 & \text{in } \Omega \end{cases} \tag{4}$$

With u being the velocity of the fluid, p the pressure divided by the density (designated as pressure), v is the kinematic viscosity ($v = \mu/\rho$) and f a forcing term per unit of mass.

The first equation in the system (4) corresponds to the conservation of linear momentum, which is the formulation of Newton's second law of motion for flow, where net force equals mass times acceleration. The conservation of linear momentum implies that the rate of change of linear momentum must be equal to the net force acting on a set of fluid particles [46]. The second equation in the system (4) corresponds to the conservation of mass, also designated as the continuity equation, which implies that the rate of accumulation of mass inside a control volume and the net rate of outflow of the amount of mass across the control surface is zero [36], [44]. The term $(u \cdot \nabla)u$ in the first equation of system (4) corresponds to the convective term and $-\nabla \cdot [v(\nabla u + \nabla u^T)]$ to the diffusive term.

System (4) can be simplified accordingly to the assumptions made to the fluid. One assumption that can be considered is that the fluid is isothermal (temperature is constant), and therefore, the energy equation, which is temperature-dependent, can be decoupled [47]. Additionally, for example, if the fluid is incompressible, v is constant, and the diffusive term reduces to:

$$\nabla \cdot \left[v\left(\nabla u + \nabla u^T\right) \right] = v\Delta u + \Delta div\, u = v\Delta u \tag{5}$$

Taking into consideration the equation (5), the system (4) can be re-written into the incompressible NS equations:

$$\begin{cases} \dfrac{\partial u}{\partial t} - v\Delta u + \left(u \bullet \nabla\right)u + \nabla p = f & \text{in } \Omega \\ \nabla \cdot u = 0 & \text{in } \Omega \end{cases} \tag{6}$$

Moreover, if the fluid is considered stationary the term $\frac{\partial u}{\partial t}$ disappears, and the system becomes:

$$\begin{cases} -v\Delta u + (u \cdot \nabla)u + \nabla p = f & \text{in } \Omega \\ \nabla \cdot u = 0 & \text{in } \Omega \end{cases} \tag{7}$$

In this system (7), considering a three-dimensional incompressible flow, there are four unknowns – the velocity components $u = (u_1, u_2, u_3)$, and the pressure p - and four equations - one from conservation of mass, which is a scalar equation, and three from the conservation of momentum equation, which is a vector equation. These equations are coupled, meaning that some of the variables appear in all four equations; the system of differential equations must therefore be solved simultaneously for all four unknowns. Besides, to solve the system, the appropriate initial conditions and boundary conditions (such as inlets, outlets, and walls) need to be defined. The full derivation of the NS equations can be found in Annexe A.

2.2.2.2. Hagen-Poiseuille's law

The Hagen-Poiseuille's law was experimentally derived independently by Jean Léonard Marie Poiseuille, a French physicist and physiologist, in 1838 and Gotthilf Heinrich Ludwig Hagen, a German hydraulic engineer, in 1839. George Stokes, an Anglo-Irish physicist and mathematician, provided the theoretical derivation in 1845. [39], [48], [49]

This law derives the relationship between the pressure drop (P) across a cylindrical tube, the volumetric flow rate (Q) – the volume of fluid which passes per unit time - through the tube and its respective radius (r) in an incompressible and Newtonian fluid in laminar flow.

To derive this law, the fluid within the tube is assumed to have constant viscosity (μ) and a uniform circular cross-sectional area (A) over its length (L), and the entry (P_R) and exit (P_L) pressures are such that $P_R > P_L$ since there is a pressure difference that would compel the fluid inside to flow from left to right.
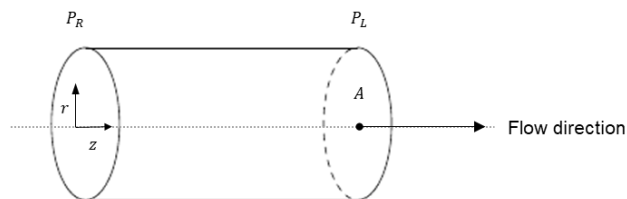
Figure 2: Flow in a tube with a uniform circular cross-sectional area A and length L, with constant viscosity μ, the pressure of entry P_R and the pressure of exit P_L.

To obtain the Hagen-Poiseuille law, the fluid's velocity (solved from the NS equations) is integrated over the blood vessel area. Considering μ is the viscosity, ρ is the density, r, θ and z are the radial coordinates, v is the velocity, v_x is the velocity component, and P is the pressure. When moving across the tube, the fluid will have a velocity called v_z, a radial velocity v_r and an angular velocity v_θ.

To simplify the Navier-Stokes equations, the tube is considered long, and the flow is steady so that the conditions of flow do not change with the distance along the tube nor with the time. There is no gravity which cancels the term ρg; no radial forces are acting on the fluid ($v_r = 0$) and the fluid is not spinning ($v_\theta = 0$).

The NS become:

$$\frac{1}{\mu}\frac{\partial P}{\partial z} = \frac{1}{r}\frac{d}{dr}\left(r\frac{\partial v_z}{\partial r}\right) \tag{8}$$

Since $\partial v_z/\partial z = 0$, considering the continuity equation, and pressure gradients in the radial ($\partial P_r/\partial r = 0$) and angular directions are zero ($\partial P_\theta/\partial\theta = 0$).

Assuming the pressure drop to be $P_R - P_L$ and multiplying both sides by the radius, equation (8):

$$\frac{1}{\mu}\frac{\partial P}{\partial z} = \frac{1}{r}\frac{d}{dr}\left(r\frac{\partial v_z}{\partial r}\right)$$

$$r\frac{1}{\mu}\frac{P_R - P_L}{L} = \frac{d}{dr}\left(r\frac{\partial v_z}{\partial r}\right)$$

$$r\frac{\partial v_z}{\partial r} = \frac{P_R - P_L}{L}\frac{r^2}{2\mu} + C_1 \tag{9}$$

$$v_z(r) = \frac{P_R - P_L}{L}\frac{r^2}{4\mu} + C_1\ln(r) + C_2$$

To define C_1 and C_2 the boundary conditions will be considered. For $r = 0$, v_z is finite and therefore C_1 needs to be 0. For $r = R$ and a no-slip wall, $v_z = 0$ and $C_2 = -\frac{P_R - P_L}{L}R^2$.

Therefore,

$$v_z(r) = \frac{P_R - P_L}{4\mu L}\left(r^2 - R^2\right) = \frac{\Delta P}{4\mu L}(R^2 - r^2) = \frac{\Delta P R^2}{4\mu L}\left(1 - \frac{r^2}{R^2}\right) \tag{10}$$

The equation (10) shows, for $0 < r < R$, the laminar flow has a parabolic profile from zero at the wall ($r = R$) to a maximum achieved in the centre of the tube ($r = 0$), which can be seen in Figure 3.
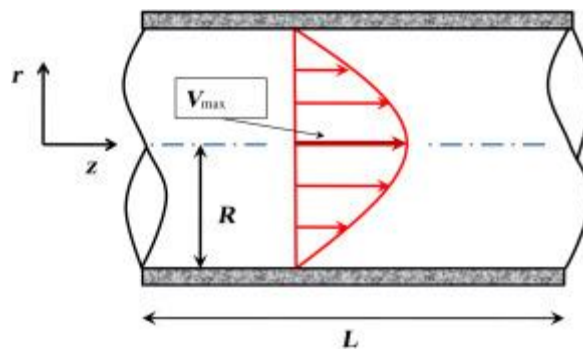
Figure 3: Longitudinal view of a tube with a laminar flow and parabolic velocity profile.

As a result,

$$V_{max} = \frac{\Delta P R^2}{4\mu L} \tag{11}$$

Considering the definition of average velocity ($\bar{V}$) in cylindrical coordinates and Equation (11), the average velocity in the tube is given by:

$$\bar{V} = \frac{V_{max}}{2} \tag{12}$$

Assuming the volumetric flow rate (Q) as the cross-section area (A) multiplied by the average velocity in the tube and that $A = \pi R^2$, the flow rate is given by:

12

$$Q = \bar{V}A \tag{13}$$

$$Q = \frac{1}{2}\frac{\Delta PR^2}{4\mu L} A = \frac{\Delta PR^4 \pi}{8\mu L} \Leftrightarrow \Delta P = \frac{8\mu L}{R^4 \pi} = QR_e \tag{14}$$

The equation (14) is known as the Hagen-Poiseuille's law and resistance (R_e) can be defined as:

$$R_e = \frac{8\mu L}{\pi R^4} \tag{15}$$

Hagen-Poiseuille's law demonstrates that small changes in the vessel radius cause substantial changes in the flow rate by significantly altering the resistance. It also demonstrates that the blood vessel radius does not significantly change to increase/decrease flow to a region with abnormal tissue oxygenation. If the flow rate did not change rapidly with small vessel diameter changes, then blood vessels would need to dilate or constrict significantly to counterbalance the tissue oxygenation level changes. This reaction would be associated with enormous energy demands that would effectively deplete the smooth muscle cells of energy, and then they would not be able to respond to changes in the tissue needs shortly. Instead, the biological system is designed so that minimal energy is required for profound blood flow changes. [33], [36]

Nevertheless, the flow when entering the tube does not show a parabolic profile, like the one seen in the equation (10). The fluid particles in contact with the surface of the tube have velocity equal to zero, due to a non-slip condition, which is being discussed in Section 2.2.3.1. As a result of friction with the particles in the surface layer, fluid particles in adjacent layers see their velocity slow down. To keep the mass flow rate through the tube constant, the velocity in the centre of the tube needs to increase to compensate for the one in the surface of the tube being zero. Consequently, a velocity gradient develops along the tube.

When the fluid contacts with the surface, viscous effects become important, and a boundary layer develops along the tube. The boundary layer is the area where the effects of the viscous shearing forces caused by fluid viscosity are felt. This development occurs at the expense of a shrinking inviscid flow region and concludes with the boundary layer merging at the centreline. The region from the tube inlet to the point at which the boundary layer merges at the centreline is called the hydrodynamic entrance region, and the length of this region is called the hydrodynamic entry length L_{entr}. Following this merger, viscous effects extend over the entire cross-section velocity profile is fully developed and remains unchanged. [40], [50]

In laminar flow, the velocity profile in a fully developed region is parabolic, and the hydrodynamic entry length is given by:

$$L_{entr} = 0.05 R_e D \tag{16}$$

In turbulent flow, the velocity profile in a fully developed region is flatter, caused by turbulent mixing in the radial direction. The entry length, given by the equation (17), is shorter for these flow types since they have a weaker dependence on Reynolds number.

$$L_{entr} = 1.359 DR_e^{1/4} \tag{17}$$

In several engineering fields, the tubes used are considerably longer than L_{entr}. Therefore, the flow is always assumed fully developed for the entire length of the tube. In small tubes, artificial entries need to be created so that the flow can become fully developed at the tube. [40], [50].

The unsteady counterpart of the Hagen-Poiseuille's Law for a constant in space and sinusoidal-in-time pressure drop is the 2D Womersley solution discussed in Annexe B. [26] [51]

2.2.2.3. Murray's law

Murray's law (ML), developed by Cecil D. Murray in 1926, explains the relationship between the radius of a vessel immediately upstream from a branch point (parent vessel) and the radii of the vessel immediately downstream (daughter vessel). When an artery of radius R_k branches into η arteries of radius R_{k+1}, then $R_k^3 = \eta R_{k+1}^3$.

Murray's derivation of this relationship assumes that there are two energy contributions to the cost of maintaining blood flow in part of a vessel: (a) the energy required to surpass viscous drag in a fluid obeying Poiseuille's law, and (b) the metabolic energy needed to keep the blood's volume and vessel tissue involved in the flow. Both energy contributions are related to the radius of the vessel, in a way that, the larger the radius, the smaller the power, P_f, required for the fluid to flow, but the larger the power, P_m, needed for the metabolic maintenance of the blood's volume and vessel tissue. For the sum of these powers to be minimised, $P_t = P_f + P_m$, the vessel cannot be too large nor too small.

If gravitation and kinetic energy terms can be neglected, a Newtonian fluid exhibits a volumetric flow rate, f, which is linearly proportional to the pressure difference, p, to which is subjected: $f = cp$, where c in a conductance coefficient.

In cylindrical tubes, the conductance is proportional to r^4.

$$c = \frac{\pi r^4}{8 \eta l} \tag{18}$$

where η is the viscosity of the fluid, and l is the length of the tube. For a tube of unit length ($l = 1$), and assuming $a = 8\eta/\pi$,

$$af = pr^4 \leftrightarrow p = afr^{-4} \tag{19}$$

The power to maintain the flow is

$$P_f = p \times f = af^2 r^{-4} \tag{20}$$

Offsetting this is the metabolic power requirement P_m, which increases linearly with the volume of the blood and vessel:

$$P_m = m \bullet volume = mr^2 l \tag{21}$$

Where m is a metabolic coefficient. For unit length ($l = 1$) and $b = \pi m$,

$$P_m = br^2 \tag{22}$$

The power required is then,

$$P_t = P_f + P_m = af^2 r^{-4} + br^2 \tag{23}$$

For a specified value of the flow (f), the power P_t depends only upon the radius of the vessel (r), and P_t as a function of r will be minimised by that value of r where $dP_t/dr = 0$ and $d^2 P_t/dr^2 > 0$.

To find the optimum value of r:

$$\frac{dP_t}{dr} = \frac{d\left(af^2 r^{-4} + br^2\right)}{dr} = -4af^2 r^{-5} + 2br = 0 \tag{24}$$

$$\frac{d^2 P_t}{dr^2} = \frac{d\left(-4af^2 r^{-5} + 2br\right)}{dr} = 20af^2 r^{-6} + 2b = 0 \tag{25}$$

Since a, b, f, and r are always positive, $d^2 P_t/dr^2 = 20af^2 r^{-6} + 2b$ is positive, and any point for which $dP_t/dr = 0$ is a minimum. Hence a minimum for P_t exists where:

$$-4af^2 r^{-5} + 2br = 0 \Leftrightarrow f^2 = \frac{b}{2a} r^6 \leftrightarrow f = kr^3 \tag{26}$$

$$k = \sqrt{\frac{b}{2a}} \tag{27}$$

The new coefficient k depends only upon a and b, so that if the fluid's viscosity, the blood's metabolism and vessel tissue remain constant throughout all vascular system, k remains constant as well. This equation expresses for any vessel minimising energy requirements, a constant relation between flow and vessel radius. Moreover, if it applies to every vessel in a branching system, then it can be applied to a sum of such vessels. The flows need to be added in one side and the radii's cubes in the other.

$$\sum f = \sum kr^3 = k \sum r^3 \tag{28}$$

Murray himself concentrated upon the application of his equation to individual branching of parent to daughter's vessels. [52]

$$r_0^3 = kr_1^3 + kr_2^3 \leftrightarrow r_0^3 = r_1^3 + r_2^3 \tag{29}$$

ML will usually apply only to branching systems for which the original assumptions leading to the law are valid. These assumptions are: (a) that the system is arranged to minimise energy output, and (b) that the energy output is that which results from two terms associated with (i) Poiseuille flow, where energy output is proportional to $f^2 r^{-4}$; and (ii) volume of the system, where maintenance energy is proportional to r^2.

Murray's law can be considered a good approximation in the cardiovascular systems where the cost is minimised when vessel radii are consistent with Murray's Law. [40], [52]–[54]

2.2.3. Boundary conditions estimation

When studying the hemodynamics of blood flow in the circulatory system, two significant aspects affect the numerical simulation – the geometry of the domain of interest and the boundary conditions (BCs). To reduce the complexity of the blood flow simulation is essential to truncate the domain of interest by creating artificial sections, which separate the region of interest for the simulation from the remaining part of the circulatory system. The choice of BCs on artificial boundaries is an essential issue for fluid dynamic computations since different BCs could lead to quantitative differences in the solution. [22], [24], [55]–[57]

In this work's case, the thoracic aorta is not isolated within the cardiovascular system. This system is comprised of a closed network with millions of vessels interacting with each other, which makes a hemodynamic analysis very complicated. Therefore, there is a need to separate the upstream and

downstream vasculature of the aorta and provide those BCs with an appropriate equivalent. The BCs, together with viscosity and density values, and the initial values, are the CFD simulation input parameters to solve the NS equations.

The proximal boundary is the section closest to the heart along the direction of the blood flow, denominated as the inlet. In contrast, the distal boundaries are named outlets and correspond to the outflow. The walls are also considered a boundary condition. [24], [58], [59]

2.2.3.1. Wall boundary conditions

Since the vessel wall encloses the fluid, it is a boundary that needs constraints. When the purpose of a study is to compare different scenarios, e.g. different BCs, rather than quantifying any hemodynamic parameter, researchers often assume the rigid-wall model [60]. This model is considered a valid assumption [61].

The most-used boundary condition in the wall is the no-slip condition, which states that for fluid in contact with a solid wall, the fluid's velocity must equal that of the wall. Fluid particles adjacent to the wall adhere to its surface and move at the same velocity as the wall.

$$\vec{V}_{fluid} = \vec{V}_{wall} \tag{30}$$

This assumption is proved to work well for viscous fluids. [62]

2.2.3.2. Inlet boundary conditions

The inlet BC should truncate the upstream vasculature of the vessel of interest and, in the case of the aorta, the inlet is a crucial part of the hemodynamic simulation once it represents the impulsion by the heart to the system. The inlet's complete characterisation would require having a velocity profile, with a vector field, or a time-dependent flow rate or pressure waveform, obtained from non-invasive in vivo measurements, which are not always available.

Generally, only averaged data are available, i.e., mean velocity or mean pressure, instead of a vector condition, which is not sufficient for a complete mathematical formulation. Therefore, alternative formulations for the inflow BC need to be developed. They need to reflect the physics of the data available and permit the formulation of a meaningful and well-posed mathematical problem.

The simplest alternatives include idealised velocity profiles supported by clinical evidence and often prescribed as the inlet BC. For example, a flat-velocity profile, an idealised profile of uniform velocity, is used because in vivo measurements have demonstrated that the ascending aorta's velocity profile, distal to the aortic valve, is essentially flat. Another example is the fully-developed profile BCs. These BCs can be achieved either numerically by applying a velocity profile based on an equation, or by affixing a flow extension to the inlet and outlets, which allows the flow to be fully developed by the time it reaches the right inlet or outlet, thus creating a more realistic simulation [23]. This velocity profiles can also be translated into a volumetric flow rate (Q) when the section's diameter is known since the flow rate is equal to the measured average velocity times the area of the section where the velocity profile was measured. The prescription of flow rate is quite common and straightforward to achieve. The drawback is that the constant profile may be a crude approximation that introduces local errors in the

numerical results. Again, a strategy to mitigate this error relies on introducing artificial extensions of the physical domain so that the errors are localised out of the region of interest. [55]

Womersley profiles are also applied velocity profiles, especially in unsteady flow simulations. When time-varying velocity data obtained with PC-MRI (Phase-contrast Magnetic Resonance imaging) or ultrasound are available, an average velocity can be prescribed at the inlet.

Nevertheless, it was found that the selection of inlet velocity conditions significantly affects only the flow region close to the inlet of the aorta. [63]

2.2.3.3. Outlet boundary conditions

Despite the importance of the inlet BC, the solutions to the NS equations in large arteries are also highly dependent on the imposed outlet BCs to represent the downstream vascular systems. It has been demonstrated that velocity and pressure fields of the same computational domain can change significantly depending on the choice of outflow BC. [64]–[66]

Since it is impossible, without geometric scale reduction, to trace all branches downstream the aorta (as they branch and connect to smaller vessels and also because they would make the computational domain too big), the computational models need to be truncated by an artificial boundary condition at some point. The further the boundary is from the vessel of interest, the less influence it will have on local results, but the larger the computational domain will be.

The BCs at the distal part of the vessel's branches of interest can be handled using many different strategies. Nevertheless, the most appropriate boundary conditions is still a topic of debate and continuous development, mainly due to the lack of patient-specific measurements for outflow, and while at the inlet, the missing data can be replaced by adapting literature data to the case of interest, at the outlets is more challenging due to the morphological variation. [67]

Strategies similar to the ones applied in the inlet are common. The fully developed flow is applied when patient-specific flow measurements are unavailable, and constant fractions of the inflowing flow are prescribed as outflow BCs. Since ML states that flow in a vessel is proportional to the diameter of the vessel lumen cubed, this leads to the application of 'flow splits' (also known as 'flow percentage' or 'flow ratio'), referring to the percentage of flow assigned to an outlet boundary dependent on the inlet flow rate. In general terms, in the MLBC, the flow split assigned to an outlet boundary is given with respect to the inlet flow rate, as:

$$\frac{Q_{out}}{Q_{in}} = \frac{D_{out}^{3}}{D_{in}^{3}} \tag{31}$$

where Q_{out} is the flow rate in the outlet, Q_{in} the flow rate in the inlet, D_{out} the diameter of the outlet, and D_{in} the diameter in the inlet. Therefore, the MLBC, in a generic outlet, is given by:

$$Q_{out} = Q_{in} \times \left(\frac{D_{out}^{3}}{D_{in}^{3}} \right) \tag{32}$$

ML can substitute or be used in conjunction with incomplete in vivo data. [68], [69] For example, [70] attributed ML to the BCs, changing its exponent from 3 to values between 2.25 and 2.75 and concluded that it did not affect the NS solutions. Furthermore, [71] assuming the widely-accepted low wall shear

stress theory of Caro, found that ML applied to BCs returns the most physiologically accurate results compared to in vivo data.

Another example of prescribed BCs, still common amongst the cardiovascular research community, is the traction-free (TF), one of the simplest BC to apply in a simulation, consists in assigning a zero pressure to the boundary, similar to assuming the vessel is cut and exposed to atmospheric conditions, thus neglects the resistive effects of downstream vessels.

New BCs have been developed to better model the interaction between the computational domain and the downstream vasculature, by coupling the domain with simple models such as resistance, impedance, lumped parameter, or distributed models, to capture the resistance and compliance effects of the proximal and distal vessels in the arterial tree from corresponding outlets. The three-element Windkessel has become one of the most widely used and accepted lumped parameter model of the circulatory system as it tends to produce realistic aortic pressures and flow [72]. This model attempts to capture the resistances of the proximal and distal arteries of the boundary and the downstream vessels' capacitance. These resistance and capacitance values are calculated using the values of measured blood pressure and flow rates. [71] Obtaining these values is complex mainly due to practical difficulties in acquiring pressure and flow data of all required sites, or the measurement data available is insufficient for accurately estimating these model parameters. The three-element Windkessel boundary condition is used in the latest CFD-based cardiovascular research to date. [22], [55], [73], [74]

Another approach observed in the literature is using the variational approach using data assimilation to obtain more accurate boundary conditions and other flow metrics. Variational approaches, which consists of varying a defined number of parameters to minimise a cost function, have been used successfully as a strategy to take advantage of real data measurements. The variational approach allows for increasing the accuracy of numerical simulations. [75] Data Assimilation techniques correspond to real data inclusion in the numerical blood flow simulations, allowing for more realistic and accurate results.

A variational data assimilation approach where velocity measurements included noise, was firstly studied by [75]. The goal was to use the sparse data with noise to obtain an accurate approximation of the blood flow in vessels to predict medical relevant physical metrics. The authors used a DO approach to minimise the misfit between the recovered velocity field and the data. They concluded that the noise affects the accuracy of the solution and the efficiency of the simulation.

For example, [8] solved a variational data assimilation problem to numerically reconstruct the blood flow circulation inside a real artery, deformed by a saccular aneurysm. The authors proposed a weighted cost function to recover both the velocity and the wall shear stress profiles. This weighted function was considered non-typical since it included WSS data information. A discretise-then-optimise (DO) approach, which consists of first discretising the optimal control problem and then solve the finite-dimensional optimisation problem resulting from the discretisation, was used to obtain the numerical solution.

Another example can be observed in [76], where the authors presented a fully automatic approach to recover boundary conditions and locations of the vessel wall, given a rough initial guess and the velocity at some cross-section, affected by noise. The method was used to minimise the uncertainty derived

from the boundary conditions choice and geometry, including noise and low resolution. The method showed to be useful as an unsupervised method to choose ow boundary conditions and identify a more accurate definition of the geometry no-slip walls.

A different DO approach was developed by [77], consisting of a variational data assimilation approach based on a Dirichlet boundary control problem, where the control was an entirely unknown velocity profile. This method was applied in a realistic model of a brain aneurysm. In this case study, due to the lack of real velocity measurements, in silico profiles were generated to supply the required data. The results showed that this data assimilation approach improved the accuracy of specific solutions obtained using an idealised laminar profile, even when noise is included.

Finally, in the case of [78], the authors proposed a sequential methodology to identify the corresponding boundary support parameters, such as stiffness parameters, using patient image data. They conclude that the resulting computational effectiveness of the complete estimation sequential method is comparable to that of a direct simulation. This method was validated in a patient-specific thoracic aorta, where the estimation of the boundary support parameters proved successful.

Nevertheless, as seen, a variational DA approach based on Murray's law boundary conditions has not been developed. Also, in the literature, the use of in-silico data can be seen, when real data is not available, and the inclusion of noise to simulate the medical devices errors.

2.3. Optimisation

As seen in the previous section, many authors chose the discretise-then-optimise approach for the variational problem. It is an approach to solve optimal control problems involving PDEs, challenging to solve due to their size and complexity. It transforms the original continuous problem into a standard optimisation problem by discretising the system completely. The fully discretised optimisation problem, typically large and sparse, can be solved by optimisation solvers. This method allows additional constraints and bounds when compared to optimise-then-discretise approach. [79]

Optimisation is an important tool in the analysis of physical systems. The formulation of an optimisation problem begins by identifying the objective, a quantitative measure of the system's performance being studied, which depends on certain characteristics of the system – the variables or parameters. The optimisation problem consists of, therefore, finding the parameters that optimise the objective. These parameters might be subject to constraints, or bounds, depending on the problem and system being studied. Constraints allow the optimisation algorithm to avoid suggesting an infeasible solution. [80]

The optimisation consists of the minimisation or maximisation of a function subjected to constraints (or not) on its parameters, and it is given by:

$$\min_{x \in \mathbb{R}^n} \quad f(x) \qquad \text{subject to} \quad \begin{array}{l} c_i(x) = 0 \quad i \in \mathrm{E} \\ c_i(x) \geq 0 \quad i \in \Upsilon \end{array} \qquad (33)$$

Where x is the vector of the parameters; f is the objective function – a scalar function of x that will be minimised or maximised; c_i are constraint functions - scalar functions of x that define certain equations and inequalities that x must satisfy – with E and Υ as their sets of indices, for equality and inequality, respectively. [80], [81]

Once all parameters and respective constraints are identified, and the objective defined, an optimisation algorithm is used to obtain the solutions. [80] An algorithm primarily used, and available in COMSOL Multiphysics® is the SNOPT (Sparse Nonlinear Optimizer) algorithm, which was initially based on the code developed by Philip E. Gill of the University of California San Diego, Walter Murray and Michael A. Saunders of Stanford University.

SNPOT allows for the objective function to have any form, and for any constraint to be applied. The algorithm minimises a linear or nonlinear function, subject to sparse constraints (linear or nonlinear) and bounds on the variables. It is an appropriate algorithm for large-scale linear and quadratic programming and linearly constrained optimisation and general nonlinear programs. [82], [83]

SNOPT uses a sequential quadratic programming (SQP) algorithm, which has proven reliable and efficient. The searching directions are found from the QP subproblems that minimise a quadratic model of the Lagrangian function subject to linearised constraints. An augmented Lagrangian merit function is reduced along each search direction to ensure convergence from any starting point. SNOPT uses a smooth augmented Lagrangian merit function and makes explicit provision for infeasibility in the original problem and QP problems. It is designed for problems with many thousands of constraints and variables but a moderate number of degrees of freedom. [82], [83] The algorithm described applies to constrained optimisation problems in the form NP

$$
\min_{x \in \mathbb{R}^n} \quad f_0(x) \qquad \text{subject to } l \le \begin{pmatrix} x \\ f(x) \\ A_L(x) \end{pmatrix} \le u \tag{34}
$$

Where x is an n-vector of parameters, l is a constant lower bound, u is a constant upper bound, $f_0(x)$ is a smooth scalar objective function, $f(x)$ is a vector of smooth nonlinear constraint functions $f_i(x)$ and A_L is a sparse matrix. Note that $f_0(x)$ in this case, is minimised but could be maximised. The first derivatives (gradients) of $f_0(x)$ and $f_i(x)$ should be known and it is given by the user. When only some of the gradients are known, SNOPT uses finite differences to estimate the unknown ones. Upper and lower bounds need to be specified for all variables and constraints. The jth constraint may be defined as equality by setting $l_j = u_j$. However, ff certain bounds do not exist, the associated elements of l or u may be set to special values treated as $-\infty$ or $+\infty$. Free variables and free constraints have both bounds infinite. [82], [83]

3. Methods

In this chapter, the methodology used to achieve the objectives of this work is described. As stated in Section 1.2, this thesis aims to automatically adjust Murray's Law boundary condition (MLBC) using real data. For that, this thesis can be split into two parts – one where a framework to obtain the adjusted parameters was developed, using a model of a "normal" aorta and in-silico data, and one where this framework was tested using a model of an aorta with coarctation and patient-specific data.

In the first part, Section 3.1 and Section 3.2, an aorta developed and studied by [84], was used to create a framework where the parameters of Murray's law (ML) were automatically adjusted, depending on the "real" data to be adjusted and the boundary conditions provided, using an optimisation study in COMSOL Multhiphysics®. This framework consists of the solution of two problems – the forward problem, where the in-silico data was generated to replicate real patient-specific information, and the controlled problem, where the parameters were adjusted.

In Section 3.1, the mathematical model and the definition of both problems are described, including the discretization methods and their implementation. Section 3.2 contains an overview of the implementation using COMSOL Multhiphysics®, including the adaptations made in the model of [84], the mesh convergence studies and the post-processing tools used.

For the second part, Section 3.3, a new model was developed of an aorta with a coarctation to validate our method, where real data from the patient was used. This section includes the domain's development, including the process from data acquisition to the final processing in COMSOL Multhiphysics®, and the mathematical model used.

3.1. Numerical approximation

3.1.1. Mathematical model and problem definition

The first part of this work involved the solution of two problems – the forward problem and the controlled problem. The forward problem was used to generate different datasets of in-silico data. In order to test the developed methodology in different "real" blood flow conditions, and driven that the lack of patient-specific data available is recurrent [85], [86], different blood flow datasets were generated in the same aorta model where the optimisation tool was applied. The generated in-silico data mimics real data and allowed testing the framework in different situations, thus understanding the capabilities of the methodology chosen.

The controlled problem consisted of using a variational approach to adjust ML exponent – here designated as a parameter – that fitted better the in-silico data generated in the forward problem.

The study of blood flow in the vascular system is complex; therefore, simplifying assumptions are needed. In both problems, the forward and the controlled, blood was modelled as a stationary, incompressible, laminar, homogeneous and Newtonian fluid with a constant density (ρ_{blood}) of 1060 kg/m^3 [22], [87]–[89], and constant viscosity (μ_{blood}) of 0.004 Pa.s [22], [90]–[92]. The assumption of Newtonian is only possible because our domain is a large artery. If the shear rates were as low as those

seen for small arteries and capillaries, the assumption could not be made. Blood was also considered to be isothermal with a constant temperature of 37°C, the average body temperature.

The three-dimension computational domain represents the upper part of a patient-specific aorta - designated as the thoracic aorta. Due to the complexity of the circulatory system, the domain was truncated by three planar surfaces: one at the entrance of the ascending aorta, to define the inlet; one in the intersection of the arteries brachiocephalic artery, left common carotid artery and left subclavian artery with the aortic arch, to define the supra-aortic outlets; and one in the middle of the thorax, to define the descendent aorta outlet. See Figure 4.

We can categorize the different portions of the boundary $\partial\Omega$ that constitute the domain of this analysis as:

1. Aortic Wall (Γ_{wall}) representing the physical wall of the artery
2. Aorta inlet (Γ_{in}) representing the main inflow section
3. Aorta outlets (Γ_{out}) representing the set of non-connected outlet sections which include the descending aorta (Γ_{DA}) outlet, the brachiocephalic artery (Γ_{BA}) outlet, the left common carotid artery (Γ_{LCA}) outlet, and the left subclavian artery (Γ_{LSA}) outlet.

$$\Gamma_{out} = \Gamma_{DA} \cup \Gamma_{BA} \cup \Gamma_{LCA} \cup \Gamma_{LSA}$$

$$\partial\Omega = \Gamma_{wall} \cup \Gamma_{in} \cup \Gamma_{out} = \Gamma_{wall} \cup \Gamma_{inlet} \cup \Gamma_{DA} \cup \Gamma_{BA} \cup \Gamma_{LCA} \cup \Gamma_{LSA}$$

4. The domain is divided into two by a virtual outlet, in the xy-plane, which will be used as an optimisation baseline (S_{obs}).
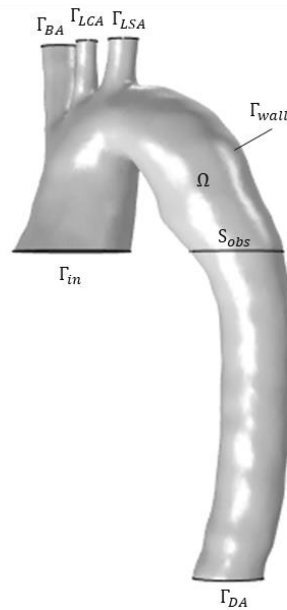
Figure 4: Domain of the numerical model with respective artificial boundaries – inlet, outlet and wall, and the optimisation simulation section.

Under the previous assumptions, blood flow can be described using the Navier-Stokes (NS) equations [93], and the interaction with the vessel wall will not be considered, since it is a stationary model [77]. As seen in Section 2.2.2.1, the stationary NS equations for an incompressible fluid is:

$$\begin{cases} -\upsilon\Delta u + (u\cdot\nabla)u + \nabla p = f & \text{in } \Omega \\ \nabla \cdot u = 0 & \text{in } \Omega \end{cases} \tag{35}$$

Where u is the fluid velocity, p is the pressure divided by density, f is the body forces, ρ is the density of the fluid, μ is the dynamic viscosity, and ν is the kinematic viscosity ($\nu = \mu/\rho$).

The wall was considered a rigid surface with a no-slip condition, which means the velocity of the elements of the wall was set to zero, which translates by:

$$u = 0 \tag{36}$$

At the inlet, a flow rate boundary condition (BC) was imposed. Base on work from [84], the maximum velocity (V_{max}) and the correspondent area of the cross-section where the velocity was measured, (A_{in}) were obtained. With equation (13) together with (12), the flow rate at the inlet (Q_{in}) is given by:

$$Q_{in} = V_{mean} \times A_{in} = \frac{V_{max}}{2} \times A_{in} \tag{37}$$

At the outlet in the descendent aorta (Γ_{DA}), the BC imposed was a traction-free boundary condition (TFBC); this condition assumes that the normal stresses at the boundary, which are approximately equal to the pressure, are zero. The tangential stress component is also set to 0 Pa; therefore, the expression used to apply this boundary condition was:

$$\left[-pI + \mu \left(\nabla u + (\nabla u)^T \right) \right] n = -P_0 n \tag{38}$$

where $P_0 = 0$.

This BC is considered a 'do-nothing' approach, which gave fewer restrictions to the model when adjusting the ML parameter and simplifying the simulation.

The inlet and outlet DA BCs were set to be the same at the forward and the controlled problem. On the other hand, the BCs at the supra-aortic outlets were changed accordingly to the type of in-silico data being generated and the controlled test being performed.

In sum, two types of BCs were attributed in the supra-aortic outlets: TFBC, where the condition imposed was (38), and MLBC. ML, as seen in Section 2.2.2.3, imposes the energy minimization principle for blood supply. The flow rate in each branch (Qi) is, therefore, calculated by:

$$Q_i = \left(\frac{D_i}{D_{in}} \right)^\alpha \times Q_{in} \tag{39}$$

Where Q_{in} is the inflow given by (37). D_{in} is the diameter of the inlet, D_i is the diameter of the branch i, with $i \in (BA, LCA, LSA)$, and p is the exponent of the MLBC. Applying (39) to each supra-aortic outlet:

$$Q_{BA} = Q_{in} \times \left(\frac{D_{BA}}{D_{in}} \right)^\alpha = (V_{mean} \times A_{in}) \times \left(\frac{D_{BA}}{D_{in}} \right)^\alpha \tag{40}$$

$$Q_{LCA} = Q_{in} \times \left(\frac{D_{LCA}}{D_{in}} \right)^\alpha = (V_{mean} \times A_{in}) \times \left(\frac{D_{LCA}}{D_{in}} \right)^\alpha \tag{41}$$

$$Q_{LSA} = Q_{in} \times \left(\frac{D_{LSA}}{D_{in}} \right)^\alpha = (V_{mean} \times A_{in}) \times \left(\frac{D_{LSA}}{D_{in}} \right)^\alpha \tag{42}$$

The diameters in each outlet were calculated assuming circular branches, using the area of each cross-section. The parameter α is what will distinguish the forward problem from the controlled problem. When

attributing MLBC, in the forward problem, the parameter was considered $\alpha = 3$, as stated in the literature [94], in the controlled problem, the parameter α was used as the value to be optimized.

The detailed characterization of the boundary conditions, for the forward and the controlled problem, can be found in Section 3.1.1.1 and Section 3.1.1.2, respectively.

3.1.1.1. Forward problem

Three different datasets (Data A, Data B and Data C) were generated using different combinations of BCs in the supra-aortic outlets, while the outlet DA and the inlet BCs were given by (38) and (37), respectively. The BCs attributed to the supra-aortic outlets are summarized in Table 1.

Table 1: Boundary conditions attributed to the inlet, the outlet DA and the supra-aortic outlets (BA, LCA and LSA) in the forward problem.

Test	Inlet	Outlet DA	Outlet BA	Outlet LCA	Outlet LSA
Data A	▲	●	▲	▲	▲
Data B	▲	●	▲	●	▲
Data C	▲	●	●	●	●

●   TFBC

▲ $Q_i = (V_{mean} * A_{in}) * \left(\dfrac{D_i}{D_{in}}\right)^3 , i \in (in, BA, LCA, LSA)$

The forward problem consists of solving the equation (35), using the boundary conditions above described.

3.1.1.2. Controlled problem

As explained at the beginning of Section 3.1.1, the only variation between tests, in the controlled problem, was the BCs applied to the supra-aortic outlets. Using the forward problem data as the data to be adjusted, each test was given of combination of different boundary conditions attributed to each supra-aortic outlet. For each in-silico data set, either one control optimising a single parameter (α_1) common to all outlets (A_1, B_1 and C_1) or three controls optimising a different parameter $(\alpha_1, \alpha_2, \alpha_3)$ in each outlet (A_3, B_3, C_3), was attributed. For Data B an additional test (B_1^{LCA}) was done, where the only outlet with an MLBC with an adjustable parameter (α_1) was outlet LCA, while the remaining outlets were given $\alpha = 3$. In Table 2, the summary of each BC applied to each test is stated.

Table 2: Boundary conditions attributed to the supra-aortic outlets (BA, LCA and LSA) in the controlled problem.

Test	Forward Problem	Inlet	Outlet DA	Outlet BA	Outlet LCA	Outlet LSA
A_1	Data A	▲	●	α_1	α_1	α_1
A_3	Data A	▲	●	α_1	α_2	α_3
B_1^{LCA}	Data B	▲	●	▲	α_1	▲
B_1	Data B	▲	●	α_1	α_1	α_1
B_3	Data B	▲	●	α_1	α_2	α_3
C_1	Data C	▲	●	α_1	α_1	α_1
C_3	Data C	▲	●	α_1	α_2	α_3

α_x $\qquad Q_i = (V_{mean} * A_{in}) * \left(\dfrac{D_i}{D_{in}}\right)^{\alpha_x}, i \in (BA, LCA, LSA)$

● $\quad$ TFBC

▲ $\quad Q_i = (V_{mean} * A_{in}) * \left(\dfrac{D_i}{D_{in}}\right)^{3}, i \in (in, BA, LCA, LSA)$

As seen in Section 2.3, an optimisation problem parameter always needs an initial value, and sometimes might need bounds, for example, due to physical constraints. In the preliminary studies, using coarser meshes, the bounded interval was [1,4], with the lower bound as the initial value. A solution was obtained for all tests. To reduce computational time, as the mesh was refined, the bounded interval was adapted and can be consulted in Table 3.

Table 3: Parameters initial values, lower bound and upper bound for each optimisation test, in the controlled problem.

Test	α_1			α_2			α_3		
	Initial Value	Lower Bound (low_1)	Upper Bound (up_1)	Initial Value	Lower Bound (low_2)	Upper Bound (up_2)	Initial Value	Lower Bound (low_3)	Upper Bound (up_3)
A_1	2	2	4		-			-	
A_3	2	2	4	2	2	4	2	2	4
B_1^{LCA}	1	1	4		-			-	
B_1	1.5	1.5	3.5		-			-	
B_3	1.5	1.5	3.5	1.5	1.5	3.5	1.5	1.5	3.5
C_1	1	1	3		-			-	
C_3	1	1	3	1	1	3	1	1	3

The controlled problem consisted of looking at the parameter α_x such that the following cost function:

$$f_{\cos t}(U) = \int\limits_{S_{obs}} \left(\|u\| - \|u_d\|\right)^2 dx \tag{43}$$

will be minimised. Here u corresponds to the solution of the NS for the controlled problem, and u_d represents the solution of the NS for the forward problem, both at S_{obs}. u is subjected to the parameters obtained and their respective bounds.

3.1.2. Numerical discretization of the Navier-Stokes equations

When coupling the stationary NS equations for incompressible fluids, stated in (35), with the appropriate boundary conditions referent to the domain given in Section 3.1.1 (Figure 4), the resulting system of equations is:

$$\begin{cases} -\upsilon\Delta u + u\cdot\nabla u + \nabla p = 0 & \text{in }\Omega \\ \nabla\cdot u = 0 & \text{in }\Omega \\ u = 0 & \text{on }\Gamma_{wall} \\ \int_{\Gamma_{in}} \overrightarrow{u_{avg}^{in}} \cdot (-\vec{n})\, ds = Q_{in} & \text{on }\Gamma_{in} \\ \upsilon\partial_n u - pn = 0 & \text{on }\Gamma_{DA} \\ \int_{\Gamma_{BA}^{ext}} \overrightarrow{u_{avg}^{BA}} \bullet (\vec{n})\, ds = Q_{BA} & \text{on }\Gamma_{BA} \\ \int_{\Gamma_{LCA}^{ext}} \overrightarrow{u_{avg}^{LCA}} \bullet (\vec{n})\, ds = Q_{LCA} & \text{on }\Gamma_{LCA} \\ \int_{\Gamma_{LSA}^{ext}} \overrightarrow{u_{avg}^{LSA}} \bullet (\vec{n})\, ds = Q_{LSA} & \text{on }\Gamma_{LSA} \end{cases} \tag{44}$$

In system (44), since the body forces are neglected, $f = 0$. The density and viscosity are represented by ρ_{blood} and μ_{blood}, respectively, and its values were defined in the previous section. Also, when implementing laminar flow BCs, geometric extensions are going to be considered. The BCs are then implemented as $u = \overrightarrow{u_{avg}^i} \cdot \vec{n}$, $i \in (BA, LCA, LSA, \text{in})$. Refer to Section 2.2.2.2, for a better understanding of the laminar flow hypothesis.

The NS equations, described here, are a partial differential equations (PDEs) system which is too complex to be solved analytically, in the patient-specific anatomic domain, like the one presented in Section 2.2.2.1. Therefore, it needs to be approximated by the finite element method (FEM).

The FEM is a numerical technique that provides approximate solutions to PDEs. In short, the method reduces a problem defined in a domain of interest to find a solution in a finite number of points by subdividing the domain into smaller regions – a geometric element. To fully characterize a finite element besides the geometric element, the degree of interpolation and the interpolation nodes in the element needs to be fixed. The basis functions used to approximate the solution are defined in terms of nodal values. With this, a continuous problem is transformed into a discrete finite element problem with unknown nodal values.

The Galerkin approach is often used for the finite element formulation [95]. In this approach, first, the weak formulation is constructed by multiplying both sides of the first equation in the system (44) by a weight function $v \in V$, and both sides of the second equation in the system (44) by $q \in Q$, and integrating by parts in the domain Ω, obtaining:

$$\begin{cases} \upsilon\int_{\Omega} \nabla u \cdot \nabla v + \int_{\Omega} (u \cdot \nabla) u \cdot v - \int_{\Omega} p(\nabla \cdot v) = 0 \\ \int_{\Omega} (\nabla \cdot u) \cdot q = 0 \end{cases} \tag{45}$$

Where $\forall\, v \in \{\, v \in H^1(\Omega) : v = 0 \text{ on } \partial s\backslash\Gamma_{DA}\}$ and considering the boundary conditions on Γ_{DA}, and $q \in L^2(\Omega)$. To discretise the problem in (45) using the FEM, the subspaces $V_h \subset H^1(\Omega)$ and $Q_h \subset L^2(\Omega)$ are considered, with finite dimensions $\dim(V_h) = N_u$ and $\dim(Q_h) = N_p$, respectively. Assuming V_h and Q_h

represent spaces of Lagrange type finite elements, associated with a partition τ_h of Ω. Therefore, the dimensions N_u and N_p tend to infinity when h tends to zero. A map between the nodes describing τ_h and the basis functions with dimensions both V_h and Q_h can be defined.

The system (45) can be re-written as:

$$\begin{cases} \upsilon \int_\Omega \nabla u_h \cdot \nabla v_h + \int_\Omega (u_h \cdot \nabla) u_h \cdot v_h - \int_\Omega p(\nabla \cdot v_h) = 0 \\ \int_\Omega (\nabla \cdot u_h) \cdot q_h = 0 \end{cases} \tag{46}$$

By applying the Galerkin method, two basis of V_h and Q_h are introduced, with elements ϕ_j and ψ_k, respectively. The approximation of the v and p variables are given by (47), where u_h and p_h are the unknown coefficients:

$$u \approx u_h = \sum_{j=1}^{N_u} u_j \phi_j \in V_h \quad p \approx p_h = \sum_{k=1}^{N_p} p_k \psi_k \in Q_h \tag{47}$$

Substituting (47) into the system (46), the equivalent system is obtained:

$$\begin{cases} \upsilon \int_\Omega \nabla u_h \cdot \nabla \phi_j + \int_\Omega (u_h \cdot \nabla) u_h \cdot \phi_j - \int_\Omega p(\nabla \cdot \phi_j) = 0 \\ \int_\Omega (\nabla \cdot u_h) \cdot \psi_k = 0 \end{cases} \tag{48}$$

Where $j = 1, 2, \ldots, N_u$ and $k = 1, 2, 3, \ldots, N_p$.

Once the space discretization is concluded, the system of algebraic equations is formed in the form:

$$\begin{cases} A U + B^T P + N(U) = 0 \\ B U = 0 \end{cases} \tag{49}$$

Where U is the matrix $(N_u \times 1)$ of the unknows coefficients u_h, and P is the matrix $(N_p \times 1)$ of the unknows coefficients p_h, AU is the discretised form of diffusion term, where $A_{ij} = \int_\Omega \nabla \phi_i \cdot \nabla \phi_j$ $N(u)$ is the discretised form of nonlinear convection, $B^T P$ is the discretised pressure term, and BU is the discretised form of the divergence of U, where $B_{ij} = \int_\Omega \nabla \phi_i \cdot \nabla \psi_j$ [95]–[98]. An example of the full derivation of the FEM for a 1D problem can be found in Annexe C.

3.1.3. The solution to the controlled problem

As seen in Section 3.1.1.2, a cost function is being minimised to obtain the parameters α_x in the MLBCs. Therefore, the system (44) needs to be adjusted, to include the parameters α_x to be adjusted and the bounds they are subjected.

$$
\begin{cases}
-\upsilon\Delta u + u \cdot \nabla u + \nabla p = 0 & \text{in } \Omega \\
\nabla \cdot u = 0 & \text{in } \Omega \\
u = 0 & \text{on } \Gamma_{wall} \\
\int_{\Gamma_{in}} \overrightarrow{u_{avg}^{in}} \cdot (-\vec{n})\, ds = Q_{in} & \text{on } \Gamma_{in} \\
\upsilon\partial_n u - pn = 0 & \text{on } \Gamma_{DA} \\
\int_{\Gamma_{BA}^{ext}} \overrightarrow{u_{avg}^{BA}} \cdot (\vec{n})\, ds = Q_{BA}(\alpha_1) & \text{on } \Gamma_{BA},\ low_1 < \alpha_1 < up_1 \\
\int_{\Gamma_{LCA}^{ext}} \overrightarrow{u_{avg}^{LCA}} \cdot (\vec{n})\, ds = Q_{LCA}(\alpha_2) & \text{on } \Gamma_{LCA},\ low_2 < \alpha_2 < up_2 \\
\int_{\Gamma_{LSA}^{ext}} \overrightarrow{u_{avg}^{LSA}} \cdot (\vec{n})\, ds = Q_{LSA}(\alpha_3) & \text{on } \Gamma_{LSA},\ low_3 < \alpha_3 < up_3
\end{cases}
\tag{50}
$$

where α_x are the parameters to be obtained with the minimised cost function, and the low_x and the up_x with $x \in [1,3]$ are the lower and upper bound, respectively, for each parameter.

For this problem, not only these NS equations need to be discretised (as in the previous section) but the cost function in (43). A discretise-then-optimize (DO) approach will be used to solve both (43) and (50), which consists of first discretizing the optimal control problem and then solving the optimisation problem, resulting from the discretization. Beginning by discretizing the cost functional $f_0(U)$ given by (43).

$$
f_{\cos t}(u) = \int_{S_{obs}} \left(\|\vec{u}\| - \|\overrightarrow{u_d}\| \right)^2 dx = \int_{S_{obs}} \left(\|\vec{u}\|^2 - 2\langle \vec{u}, \vec{u}_d \rangle + \|\vec{u}_d\| \right) dx
\tag{51}
$$

Since the solution of the forward problem $(\vec{u}_d)$ and the solution of the controlled problem $(\vec{u})$ can be approximated as:

$$
\vec{u} \approx \vec{u}_h = \sum_i^{N_u} u_i \vec{\phi}_i \quad \vec{u}_d \approx \vec{u}_{d_h} = \sum_i^{N_o} u_{d_i} \vec{\phi}_i
\tag{52}
$$

Equation (51) becomes:

$$
\begin{aligned}
f_0(U) &= \int_{S_{obs}} \left\langle \sum_i u_i \phi_i, \sum_j u_j \phi_j \right\rangle dx - 2\int_{S_{obs}} \left\langle \sum_i u_i \phi_i, \sum_j u_{d_j} \phi_j \right\rangle dx + \int_{S_{obs}} \left\langle \sum_i u_{d_i} \phi_i, \sum_j u_{d_j} \phi_j \right\rangle dx \\
&= \sum_i \sum_j u_i u_j \int_{S_{obs}} \langle \phi_i, \phi_j \rangle dx - 2\sum_i \sum_j u_i u_{d_j} \int_{S_{obs}} \langle \phi_i, \phi_j \rangle dx + \sum_i \sum_j u_{d_i} u_{d_j} \int_{S_{obs}} \langle \phi_i, \phi_j \rangle dx
\end{aligned}
$$

$$
f_0(U) = U^T M U - 2 U^T M U_d + U_D^T M U_D
\tag{53}
$$

Where $\|\cdot\|$ is the norm induced by the inner product $(\cdot,\cdot)_M$ and M is symmetric $N_u \times N_o$ matrix where each element is given by:

$$
mij = \int_{S_{obs}} \phi_i \phi_j\, dx,\ i = 1,2,\ldots,N_u,\ j = 1,2,\ldots,N_o
\tag{54}
$$

The discrete problem can be stated as:

$$\text{minimise} \quad f_0(U)$$

$$\text{subject to} \quad F(U, \alpha_1, \alpha_2, \alpha_3) = 0 \quad \text{where} \quad \begin{array}{l} low_1 < \alpha_1 < up_1 \\ low_2 < \alpha_2 < up_2 \\ low_3 < \alpha_3 < up_3 \end{array} \qquad (55)$$

Where F is the discretization of the NS equations, seen in (50), taking into consideration the parameters α_x and its respective bounds.

3.2. Numerical implementation

The numerical approximation was implemented and solved using the software COMSOL Multiphysics®. COMSOL Multhiphysics® is a general-purpose simulation software for modelling designs, devices, and processes in all fields of engineering, manufacturing, and scientific research. COMSOL Multhiphysics® allows conventional physics-based user interfaces and coupled systems of partial differential equations (PDEs) and the junction of workflows from different engineering fields such as mechanical, fluid, acoustics, and chemical [99].

The COMSOL Multhiphysics® interface is organized as a tree-structure where the model is built by adding and editing nodes to the default model tree. All the nodes in the default model tree are top-level parent nodes. When right-clicking the parent nodes, the child nodes (sub-nodes) to add to the tree appear. Each node has its *Settings* window, where all the features and properties can be adjusted.

A model tree always starts with a root node (which is labelled as File_Name.mph) which branches into a *Global* node and a *Results* node.

The *Global* node, in its turn, has two sub-nodes: *Definitions*, where the parameters, variables, functions, and couplings that can be used through the entire model tree are defined, and *Materials*, which is a repository of material properties that can be referenced in all other nodes of a model [99].

The *Results* node is where the solution obtained from the simulation is stored, and the tools for post-processing the data can be found. The *Results* node initially branches into five sub-nodes: *Data Sets*, which contains the list of solutions to work with; *Derived Values*, where the values to be calculated or extracted, from the solution, are defined; *Tables*, where the output of the derived values and other results generated by queries that monitor the solution while the simulation is running are stored; *Export*, where the numerical data in the form of tables, images or animations to be exported to external files, is defined; And finally, the *Reports* sub-node, which contains reports about the model, that can be generated automatically or custom based. Additional Plot Group sub-nodes can be added to these five default sub-nodes, where the graphs to be displayed in the *Graphics* window or the *Plot* windows can be characterised. Some of these may be created automatically, depending on the type of simulations being performed, but other plots and graphs can be added by right-clicking on the *Results* node and choosing from the list of plot types [99].

Besides the two default nodes just described, two additional top-level node types can be added to the root node: *Component* node and *Study* node. The *Component* node contains the model's geometry with its associated physics interface, mesh, variables, and other definitions that are local to that component. On the other hand, the *Study* node defines how to solve a model. These nodes can be added multiple

times, but when creating a new model using the default generator, one of each of these nodes is added to the root.

As referred at the beginning of Section 2.3, the framework's development was done using the model of the aorta studied by [84]. The model (.mph file type) was directly imported to COMSOL Multiphysics®, with the model's geometry being directly added to the *Component > Geometry* node. The numerical simulation's first step was to remove the aorta's wall once it is not an FSI simulation. The wall was directly removed in *Graphics* window, by first, selecting the domains referring to the wall and then selecting the option *Select and Hide*. Moreover, the plane originated to create an artificial section in the aorta for the optimisation step was also removed. Figure 5 shows the original model (Figure 5 – A) and the resulting model (Figure 5 – B).

Additionally, a convergence study for the mesh was carried and a new mesh implemented, which can be verified in Section 3.2.1.
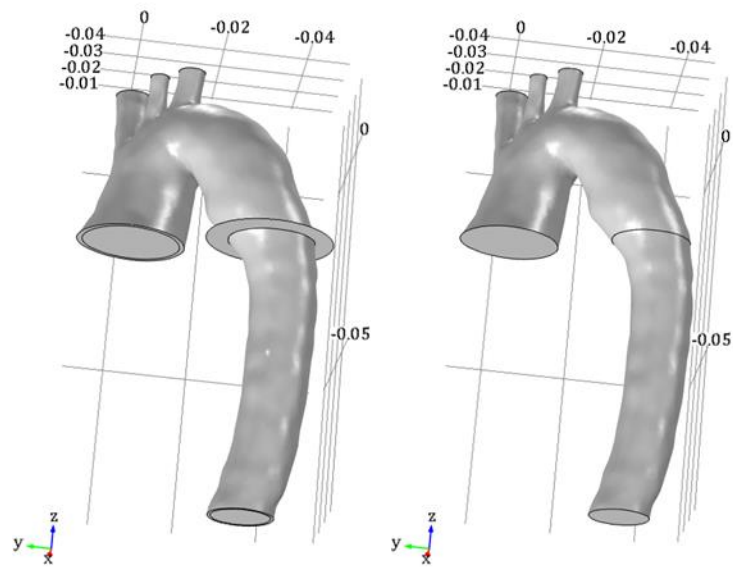
Figure 5: (A) Model used by [84] and (B) model after the needed adjustments to be used in the testing of the framework.

In the geometry displayed in Figure 5 the domain was defined, which is composed by the vessel inlet, the boundary in the ascending aorta (*Figure 6* - A); the primary outlet, a section in the descending aorta (Outlet DA; *Figure 6* - B); the vessel wall (*Figure 6* - C), and three supra-aortic outlets - surfaces of the sectioned brachiocephalic artery (Outlet BA; *Figure 7* - A), left common carotid artery (Outlet LSA; *Figure 7* - B) and left subclavian artery (Outlet LSA; *Figure 7* - C). An additional section, as described in Section 3.1, was included to be used in the optimisation study (Section S_{obs}; Figure 8).

(A) Inlet   (B) Outlet DA   (C) Aortic Wall
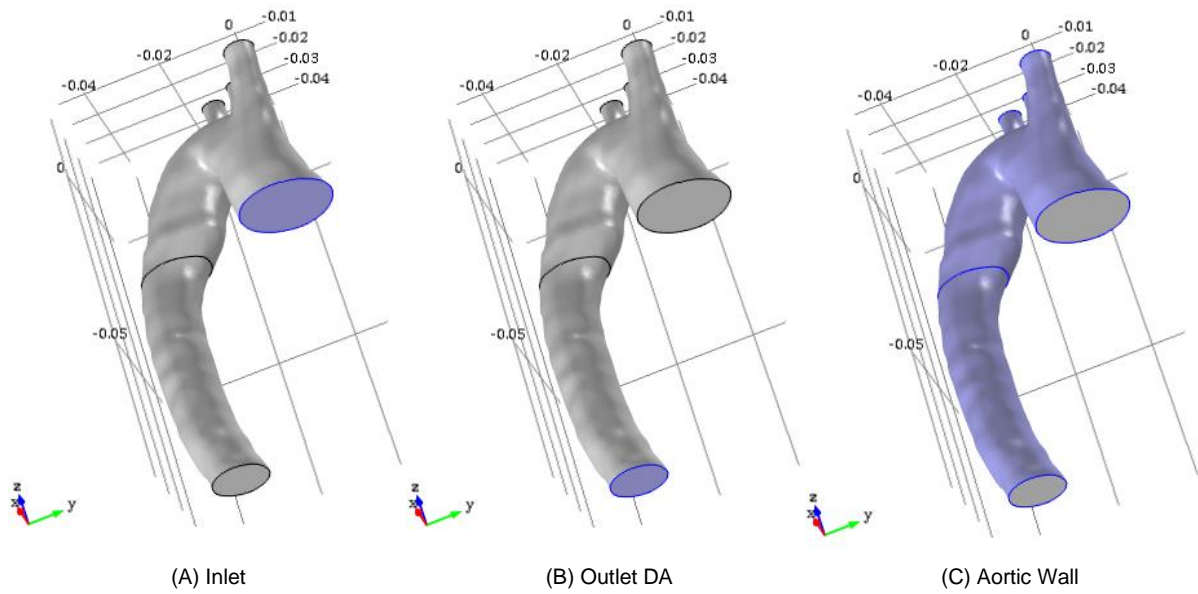
Figure 6: (A) inlet; (B) primary outlet – the surface of the descendent aorta (outlet DA); (C) wall of the aorta.

(A) Outlet BA   (B) Outlet LCA   (C) Outlet LSA
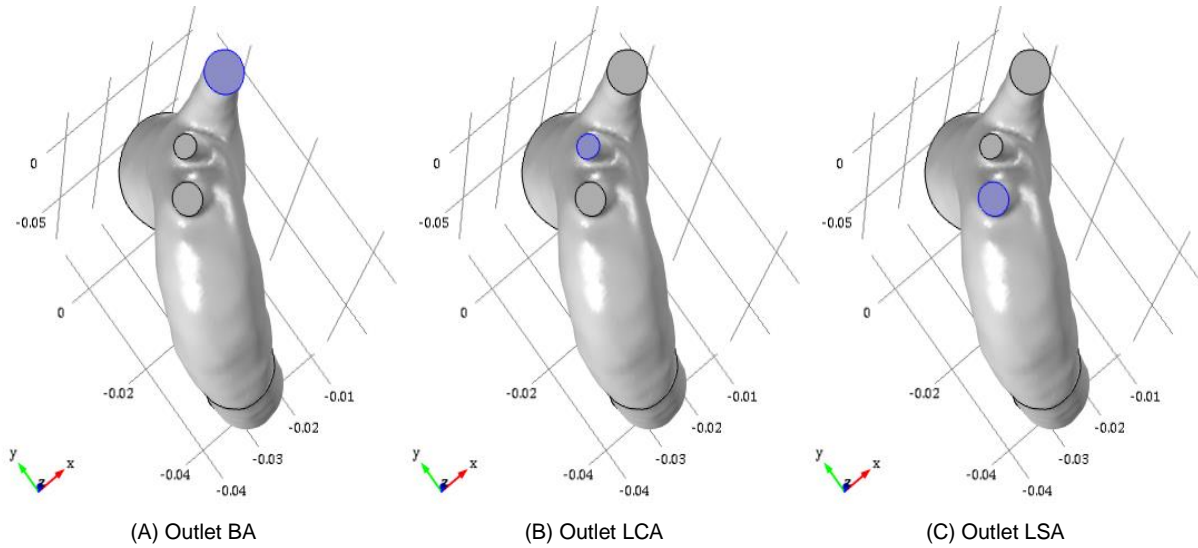
Figure 7: supra-aortic outlets: (A) surface of the brachiocephalic artery (outlet BA), (B) surface of the left common carotid artery (outlet LCA) and (C) surface of the left subclavian artery (outlet LSA).
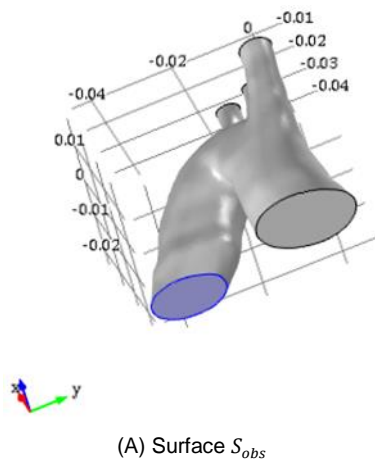
(A) Surface S_{obs}

Figure 8: Artificial surface to be used in the optimisation solver (Surface S_{obs}).

31

In the *Global > Parameters* node, some parameters, defined as static objects, are defined. These parameters include material properties, geometry properties and physical properties used in the *Physics* node. The full list of parameters added can be found in Annexe D (Table 24).

Once the domain and the parameters were defined, the *Physics* node was added to the *Component* node, by selecting in the ribbon *Add Physics* and expand the *Fluid Flow* section to add the *Laminar Flow* from the menu. To start, the physics of the forward problem was defined, and the *Laminar Flow* node was denominated as *Forward Laminar Flow (spf).* This new node will form its branch based on the model definition requirements, creating a template that automatically supplies the appropriate underlying PDEs. In this branch, the governing equations of blood flow and boundary constraints will be connected to the domain – composed by the inlet, the four outlets (DA, BA, LCA and LSA) and the wall. In each of them, a distinguish BC was applied.

The *Laminar Flow* branch will have three built-in nodes: *Fluid properties*, *Wall* and *Initial Values*. Within the *Laminar Flow* node settings, several characteristics need to be selected. First, in the *Domain Selection* section, the entire domain was selected– the aorta's lumen. Then, in the *Equation* section, the chosen option was Stationary, and the following NS equations were stated:

$$\begin{cases} \rho(u \cdot \nabla)u = \nabla \cdot [-pI + \mu(\nabla u + (\nabla u)^T] + F \\ \rho \nabla \cdot (u) = 0 \end{cases} \tag{56}$$

Finally, in the *Physical Model* section, the *Incompressible Flow* was considered, since blood was assumed as an incompressible fluid, and *Turbulence* model was set to none.

Next, the *Laminar Flow* branches were set up. Firstly, in the *Fluid Properties* node settings, the fluid domain was selected, the same as the Laminar Flow node domain. Then, the fluid properties were set as *User-defined,* and the *Density* and the *Dynamic viscosity* input fields were assigned with the quantities previously defined in *Global Definitions > Parameters*: rho_fluid and mu, respectively.

In the *Wall* node, the domain was selected as the boundary to be treated as the wall (*Figure 6* – C), and the *Boundary Condition* set up as No-slip where, as seen before, the velocity of the elements of the wall is set to zero.

Thirdly, in the *Initial Values* node, the initial default values are zero, which means the initial value for the velocity field is u = [0,0,0] m/s and for the pressure p = 0 Pa. These initial values were used as an initial guess.

After defining all the default nodes which were automatically added to the physics, a node per each boundary was added to the tree, by right-clicking in the *Laminar Flow* node and selecting either inlet or outlet. One inlet and four outlets (DA, BA, LCA and LSA) nodes were created, and for each, the settings were attributed independently.

Starting with the *Inlet* node in the *Boundary Selection* section, boundary represented in *Figure 6* – A was selected as the domain. Then, in the *Boundary Condition* section, *Laminar inflow* was set, the flow rate was select as the boundary condition and expression (37) was introduced. The expression of the inlet boundary condition is given by:

$$L_{entr} \nabla_t \cdot [-pI + \mu(\nabla_t u + (\nabla_t u)^T] = -p_{entr} n \tag{57}$$

This expression takes an additional variable, the L_{entr}, which is included to impose a fully developed profile, as discussed in Section 2.2.3. COMSOL Multiphysics® considers a virtual domain that is an

extrusion of the inlet with L_{entr} as length and with the same characteristics as the model itself. The length of this virtual extension is determined experimentally, in order to have a fully-developed flow by the time it reaches the real inlet, Γin. The software also adds an ODE to calculate the pressure applied at the entrance of this virtual extension, L_{entr}, such that desired inlet flow rate is obtained. The value of L_{entr} attributed ($L_{entr} = 6$) was chosen assuming equation (16).

In the node previously created of the descendent aorta (Outlet DA), the boundary represented in *Figure 6 – B* was selected from the *Boundary Selection*. In the *Boundary Condition* section, Pressure was set as the BC and attributed the value $p_0 = 0$ Pa. The pressure p_{exit} was applied at the exit of the virtual extension and computed by an ODE added by the software to ensure the imposed outlet flow rate is obtained. The expression imposed was:

$$[-pI + \mu(\nabla_t u + (\nabla_t u)^T)]n = -p_0 n \tag{58}$$

With $\widehat{p_0} \le p_0$, reflecting the suppress backflow option. This option means that the software is free to adjust the outlet pressure p locally to prevent fluid from exiting the domain through the boundary. Effectively, it means that the prescribed pressure P is P₀ if $u \cdot n \ge 0$, but it becomes smaller at locations where $u \cdot n < 0$. Sometimes it becomes smaller, and the backflow is substantially reduced, but not enough to prevent fluid from entering the domain through the boundary. Analogously to the laminar inflow condition, COMSOL Multiphysics® also considers an extrusion of the outlet with length L_{exit} as a virtual domain attached to it.

For the supra-aortic outlets, the boundary conditions were different for each dataset, and their expressions are stated in Table 1. In the case of MLBC (seen in Data A and Data B), after selecting the respective boundary representing the outlet (Figure 7), in *Boundary Condition* section, *Laminar Outflow* was selected, and *Flow Rate* applied with expressions defined in Table 1. Analogously to the laminar inflow condition, the COMSOL Multiphysics® also considers an extrusion of the outlet with length Lexit as a virtual domain attached to it. The pressure p_{exit} is applied at the exit of the virtual extension and computed by an ODE added by the software to ensure the imposed outlet flow rate is obtained. Lexit was defined again with the value six. The expression imposed was:

$$L_{exit}\nabla_t \cdot [-pI + \mu(\nabla_t u + (\nabla_t u)^T)] = -p_{exit} n \tag{59}$$

In the case of a TBC, the same methodology was applied as seen for the descendent aorta.

Once the *Forward Laminar Flow (spf)* node was defined, a second *Laminar Flow* physics was added to the tree to define the controlled problem – designated as *Controlled Laminar Flow (spf2)*. Again, one inlet and four outlets (DA, BA, LCA and LSA) nodes were created. The *Laminar Flow* settings, the *Fluid properties*, the *Wall*, the *Initial Values*, the Inlet BC and the Outlet DA BCs, were defined using the same settings as the *Forward Laminar Flow (spf)* physics.

For the supra-aortic outlets (BA, LCA and LSA), in *Boundary Condition* section, *Laminar Outflow* was selected, and *Flow Rate* applied with expressions defined in Table 2. The parameters p_x were left as unknowns, which were defined in the next step – the optimisation.

The *Optimization (opt)* interface contains tools for setting up advanced optimisation problems. The interface's primary purpose is its ability to set up objective functions, constraint contributions and control variables that are defined locally only on certain geometric entities and least-squares contribution with

a time or parameter dependence. The *Optimization* interface itself does not have any selection and is not associated with any particular space dimension [100].

The *Optimization* module can be used in combination with any other module in COMSOL Multiphysics. This module offers an interface for optimal computing solutions to the problem being solved. In this work, the optimisation module was used for the variational approach to obtain the ML parameter that best fits the in-silico flow. The variational approach used in this work means that the minimisation of the objective function was reached by varying the control variables within a set of constraints.

The *Optimization* node was added to the tree, which can be found in the *Add Physics > Mathematics > Optimization and Sensibility.* There are two sub-nodes in the *Optimization* node that need to be added – the Global Objective and the Global Control Variables.

In the Global Objective, the objective expression was set up, which was left the same during all simulations, and is the tolerance of the optimisation problem.

$$10^6 \times PartVelFit \tag{60}$$

The PartVelFit is considered the Objective Function and was attributed as a variable, since it is not static, in the *Component > Definitions > Variables*. In short, it calculated the difference in the velocities in each direction between the solution of the *Forward Laminar Flow* and the solution of the *Controlled Laminar Flow*, in the observed section. To obtain the variable PartVelFit, the integration function needed to be defined over the observation segment (S_{obs}). This was done by adding in *Component > Definitions > Component Couplings > Integration*. In this node, the boundary where the integral was being applied was selected. The Objective Function was, therefore, given by:

$$PartVelFit = \int_{S_{obs}} (u - u_2)^2 + \int_{S_{obs}} (v - v_2)^2 + \int_{S_{obs}} (w - w_2)^2 \tag{61}$$

In real-life examples, data measurements using medical devices include a certain amount of error in the form of noise. The in-silico data (Data A, Data B and Data C) was perturbed with noise to mimic this scenario. A random function was added to the Objective Function to modify the in-silico data to represent the noise. The random function was derived from a normal distribution with zero mean and standard deviation given by $\sigma = 0.1 * \frac{V_{max}}{3}$, where V_{max} is the maximum velocity at the inlet (Table 24). This new Objective Function is given by:

$$PartVelFit = \int_{S_{obs}} ((u + rn(x)) - u_2)^2 + \int_{S_{obs}} ((v + rn(y)) - v_2)^2 + \int_{S_{obs}} ((w + rn(z)) - w_2)^2 \tag{62}$$

Where rn is the random function generated.

Contrarily to the Objective Function, the control variables varied according to the test which was being performed. In the *Global Control Variables* node, the *Initial Value*, the *Upper* and *Lower Bound* were defined per each parameter - p_1, p_2 and p_3, and the values attributed to each test can be seen in Table 3. These parameters were used in the *Controlled Laminar Flow (spf2)* to substitute ML exponential parameter.

The logic behind the *Optimization* module is that the variations in the parameter p_x, according to the bounds imposed, changed the BC in the *Optimization* node, which returned a different solution of the blood flow. Comparing the obtained solution with the one from the *Forward Laminar Flow (spf),* the

Objective Function changed, and when its minimum is achieved, the adjusted parameters were returned as a result.

Finally, for each test of the controlled problem, two studies were performed: 1) a study using the *Forward Laminar Flow* (spf) definitions to obtain the in-silico data (denominated *Study Forward*) and 2) a study using the *Controlled Laminar Flow (spf2)* definitions and the *Optimization* module (denominated *Study Controlled*).

The first step to perform a simulation was to add the *Study* node to the tree, by clicking in the *Add Study* selection in the ribbon, which opens the menu, where the *Present Studies > Stationary* option was chosen, and the physics interface being studied was selected – the *Forward Laminar Flow (spf)* – and, finally, *Add Study*. This step added a study to the current model component with one default sub-node *Step 1: Stationary*. In this sub-node, since the physics was already selected in the previous step, the mesh was the only characteristic that needs to be select. The mesh chosen in Section 3.2.1 was selected.

A second sub-node was then added to the *Study* by right-clicking in it and selecting *Show Default Solver* – this added a sub-node named *Solver Configurations*. Under *Solver Configurations>Solution*, the sub-node *Stationary Solver* was expanded and the *Fully Coupled* node selected. In this node, the *Linear Solver* was set as *Direct*, which will enable the *Direct* node, and the settings under the Method and Termination section were changed. The damping factor was changed from 0.01 to 0.001 and the maximum number of iterations from 25 to 50. The nonlinear method used was kept as the Automatic (Newton).

The *Linear Solver* chosen was the *Direct* since it has been proved to work well when the number of degrees of freedom is less than one million [101]. In the *Direct* node, the algorithm PARDISO was selected, and all characteristics were left as the default. The package PARDISO is "a high-performance, robust, memory–efficient and easy to use software for solving large sparse symmetric and nonsymmetric linear systems of equations on shared–memory and distributed-memory architectures"[102]. PARDISO calculates the solution of a set of sparse linear equations with multiple right-hand sides, $AX = B$, using a parallel LU, LDL^T or LL^T factorization, where A and X, B are (n x n) and (n x nrhs) matrices, respectively. PARDISO supports a wide range of sparse matrix types and computes the solution of real or complex, symmetric, structurally symmetric or nonsymmetric, positive definite, indefinite or Hermitian sparse linear systems of equations on shared-memory multiprocessing architectures. [44], [97]

The simulation's last step was to create the *Study Controlled*, which will run on both *Controlled Laminar Flow (spf2)* and *Optimization* physics. The procedure is as follows: similar to the *Study Forward*, the *Study* node was added to the tree, but both *Controlled Laminar Flow (spf2)* and Optimization physics were selected as the physics interface studied. In the default existing sub-node *Step 1: Stationary*, besides selecting the mesh – the same as in *Study Forward* – the option *Values of variables not solved for* was ticked, *Solution* selected as the method and *Study Forward, Stationary* as the solution.

A second sub-node was then added to the *Study* by right-clicking in it and selecting, for this study, *Optimization*. In the *Optimization Solver* section, SNOPT was selected as the method within this node and all the remaining options kept as default.

Finally, the *Solver Configurations* was added as in the *Study Forward*. In this case, *Solver Configurations > Solution > Optimization Solver > Stationary* was expanded to apply the same configurations as in the *Study Forward*. Moreover, within the node *Optimization Solver*, the QP solver used was the Cholesky.

The solution for each test case was computed, with the presented definitions and the results presented in the next chapter. Additionally, some post-processing tools were used to visualise better and understand the results, namely the errors driven by the different parameters α_X obtained.

3.2.1. Mesh convergence

The FEM is a widely used approach to solve partial differential equations. COMSOL Multiphysics® applies the FEM to solve the NS equations, for fluid dynamics simulations.

The geometrical properties of the mesh applied directly contribute to the accuracy of the obtained solution. A more refined mesh, consisting of smaller finite elements, lead to more accurate results since the geometric domain is better approximated to the real domain (18). As the mesh size reduces, the number of nodes increases, and so does the number of degrees of freedom to be solved. Therefore, a more refined mesh implies a higher computational cost and a longer computational time, usually two limited resources in a regular computer machine.

The mesh selection is critical to validate the finite element model and thus have confidence in the solutions obtained but will be a trade-off between accuracy and computational expense. To select the most appropriate mesh a convergence analysis was used, and this will allow determining how many elements are required in a model to ensure that the results of an analysis are not affected by changing the size of the mesh.

The process consists of computing the same problem, using progressively finer meshes, and track a pre-determined parameter used for comparison between meshes. According to the convergence criteria, after a few iterations, at least three, the minimum size where the parameter starts to converge to the true solution can be determined. As the mesh refines, the difference between the solutions becomes smaller, and eventually, these changes will be small enough to consider the model has converged.

A convergence analysis was done in the aortic model used by [84] by reducing the element size and comparing the absolute and relative errors of the L2- and H1-norm of the velocity in the different solutions. To measure the error of the numerical solutions, it is necessary to introduce the functional spaces where the problem is defined. In this case, the system is defined in a Hilbert space ($H1(\Omega)$), and the chosen measures for the error are the $H1(\Omega)$ semi-norm and the $L2(\Omega)$ norm. The $L2(\Omega)$ norm and the $H1(\Omega)$ semi-norm are defined by, respectively:

$$\|\mathbf{f}\|_{L^2} = \sqrt{\int_{\Omega} \|\mathbf{f}\|^2} \tag{63}$$

$$\|\mathbf{f}\|_{H^1} = \sqrt{\int_{\Omega} \|\mathbf{f}\|^2 + \int_{\Omega} \|\nabla \mathbf{f}\|^2} \tag{64}$$

Where Ω is the integration domain of the previous formulas.

COMSOL Multiphysics® allows a manual or an automatic, which considers the problem's physics, mesh generator. To permit a higher rate of degrees of freedom (DOF) increase when refining the mesh, and taking into consideration the computational resources available, the automatic generator was chosen after several experiments with the training model. For both models, seven meshes were created, ranging from extremely coarse to extremely fine mesh size. A mesh is added by right-clicking in the *Mesh* node, under the model builder window, that will create a sub-node under the component tree. In the settings, the *Physics-controlled mesh* was chosen and attribute the size being studied. Additionally, a *Laminar Flow* physic with the same characteristics as the *Forward Laminar Flow* of Data B was added to the *Component* node. Finally, per each mesh a *Stationary Study*, using the same solver as the *Study Forward* for Data B, was implemented individually, and its solution saved in the same .mph file. A solution per each mesh can be found under the node *Results > Data sets*. Saving all the solutions in the same file allows the direct comparison of the distinct datasets, using the COMSOL Multiphysics® built-in operator *Join.* Six distinct joined datasets were created, each comparing a distinct solution (from Mesh 1 – 6) with the finer mesh solution (Mesh 7). For each *Join*, the *Combination method* chosen was *Explicit* so the data of each data set could be arbitrarily manipulated, by referring to its source dataset with the operators data1( ) and data2( ), in order to compute the errors of the velocity according to the L2- and H1-norms.

The variable f, in equations (63) and (64), is the difference between the velocity (u) computed with Mesh 1 to 6 and the velocity computed from Mesh 7. This difference is considered as the error of the velocity – because there is no exact solution, the best approximation was used, which is the one from the most refined mesh (Mesh 7). Using this definition, the absolute computational error can be computed, which is the difference between the exact solution of the mathematical model and the solution obtained through the numerical resolution of the model, and the relative error, which is the ratio between the absolute computational error and the exact solution. The absolute and relative error of velocity according to the L2-norm are defined in (65) and in (66), respectively. While the absolute and relative error of velocity according to the H1-norm are defined in (67) and (68), respectively.

$$e_{L2}^{abs} = \sqrt{\int_{\Omega}\|u_i - u_d\|^2} \tag{65}$$

$$e_{L2}^{rel} = \frac{\sqrt{\int_{\Omega}\|u_i - u_d\|^2}}{\sqrt{\int_{\Omega}\|u_d\|^2}} \tag{66}$$

$$e_{H1}^{abs} = \sqrt{\int_{\Omega}\|\nabla u_i - \nabla u_d\|^2 + \int_{\Omega}\|u_i - u_d\|^2} \tag{67}$$

$$e_{H1}^{rel} = \frac{\sqrt{\int_{\Omega}\|\nabla u_i - \nabla u_d\|^2 + \int_{\Omega}\|u_i - u_d\|^2}}{\sqrt{\int_{\Omega}\|\nabla u_d\|^2 + \int_{\Omega}\|u_d\|^2}} \tag{68}$$

In the presented expressions, u_i stands for the velocity vector computed from the solution of the Mesh i, for $i = 1,2,...,6$ and u_d is the velocity vector obtained from the solution of the most refined mesh, Mesh 7. The parcels containing the integral over the domain, Ω, were computed in COMSOL Multiphysics® through the operation *Results > Derived Values > Integration > Volume integration*, and

the volume of integration selected was the whole domain. In addition to these errors, per each mesh, using the operation *Results > Derived Values > Maximum > Volume Maximum*, the maximum element (h) size in the domain was extracted. Within the log file per each solution, the number of DOF was registered as well as the computational time. These computed values are summarized in Table 4.

Table 4: Resume of mesh: size, degrees of freedom, errors and computation time

Mesh	Size	DOF	Max Mesh Size (m)	e_{L2}^{abs} (m^4/s)	e_{H1}^{abs} (m^4/s)	e_{L2}^{rel}	e_{H1}^{rel}	Computation time (s)
1	Extremely Coarse	64,335	7.91E-03	2.62E-06	4.53E-03	1.50E-01	6.38E-01	64
2	Extra Coarse	74,471	7.03E-03	2.38E-06	4.39E-03	1.36E-01	6.19E-01	79
3	Coarser	108,855	4.82E-03	2.02E-06	4.26E-03	1.15E-01	6.01E-01	113
4	Coarse	193,611	4.32E-03	1.80E-06	4.22E-03	1.03E-01	5.96E-01	321
5	Normal	344,631	3.70E-03	1.72E-06	4.25E-03	9.83E-02	5.99E-01	854
6	Fine	675,303	2.81E-03	1.70E-06	4.34E-03	9.75E-02	6.12E-01	17,500
7	Finer	883,035	2.31E-03	-	-	-	-	26,483

To allow better visualization of the data, obtained errors were plotted against the DOF. From Table 4, as the degrees of freedom increase, the computational time also increases, but the L-2 absolute error does diminish from Mesh 4 and Mesh 5 onwards.

Figure 10 shows the absolute error of the L2-norm (calculated in (65)) in terms of the DOF. The absolute error is the greatest for Mesh 1, as expected since it is the coarsest mesh. The smallest error is found for Mesh 6, also as expected, since the finer the mesh, the closest the computed solution should be the exact value. The absolute error of the H1-norm is plotted in Figure 10. Again, the most significant error is found for Mesh 1. On the other hand, the solutions obtained from the smaller meshes (Mesh 5 and Mesh 6), according to the H1-norm, retrieve higher absolute errors. This might be driven by higher gradients of the velocity, comparing to the velocity, being found close to the outflow arteries, and dominating the expression.
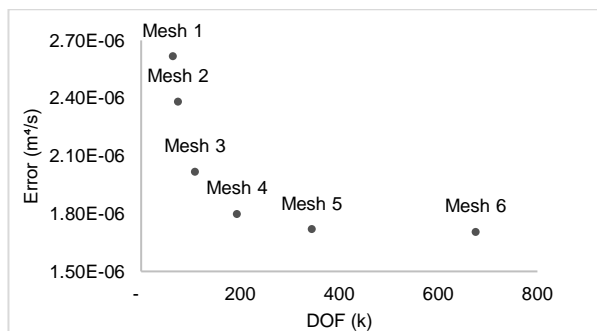
Figure 9: Absolute L_2 error for meshes 1 to 6
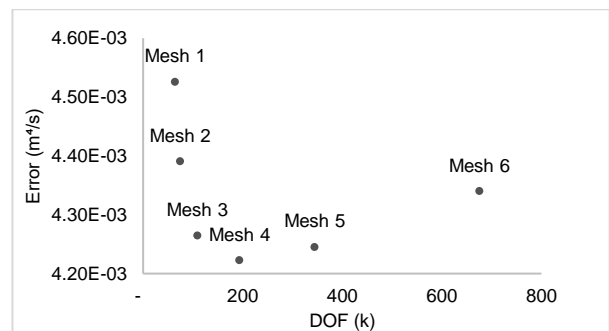
Figure 10: Absolute H_1 error for meshes 1 to 6

Absolute errors do not allow a proper comparison since they are not scaled to the problem. For a better conclusion, the relative errors to the L2-norma and H1-norm can be found in Figure 11 and Figure 12. Same results were obtained comparing with the respective absolute error.
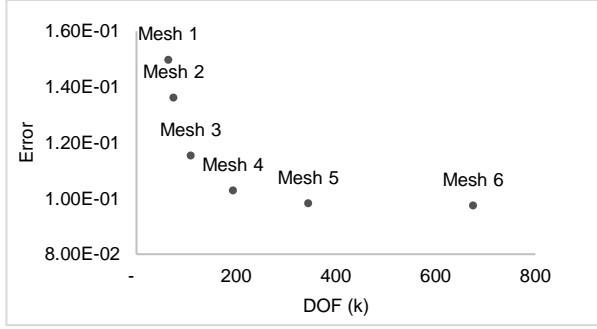
Figure 11: Relative L_2 error for meshes 1 to 6
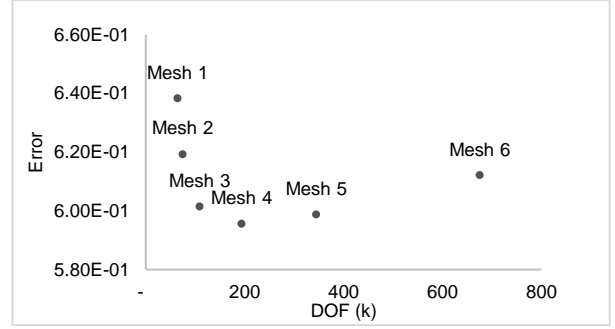
Figure 12: Relative H_1 error for meshes 1 to 6

The analysis led to the belief that the solution starts from Mesh 3 onwards and converges to a solution. Despite better errors for Mesh 4 and 5, the considerable increase of DOF from Mesh 4 to 5 will drive an exponential increment computational time, which does not translate in the error's improvement at the same proportion. Therefore, considering each simulation's duration and the errors obtained, presented in Table 4, the chosen mesh to proceed the computational analysis was Mesh 4.

3.2.2. Post-processing

The same way some parameters were added in the *Global* node, parameters and functions can be declared in the *Component* node to be used in its sub-nodes. The parameters and functions defined were used in the *Study* node and observed in the *Results* node.

To calculate post-processing metrics, some additional functions were defined in the *Component > Definitions* node. Several integration components coupling were included, under the *Component Couplings* section, which integrates an expression over the source defined under the Integration settings. The expressions were defined in the *Derived Values* node. An integral for each BC, for the Surface Obs, for the domain and for the entire surface of the model, were added.

To complete the post-processing, surfaces of each BC and Surface Obs for each solution (Forward and Controlled) were defined under the *Results > Data Sets* node. These surfaces are where the integrated expressions will be defined.

Wall shear stress

Wall shear stress (WSS) measures the forces applied tangentially to the blood's arterial wall. Blood flow leads to the development of superficial stresses near the vessel wall, that take the name of shear stresses, once they are parallel to the direction of the flow velocity vector very close to the wall.[60] The expression of the total stresses developed is given by:

$$\sigma = [pI + \mu(\nabla u + (\nabla u)^T)]n \tag{69}$$

This represents the stress tensor, which has a component normal to the surface and a component tangential to the surface. Since the needed stresses are the ones applied tangentially, this quantity is computed from (46):

$$WSS = \sigma - \sigma \cdot n \tag{70}$$

This measure was also added to the parameters in the *Component* node to be plotted in the *Results* node.

Errors

Three types of errors were used, in this work, to quantify the approximation of our adjustment to the in-silico data: absolute error, the difference between the in-silico values and the values of the tests; relative error, the absolute error divided by the in-silico data values.

These errors were calculated both over all the domain and over the boundaries, to understand where the method was better adjusted.

The absolute error and relative error in the domain were calculated using (65) and (66), respectively. Where u is the velocity of the Controlled Study in the domain Ω, and u_d is the velocity of the Forward Problem in the domain Ω.

In the boundaries, besides absolute error and relative error, the magnitude was also calculated using the following expressions:

$$e_{\Gamma_i}^{abs} = \sqrt{\int_{\Gamma_i} \|u - u_d\|^2} \tag{71}$$

$$e_{\Gamma_i}^{abs} = \frac{\sqrt{\int_{\Gamma_i} \|u - u_d\|^2}}{\sqrt{\int_{\Gamma_i} \|u_d\|^2}} \tag{72}$$

$$e_{\Gamma_i}^{mag} = \frac{\int_{\Gamma_i} \|u - u_d\|^2}{\int_{\Gamma_i} \|u_d\|^2} \tag{73}$$

Where u is the velocity of the Controlled Study in the boundary Γ_i, u_d is the velocity of the Forward Problem in the boundary Γ_i.

These errors were calculated by adding a *Global Evaluation* node to the *Derived Values* node, with the expressions defined above and selecting as the data the respective surface or domain where the integral was being calculated. The *Global Evaluation* setting allows the definition of the evaluation of the numerical value of a global variable.

3.3. Application to aortic coarctation

3.3.1. Data preparation

3.3.1.1. Data acquisition

For the aorta's coarctation, a thoracic X-ray computed tomography (CT) acquired from a 36-year-old patient, was given by the Hospital Santa Marta (Centro Hospitalar de Lisboa Central).

A CT scan is a medical imaging technique that uses computer-processed combinations of multiple X-ray measurements taken from distinct angles to produce cross-sectional images of the region of interest (ROI), designated as slices. The produced slices, whose thickness can range from 1 to 10mm, can be reformatted in multiple planes and consequently into a 3D image. In this work, images were obtained with a distance of 1.5 mm between each slice acquisition [104].

This type of medical image allows one to see the body's interior structures through the slides, in the three anatomical planes axial, sagittal and coronal. The images are displayed on a greyscale where each grey shade represents a degree of attenuation of the X-rays by the tissues.

A contrast dye can be applied to allow a better distinction between different structures. In our case, to enhance the aorta, Ultravist®, a solution of iopromide, was administered intravenously to the patient. Iopromide is a low osmolar, non-ionic X-ray contrast molecule that works as a contrast agent since the blood in contact with this agent absorbs more significant radiation than the surrounding tissues, highlighting the path of the flow [105], [106].

Using this set of images with adequate software and procedures, the aorta structure could be isolated and retrieved as a 3D model.

3.3.1.2. Data segmentation

This first step to obtaining the aorta model, to be used in COMSOL Multhiphysics®, was the segmentation of the CT images acquired and the geometry reconstruction.

Image segmentation, an essential medical imaging process, consists of portioning an image into multiple segments to allow the location of the region of interest (ROI) [107], [108]. In CT or MRI (Magnetic Resonance Imaging) images are subdivided into sets of pixels, which are the smallest controllable elements of an image. In this process, pixels are classified using grey level based or textural feature-based techniques, and then joined together based on this classification to delineate the ROI [109].

For this step, an open-source image processing software - 3D Slicer (version 4.10.2, https://www.slicer.org/) - was used. This software is specialized in medical image processing and three-dimensional visualization from DICOM data. DICOM (Digital Imaging and Communications in Medicine) is a format for medical files and a communication protocol to store medical information, ensuring the compatibility between equipment [110].

Once the software is launched, the DICOM data file was imported into the software. The file given by the hospital includes all studies and series performed in the CT acquisition. Therefore, it was necessary to choose the study series to load. After the series of interest was loaded, the data was displayed in Axial, Sagittal and Coronal view, as shown in Figure 13.

Each view in the 3D Slicer interface contains a set of slices, that cover the thoracic region, in each anatomic plane: axial (Figure 13 - A), sagittal (Figure 13 - B) and coronal (Figure 13 - C). The intersection of the structural information between these three planes allows the reconstruction of the volume of the aorta by selecting the pixels that represent the aorta in each slice, which will be merged to create a three-dimensional model.
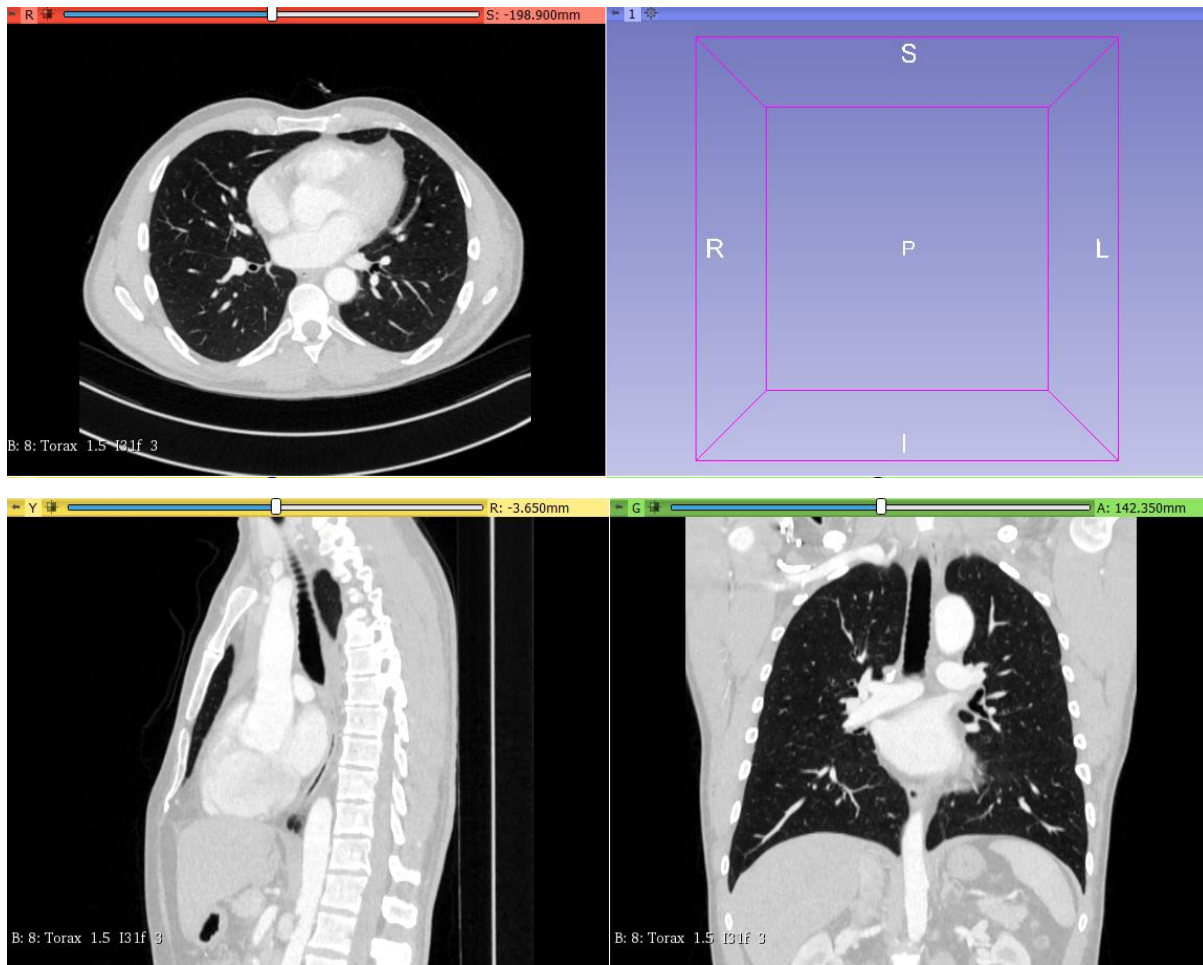
Figure 13: 3D Slicer panel after loading the DICOM data of a thoracic CT. The data was displayed as three sets of slices, in three different windows, according to the orientation of the image. On the top left, the axial plane; on the bottom left, the sagittal plane; and the coronal plane on the bottom right.

The next step was to identify the pixels representing the aorta in the slices to perform the segmentation. This operation allows for the elimination of unwanted image information and the selection and visualization of the ROI. With the contrast used in the CT, the aorta becomes an easily identifiable structure. However, to create a useful distinction between the aortic structure and its involving structures, contrast and brightness of the images need to be continuously adjusted, during the entire process, to identify the contour better.

The core plane used for the manual slice segmentation was the axial plane since it allows for better visualization of the complex aortic structure, especially in the aortic arch. Nevertheless, at some point, all planes were used to visualize the aorta, in case of doubt in distinguishing different structures, due to low contrast CT images, image artefacts, and noise.

To start the segmentation process, the *Segment Editor* module must be selected and +*Add* clicked to add a new empty segment and select the aorta category from a built-in list. The segment was a label map created by painting the pixels of the ROI on several slices which are then rendered into a volume. The tool *Level Tracing* was used to facilitate this painting task. The tool defines an outline where all the pixels have the same background value as the selected pixel by moving the mouse in the region of interest.

42

The contrast enhancement can be affected by numerous factors [111], including the concentration levels of the contrast dye and the duration of the procedure. As the CT contrast circulates in the body, it is diluted by the blood. The dilution effect was most significant in organs more distal from the site where the contrast was injected. Additionally, a CT image acquisition can take up to one hour, and during that time, the heart continues to beat, deforming itself and the surrounding tissues. Therefore, the contrast levels will not be uniform along the aorta, which will not allow for a perfect delineation of the structure using the *Level Tracing* tool alone. For these reasons, the *Level Tracing* tool was complemented with manual segmentation using the *Paint* and *Erase* tools – the more accurate the aorta is identified at this stage, the better to avoid edges or holes in the final model which will need to be removed. Figure 14 shows four slices in the axial plane after the pixels correspondent to the aorta are painted.

(A) Descending aorta

(B) Descending aorta and thoracic aorta

(C) Aortic arch

(D) supra-aortic arteries
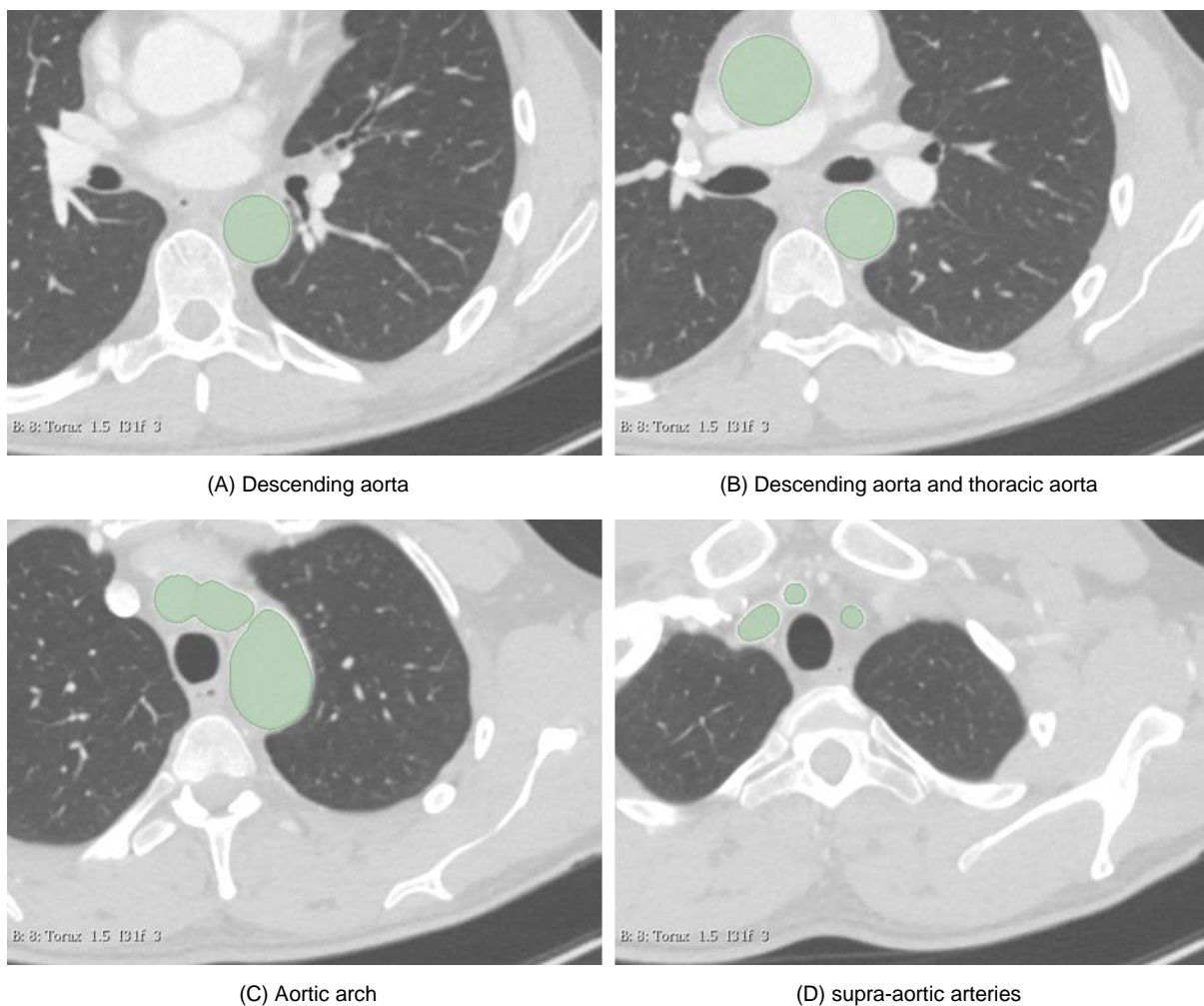
Figure 14: Segmentation of the aorta. Axial views of thoracic CT. (A) cross-sections of the descending aorta; (B) cross-sections of the descending aorta and the thoracic aorta; (C) cross-section of the aortic arch; (D) cross-sections of the supra-aortic arteries (brachiocephalic artery, left common carotid artery and left subclavian artery).

When all slices are processed, the full model can be previewed by selecting the option *Show 3D*, that generates a label map volume from the pixels selected in each slice. The 3D view permits a macroscopic view of the aorta, which helps check edgy places or wrongly selected pixels, which can be improved by manually painting and erasing, using the appropriate tools. The final segmented model

comprises the thoracic aorta from the ascending portion (above the aortic root) to the descending portion, including the beginning of the three aortic arch branches. The goal was to segment as much as possible of the aorta regions, and the supra-aortic branches, so more data is available in later stages of the modelling. However, while the descending aorta was easily defined, and therefore a big chunk was included, the three aortic branches due to its complexity were more difficulty defined, and the only a small proportion was included.

The *Smoothing* tool from the *Segment Editor* module was used to enhance the surface of the model, as a next step. The Gaussian method was used, a standard linear technique where all the frequencies are attenuated, except for the zero frequency, to introduce an absolute blur in the image. This attenuation (filtering) removes noise and consequently smooths the surface. In this method, each vertex's new position was computed as a weighted average, with the shape of a Gaussian function, of the current positions of the vertex itself and its direct neighbours (the ones that share an edge or face with the current vertex). [112]

Surface reconstruction from the previously segmented label map in 3D Slicer was carried on using the *Model Maker* module. A reconstruction with five smoothing iterations was chosen for a Laplacian filter type regarding the surface reconstruction parameters available, equivalent to a 5% smoothing. Such a small smoothing percentage was chosen to maintain the aortic models the most realistic possible. A default decimation (surface complexity reduction) value of 0.25 was chosen.
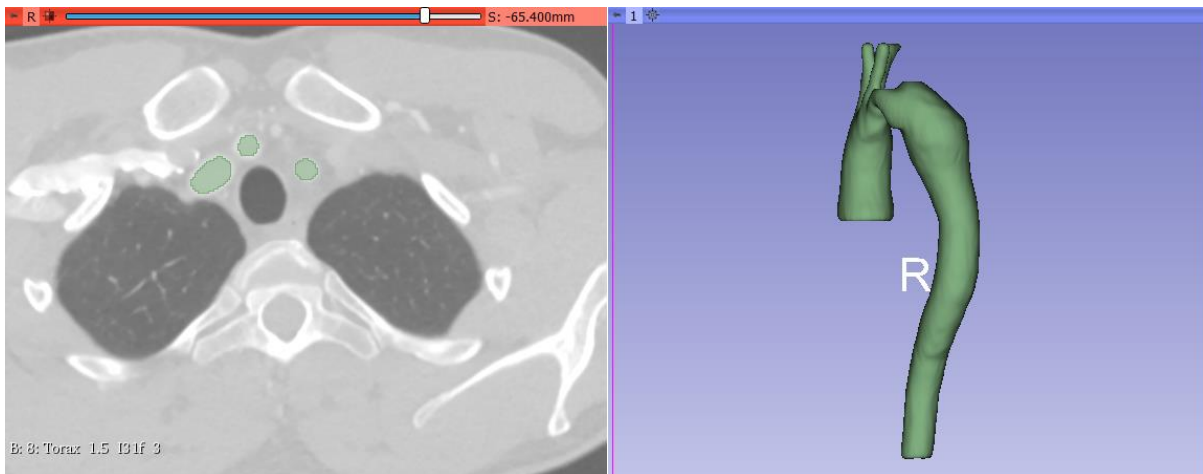
Figure 15: 3D visualization of the resulting segmentation in 3D Slicer after one application of Gaussian smoothing method with a standard deviation of 1.000 mm (continues in the previous page)

The information was saved as a label map, so it must be converted and exported as a Model. The file was saved in .STL extension format saves the surface like a raw unstructured triangular mesh to be imported to another software – MeshLab - where further adjustments regarding surface smoothing will be completed.

3.3.1.3. Data transformation

Following the aorta's segmentation, the next step was to improve the model's smoothness created in 3D Slicer. MeshLab (https://www.meshlab.net/) - an open-source system for processing and editing 3D triangular meshes – provides a set of tools for editing, cleaning, healing, inspecting, rendering, texturing, and converting meshes. In this step, MeshLab was solely used for its smoothing features,

In this step, firstly, the .STL file exported from 3D Slicer was imported as a mesh, and the option *Unify Duplicated Vertices* was enabled to eliminate duplicated data. Secondly, on the *Filters* tab, the option *Smoothing, Fairing and Deformation* module was selected, and the Taubin smoothing method chosen. The Taubin smoothing method, developed by Gabriel Taubin in 1995, consists of two consecutive Gaussian smoothing steps to avoid shrinkage [113]. This method allows significant smoothing of extensive and complex surfaces without the loss of natural characteristics. The first Gaussian smoothing step was applied with a positive scale factor (λ) to all vertices of the object. The second Gaussian smoothing step was applied with a negative scale factor (μ), whose magnitude was greater than the positive factor ($0 < \lambda < |\mu|$), to all vertices of the object as well. These two steps must be repeated, alternating between the positive and the negative scale factors to produce a significant smoothing effect. A trial and error approach was used to select the proper parameters λ and μ and the number of smoothing steps, and the final values chosen were 0.6, -0.6 and 100, respectively.
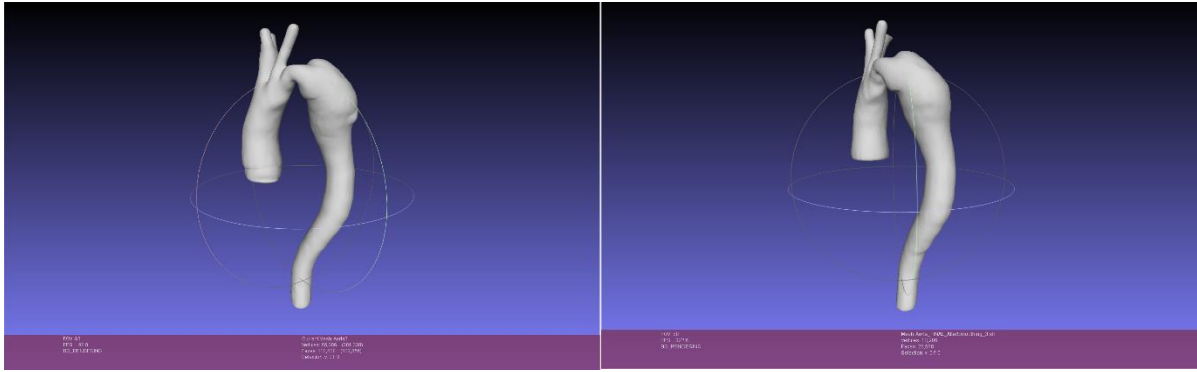
Figure 16: Model of the aorta in MeshLab, before (left) and after (right) application of Taubin smoothing method

After the smoothing step, the resultant .STL file has a substantially refined mesh, making the file too heavy to be imported to COMSOL Multhiphysics® and impossible to work within the software. To reduce the file size, and since the model will be given a mesh at a later stage in COMSOL Multhiphysics®, MeshLab was used again to re-mesh the model. For that, the Remeshing, Simplification and Reconstruction module was selected in the Filters tab, and the *Simplification: Quadratic Edge Collapse Decimation* method chosen. This method simplifies the mesh using a quadratic based edge collapse strategy, and the percentage of elements to be reduced was arbitrary. In this case, the original mesh contemplated 53,138 vertices and 106,672 faces. After a 50% element reduction, 26,570 vertices and 53,136 faces, were obtained. Since this file was still too heavy for the computer capacity, a second 50% reduction was made, where the final saved .STL file had 13,286 vertices and 26,568 faces.

Since the fluid dynamics are only being studied within the lumen of the aorta, there was no need to define the aortic wall, and therefore the final step will be to convert the .STL file to .IGES. The software Autoconverter (https://autoconverter.software.informer.com/), a native Windows operating system executable that allows importing, export and converts between different 3D files formats, was used for file conversion [114]. The geometry was finally ready to be imported into COMSOL Multiphysics

3.3.1.4. COMSOL Multhiphysics® transformation

The final step to obtaining a model of the aorta to analyze blood behaviour, through the simulation, was to create the geometry in COMSOL Multhiphysics® using the model previous developed using 3D Slicer and MeshLab.

The first step to creating the model's geometry, in COMSOL Multhiphysics®, was to import the .IGES file to the *Geometry* sub-node of the *Component* node. By right-clicking in the Geometry sub-node, the *Import* node was added to the tree. In the *Import* settings, the format chosen to import was the 3D CAD file, and the remaining options were kept as the default.

The subsequent step was to line up the geometry's extremities - the inlet and the four outlets - with the x-y plane by creating three work planes parallel to the x-y plane and extruding them as cylinders, as shown in Figure 8-B. This extrusion created new solids aligned with the x-y plane. Then, the wall's intersection with each of these solids was eliminated, guaranteeing the resulting geometry was parallel to the x-y plane. This operation was done with the tool *Compose from Booleans and Partitions* using

the expression imp1-(imp1*ext1+imp1*ext2+ imp1*ext3), being imp1 the label of the imported geometry, ext1, ext2 and ext3 the three extrusions.

The translation of the CAD geometry between software caused a change in its dimension, confirmed by measuring the inlet's cross-section area. Assuming the inlet was almost circular, the diameter can be computed from the area and compared with the diameter measured in the echocardiogram. The comparison revealed the current geometry was ten times greater than the real aorta, and for that reason, the geometry was re-scaled by 10.

The final step was preparing the geometry for meshing. The resulting geometry has more features than needed, i.e. thousands of faces and vertices, making the model bulky and interfering with its manipulation. The software has a set of attributes called *Virtual Operations* that enable simplifying the model to reduce the file size. The tool used was *Form Composite Faces* which ignores the boundaries of the selected faces, composing one major face that represented the entire surface of the geometry.
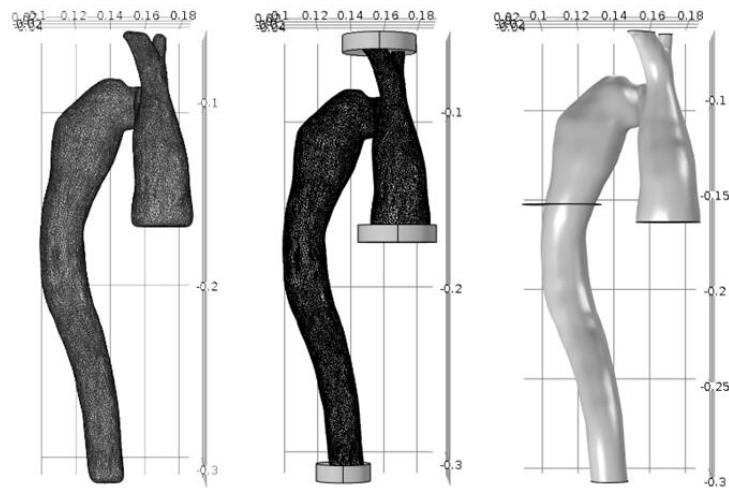
Figure 17: Graphic window of COMSOL Multiphysics. First column: imported geometry created in 3D Slicer; second column: geometry with the three work planes parallel to the x-y plane to be extruded as cylinders; third column: geometry after Form Composite Faces operation. Scale in meters.

An extra step was taken to give a virtual boundary in the middle of the aorta for the optimisation step. Therefore the model has two domains, an upper and a lower. The final domain union has two domains, 24,690 boundaries, 37,484 edges, and 12,798 vertices.

The mesh chosen for this geometry was the *Physics-controlled mesh* with Coarse size.

3.3.2. Numerical model

The assumptions made regarding the flow were the same as those for developing the framework (see Section 3.1.1). The domain represents the upper part of a patient-specific aorta with a coarctation, which was truncated due to its complexity by three planar surfaces: one at the entrance of the ascending aorta, to define the inlet; one in the intersection of the arteries brachiocephalic artery, left common carotid artery and left subclavian artery with the aortic arch, to define the supra-aortic outlets; The

47

domain can be observed in Figure 18 and one in the middle of the thorax, to define the descendent aorta outlet.

The domain Ω and respective surface $\partial\Omega$ are segmented as:

1. Aortic Wall (Γ_{wall}) representing the physical wall of the artery
2. Aorta inlet (Γ_{in}) representing the main inflow section
3. Aorta outlets (Γ_{out}) representing the set of non-connected outlet sections which include the descending aorta (T_{DA}) outlet, the brachiocephalic artery (Γ_{BA}) outlet, the left common carotid artery (Γ_{LCA}) outlet, and the left subclavian artery (T_{LSA}) outlet.

$$\Gamma_{out} = \Gamma_{DA} \cup \Gamma_{BA} \cup \Gamma_{LCA} \cup \Gamma_{LSA}$$

$$\partial\Omega = \Gamma_{wall} \cup \Gamma_{in} \cup \Gamma_{out} = \Gamma_{wall} \cup \Gamma_{inlet} \cup \Gamma_{DA} \cup \Gamma_{BA} \cup \Gamma_{LCA} \cup \Gamma_{LSA}$$

Like in the framework development, a virtual boundary (S_{obs}) was added to the aorta for the optimisation process.
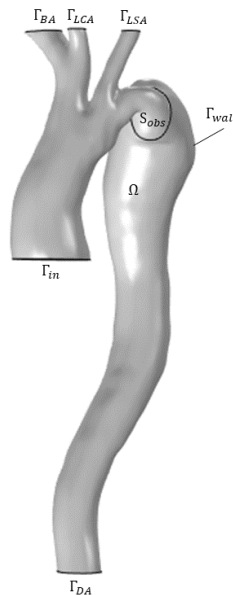
Figure 18: Domain of the numerical model of the aorta with coarctation with respective artificial boundaries – inlet, outlet and wall, and the section used in the optimisation simulation.

The controlled problem consisted of solving the system (50) using the following boundary conditions (Table 5), with the appropriate bounds (Table 6). The flow rate at the inlet was obtained from the literature ($Q_{in} = 316\ mL/s$) [115], based on the geometry of the aorta.

Table 5: Boundary conditions attributed to the supra-aortic outlets (BA, LCA and LSA) in the controlled problem for the aortic coarctation.

Test	Forward Problem	Inlet	Outlet DA	Outlet BA	Outlet LCA	Outlet LSA
P_1	Data P	■	●	α_1	α_1	α_1
P_3	Data P	■	●	α_1	α_2	α_3
P_v	Data P	■	●	β_1	β_1	β_1
Q_1	Data Q	■	●	α_1	α_1	α_1
Q_3	Data Q	■	●	α_1	α_2	α_3
Q_v	Data Q	■	●	β	β	β

- ■ Q_{in} α_x $Q_i = (V_{mean} * A_{in}) * \left(\frac{D_i}{D_{in}}\right)^{\alpha_x}, i \in (BA, LCA, LSA)$
- ● TFBC β $V_i = V_{mean} * \left(\frac{D_i}{D_{in}}\right)^{\beta}, i \in (BA, LCA, LSA)$

Table 6: Initial values, lower bound and upper bound for each optimisation test, in the controlled problem for the aortic coarctation.

Test	α_1/β_1			α_2			α_3		
	Initial Value	Lower Bound (low_1)	Upper Bound (up_1)	Initial Value	Lower Bound (low_2)	Upper Bound (up_2)	Initial Value	Lower Bound (low_3)	Upper Bound (up_3)
P_1	2	2	7	-	-	-	-	-	-
P_3	2	2	7	2	2	7	2	2	7
P_v	2	2	7	-	-	-	-	-	-
Q_1	2	2	7	-	-	-	-	-	-
Q_3	2	2	7	2	2	7	2	2	7
Q_v	2	2	7	-	-	-	-	-	-

Unlike the previous studies in Section 3.1.1, an additional simulation was performed for each dataset, where the laminar flow hypothesis was not considered (Test P_v and Test Q_v).

In this case, the objective function was built using patient-specific data. The controlled problem consisted of looking at the parameter α_x such that the following cost function:

$$f_{\cos t}(U) = \int_{S_{obs}} \left(\|u - v\|\right)^2 dx \tag{74}$$

Where u is the controlled problem solution in the section S_{obs} and v is the mean velocity obtained from a patient-specific hemodynamic gradient. A hemodynamic gradient, in the coarctation area, was obtained from the hospital ($P = 30\ mmHG$) and using a simplification of Bernoulli's equation:

$$\Delta P = 4V^2 \Leftrightarrow V = \sqrt{\frac{\Delta P}{4}} = 2.7 \text{ m/s} \tag{75}$$

In the case of the coarctation of the aorta, the forward problem was also solved for a better understanding of the controlled problem, since it allowed the calculation of the errors in the outlets by comparing the solutions of both problems. This problem consisted of solving system (44), using the BCs in Table 7. The inlet flow rate (Q_{in}) was the same as in the controlled problem.

Table 7: Boundary conditions attributed to the supra-aortic outlets (BA, LCA and LSA) in the forward problem for the aortic coarctation.

Test	Inlet	Outlet DA	Outlet BA	Outlet LCA	Outlet LSA
Data P	■	●	▲	▲	▲
Data Q	■	●	●	●	●

- ■ Q_{in} ● TFBC
- ▲ $Q_i = (V_{mean} * A_{in}) * \left(\frac{D_i}{D_{in}}\right)^{3}, i \in (in, BA, LCA, LSA)$

4. Results

This work aims to adjust Murray's law boundary conditions (MLBCs) by optimising its parameter, as seen in Section 2.2.2.3., using real data. The lack of data is an ongoing problem in numerical simulations in biological systems, to overcome this problem, three in-silico solutions to substitute the real data were generated. In-silico data was used to adjust Murray's law (ML) parameter and understand how it changes depending on the flow characteristics, varying from person to person.

In the first part of this section, the CFD simulation results of the in-silico data (Data A, Data B and Data C) will be discussed. Data A was generated attributing the classic MLBC with exponent $\alpha = 3$ in all supra-aortic outlets. Data B was generated in the same way as Data A, but in outlet LCA a traction-free boundary condition (TFBC) was given. Data C was generated with all supra-aortic outlets with TFBC.

In the second part, the adjusted solutions, obtained by adjusting Murray's parameter using an optimisation study over the in-silico data generated, will be compared. All tests were given MLBC in the supra-aortic outlets, with the parameter being either $\alpha = 3$ or a given control to be optimized (α_x). For each in-silico dataset, the flow was recovered using two different tests – one optimising a single parameter common to all outlets (Test A_1, Test B_1 and Test C_1), closer to what was defined by Murray; and another with a different parameter in each outlet (Test A_3, Test B_3 and Test C_3). Additionally, for Data B, the flow was recovered only in the outlet where traction free was attributed (Test B_1^{LCA}) with the remaining outlets with a classic MLBC ($\alpha = 3$). Finally, since using medical devices to obtain the flow metrics, an error is always associated, the parameters were adjusted by assuming a certain degree of error (10%) (Test A_1 + *noise*, Test B_1 + *noise* and Test C_1 + *noise*).

The numerical simulations solutions will include the distribution of flow velocity over the ROI, emphasising the supra-aortic outlets. Additionally, the quantification of how the hemodynamics metrics were affected by each adjustment, through the errors, will be shown and thus numerically emphasizing the regions most affected by the prescribed boundary conditions (BCs). The absolute, relative and magnitude of the relative error were studied in the several selected sections, namely, the supra-aortic outlets, the descendent aorta and section S_{obs}. The obtained control for ML will also be discussed.

As will be seen in the next chapters, results using one or three parameters were very similar. Therefore, for simplification of the results, hemodynamic parameters will be only presented for the solutions with one parameter being optimized (Test A_1, Test B_1, Test B_1^{LCA} and Test C_1).

4.1. Forward problem

4.1.1. Velocity magnitude

In Figure 19, the velocity's magnitude computed from the solutions of the in silico data, Data A (Figure 19 – A), Data B (Figure 19 – B) and Data C (Figure 19 - C), is presented at fifteen cross-sections along with the thoracic aorta, together with the velocity's direction at each slice. The three solutions are presented with the same colour range, for a better comparison. The velocity attributed in the inflow inlet corresponds to the peak of systole.

(A) Data A	(B) Data B	(C) Data C
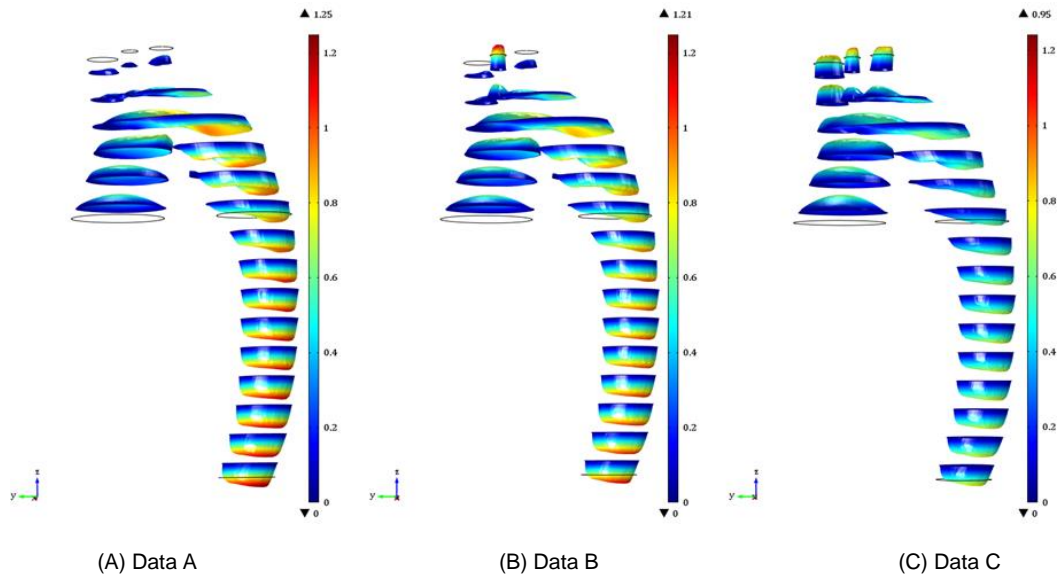
Figure 19: Distribution of velocity magnitude and direction on 15 slices of the domain, computed from the solution of the studies: (A) in-silico Data A, generated with MLBC with exponent $\alpha = 3$ in the supra-aortic outlets; (B) in-silico Data B, generated with MLBC with exponent $\alpha = 3$ in LCA, and TFBC in the outlets BA and LSA; (C) in-silico Data C, generated with TFBC in the supra-aortic outlets. Scale units: m/s.

Overall, the highest velocities are achieved for Data A (1.25 m/s), in the descendent aorta, and by Data B (1.21 m/s), in the LCA outlet. Data C shows lower velocity values, with a maximum of 0.95 m/s achieved in the supra-aortic arteries. The thoracic aorta shows lower values of velocity, in all three solutions, in comparison with the remaining sections of the aorta.

At the outset, for all images of Figure 19, the velocity is zero in the wall, as imposed by the no-slip condition. The distribution of velocity near the inlet shows a concentration of the higher values of velocity in the centre of the vessel, suggesting the development of a parabolic (fully developed) flow. The BC defined at the inlet drives this velocity distribution, since the value of L_{entr} is long enough to guarantee the development of the flow.

When reaching the aortic arch, for Data A and Data B higher velocities can be observed, slightly skewing along with the arch's interior, with the skewness being more pronounced in which the direction of velocity follows the curvature of the vessel. For Data C, as the data reaches the aortic arch, the profile becomes flattered, driven by the amount of flow leaving through all the outlets. When reaching the apex of aortic arch part of the flow exists towards the outlets, with the proportion of flow being higher for Data C, followed by Data B and later Data A.

For Data A, only a small percentage of the fluid goes through the outlets, but this type of representation makes it difficult to study the flow profile. When reaching the aortic arch, velocities increase at the apex of the curve and change direction following the vessel's bending. The diameter of the boundary drives the values of velocity since an MLBC is applied; since the ratio between the diameter of the boundary to the diameter of the inlet is powered to the estimated parameter (>1), the largest outlet takes a larger proportion of the flow.

For Data B, most of the flow exits towards the outlet where the TFBC was given (LCA), and in this vessel, the magnitude of the velocity reaches its peak.

Lastly, for Data C, a uniform distribution of flow per each outlet can be observed, at a higher proportion than seen in Data A. The increase of velocity starts in the middle of the arch, unlike the other simulations, where it happens right in the arteries' base. In this solution, a flat profile is observed, but again, the representation type does not allow a proper understanding.

In the three solutions, the velocity distribution exhibits the development of a characteristic crescent-shaped axial velocity profile when exiting the aortic arch, next to the 180-degree turn, towards the descending aorta. These swirling velocity components often arise in arteries and may be induced by rapid turning of the flow direction as arteries bend along their length. When a non-uniform flow is forced to turn, the balance of angular momentum will cause rotational or swirl velocity components to develop [24]. This behaviour is more prominent for Data A than for Data B and C.

All solutions show a flat velocity profile with the flow slightly skewed at the descending aorta, with higher values near the vessel's outer wall. In general, the descending aorta shows the highest velocities, with Data A and Data B showing considerable higher velocity values at the descendent aorta than Data C.

As expected, the distribution across the three supra-aortic outlets is not the same for the three different datasets since they were generated with different BCs in these outlets.

For Data A (94%) and Data B (90%), the most significant proportion of flow is forward towards the descendent aorta, according to Table 8, with section DA reaching the highest value of velocity in the thoracic aorta.

Table 8: Average flow rate of the solutions of the forward problem (Data A, Data B and Data C) in the supra-aortic outlets (Outlet BA, Outlet LCA and Outlet LSA), in the descendent aorta (Outlet DA) and the total outflow. Corresponding proportion (%) of flow rate in each outlet in relation to the outflow.

Data	Outlet BA		Outflow LCA		Outflow LSA		Outlet DA		Total Outflow
	(m/s^2)	(%)	(m/s^2)	(%)	(m/s^2)	(%)	(m/s^2)	(%)	(m/s^2)
Data A	5.7E-06	4.0%	1.0E-06	0.7%	2.4E-06	1.7%	1.3E-04	94%	1.4E-04
Data B	5.7E-06	4.2%	5.7E-06	4.2%	2.4E-06	1.8%	1.2E-04	90%	1.4E-04
Data C	3.2E-05	22.1%	1.0E-05	7.2%	2.0E-05	13.7%	8.2E-05	57%	1.4E-04

For Data A (Figure 20), since ML governs the distribution in all supra-aortic outlets, the largest artery (BA) corresponds to a higher flow rate (around 4% of total outflow), according to Table 8 followed by LSA (1.7%) and then LCA (0.7%). Nevertheless, according to literature, BA should receive the sum of LCA and LA. Since the BCs were imposed and the geometry might not fully replicate the anatomy, there is a discrepancy. Due to the big gap between velocities in the supra-aortic outlets and the descendent artery, this visualisation does not allow an understanding of the flow profile.

Regarding Data B (Figure 21), since a TFBC was imposed in outlet LCA, a flat profile can be observed in this outlet, while for the remaining supra-aortic outlets a fully developed profile is verified as a consequence of the imposed BCs. The flow rate in outlets BA and LSA, are the same as in Data A, observed by the values in Table 8 because the same BCs were attributed. Additionally, a more significant portion of the flow goes towards LCA in Data B (4.2%) than Data A (0.7%). Therefore, the remaining flow going towards DA is lower in Data B than Data A, which can be observed in Figure 21 and Table 8.

Finally, for Data C (Figure 22), the fluid flowing towards the outlets is proportional to the vessel's diameter by attributing the same BC in the supra-aortic outlets. The outlet BA (22.1%) has the most

significant proportion, followed by LSA (13.7%) and then LCA (7.2%). In this study, the outlet DA shows a flat profile with the lowest magnitude values from all studies, since only 57.0% of the flow is passing by. Since all outlets are subjected to the same conditions, even DA is subjected to the proportion of flow being dependent on the diameter, showing the highest distribution amount.

(A) Data A: superior view

(B) Data A: inferior view
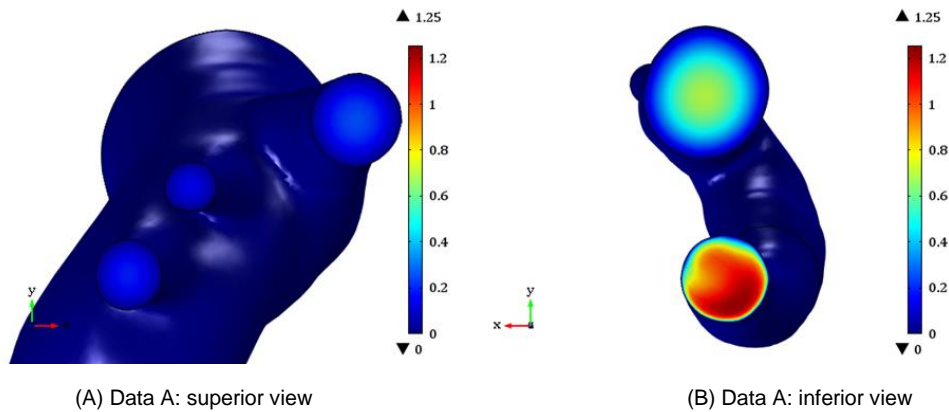
Figure 20: Distribution of the magnitude of velocity at (A) the surface of the supra-aortic outlets (B) and descendent aorta and inlet, computed from the solution of the study using in-silico Data A, generated with MLBC with exponent $\alpha = 3$ in the supra-aortic outlets. Scale units: m/s.

(A) Data B: superior view

(B) Data B: inferior view
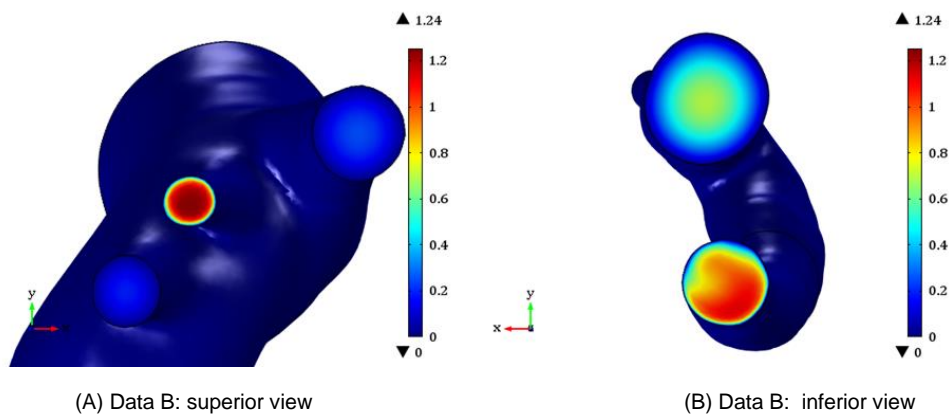
Figure 21: Distribution of the magnitude of velocity at (A) the surface of the supra-aortic outlets (B) and descendent aorta and inlet, computed from the solution of the study using in-silico Data B, generated with MLBC with exponent $\alpha = 3$ in LCA, and TFBC in the outlets BA and LSA. Scale units: m/s.

(A) Data C: superior view

(B) Data C: inferior view
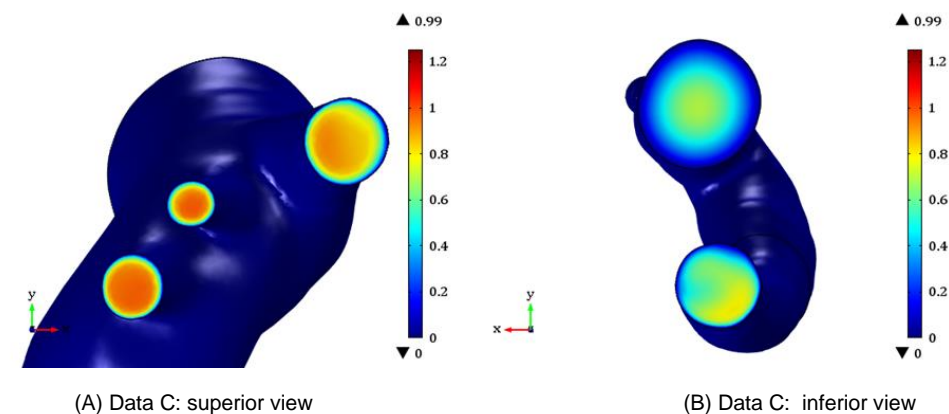
Figure 22: Distribution of the magnitude of velocity at (A) the surface of the supra-aortic outlets (B) and descendent aorta and inlet, computed from the solution of the study using in-silico Data C, generated with TFBC in the supra-aortic outlets. Scale units: m/s.

In section DA, a fully developed flow is observed for all solutions, skewing to the outer wall of the vessel in a crescent shape. This velocity distribution is justified because the fluid particles are forced to change direction and accelerate to preserve the axial flow. As the initial flow is fully developed, the highest velocities in the centre have high inertia, therefore are not easily deflected. In turn, the blood near the wall has less inertia, thus, significantly displaced. As a consequence, the highest velocities are found closer to the outer wall of the curvature.

To have a better understanding of the flow behaviour in the outlets being studied, the cross-section of each boundary – outlet BA (Figure 23), outlet LCA (Figure 24) and outlet LSA (Figure 25) - is presented. The first column in each figure corresponds to Data A, the second column to Data B and the third to Data C.

(A) Data A   (B) Data B   (C) Data C
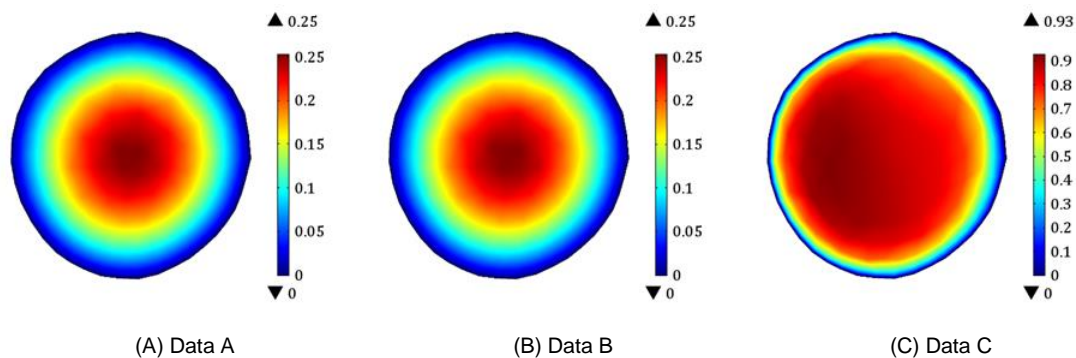
Figure 23: Distribution of velocity magnitude on the outlet BA cross-section, computed from (A) in-silico Data A, generated with MLBC with exponent $\alpha = 3$ in the supra-aortic outlets; (B) in-silico Data B, generated with MLBC with exponent $\alpha = 3$ in LCA, and TFBC in the outlets BA and LSA; (C) in-silico Data C, generated with TFBC in the supra-aortic outlets. Scale units: m/s.

(A) Data A   (B) Data B   (C) Data C
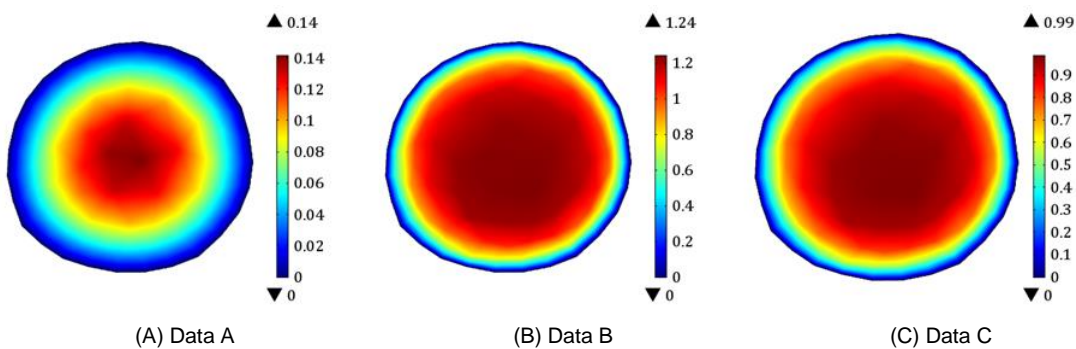
Figure 24: Distribution of velocity magnitude on the outlet LCA cross-section, computed from (A) in-silico Data A, generated with MLBC with exponent $\alpha = 3$ in the supra-aortic outlets; (B) in-silico Data B, generated with MLBC with exponent $\alpha = 3$ in LCA, and TFBC in the outlets BA and LSA; (C) in-silico Data C, generated with TFBC in the supra-aortic outlets. Scale units: m/s.

The first thing to notice is that the imposition of an MLBC forces a parabolic outflow in these outlets with the highest values of velocity being observed in the centre of the vessel (Outlets BA, LCA and LSA for Data A; outlets BA and LSA for Data B). For Data C, in BA, the flow is skewed towards the outside the vessel. As expected, velocities in outlets where the same MLBC was attributed the same values of velocity are obtained (0.25 m/s for outlet BA in Data A and Data B; 0.19 m/s for outlet LSA in Data A and B).

For outlets where TFBC was imposed, a flatter profile can be observed, with higher values closer to the wall (outlet LCA for Data B, outlets BA, LCA and LSA for Data C). In the outlet LSA, despite the same BC, the values of velocity in the centre of the vessel are higher for Data B than Data C.

Maximum values obtained for Data C are higher in all outlets, comparing to A, and higher in all outlets except LCA, for B. Furthermore, in Data C, all values of velocity are similar between them (around 0.9 m/s).

| (A) Data A | (B) Data B | (C) Data C |
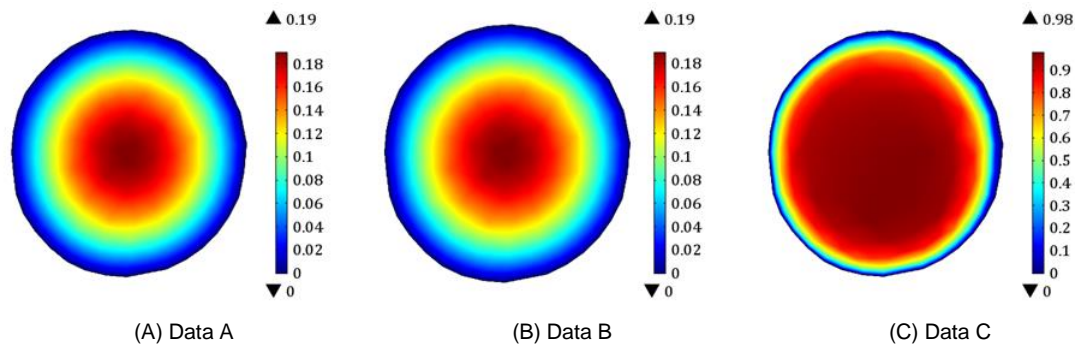
Figure 25: Distribution of velocity magnitude on the outlet LSA cross-section, computed from (A) in-silico Data A, generated with MLBC with exponent $\alpha = 3$ in the supra-aortic outlets; (B) in-silico Data B, generated with MLBC with exponent $\alpha = 3$ in LCA, and TFBC in the outlets BA and LSA; (C) in-silico Data C, generated with TFBC in the supra-aortic outlets. Scale units: m/s.

Another useful post-processing visualization element, in fluid dynamics, are the streamlines. A streamline is a line that is tangential to the instantaneous velocity direction. Therefore it shows the direction at which a fluid element will travel at any point in time [116]. In COMSOL Multiphysics®, the streamline positioning and the number of streamlines need to be defined to plot this type of graph. For this model, the inlet of the fluid domain was chosen as the starting point. A colour expression was also added, so the magnitude of the velocities together with the direction could be observed.

Studies reported that highest to lowest velocities are seen in the descending aorta, the thoracic aorta and ascending aorta, in this order. In Figure 26, the streamlines for Data A (Figure 26 – A), Data B (Figure 26 - B) and Data C (Figure 26 - C) are following the literature, and again the same range was used. Also, as noticed in previous visualisations, at the inlet, the velocity profile is fully developed. Some recirculation of the flow is observed, with insignificant velocities, in the aortic arch exit. Higher velocities can occur in the descendant aorta closer to the outer wall of the curvature. This phenomenon appears due to the initial fully-developed flow, characterised by high velocities in the centre, which imply high inertia, and lower velocities near the wall, subjected to less inertia. For this reason, when the blood is forced to change its direction and accelerate, due to the curvature of the geometry, the most significant displacements occur where there is less inertia, near the outer vessel wall. Data C is the only study where this phenomenon is less visible, with higher velocities being prominent in the supra-aortic arteries.
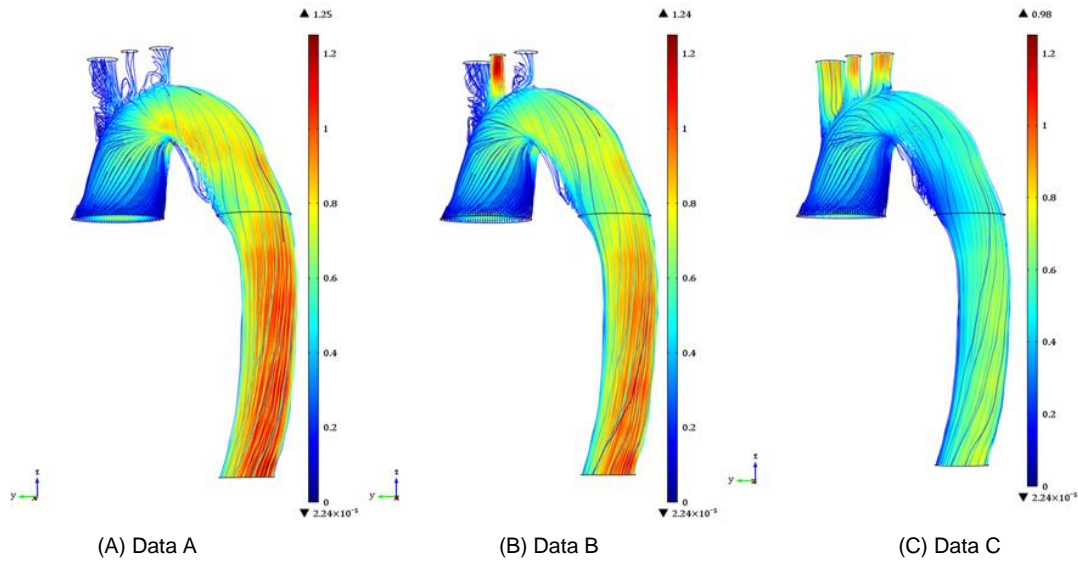
Figure 26: Streamline plots on the fluid domain, computed from the solution of the studies: (A) in-silico Data A, generated with Murray's Law boundary condition with exponent $\alpha = 3$ in the supra-aortic outlets; (B) in-silico Data B, generated with MLBC with exponent $\alpha = 3$ in LCA, and TFBC in the outlets BA and LSA; (C) in-silico Data C, generated with TFBC in the supra-aortic outlets. The streamlines have a colour expressing the velocity magnitude in m/s.

4.1.2. Wall shear stress

As seen in Section 3.2.2, complex WSS fields are observed due to the complex flow structures. The most crucial aspect that will be analysed will be the location of the highest shear stresses.

WSS peaks can be mainly found at the aortic arch since it is the branches' base and includes all the bifurcations. Because of these bifurcations, when blood arrives at the aortic arch, it is forced to divide into the branches. However, due to its high inertia, it cannot be immediately displaced into the axial directions of the branches. Consequently, the flow moves next to the bifurcation's inner walls, developing high shear stresses on the flow divider, as observed in the third column of Figure 29. These significant differences in the WSS within the branches connected to the aortic arch have been reported in previous studies [70].

Secondly, as a consequence of the asymmetry of the initial flow, which is skewed to the inside of the curvature of the vessel (at the aortic arch), the change in the direction of velocity implies that high shear stress develops on the outer wall of the curvature, and low shear stress on the inner wall.

Additionally, there are WSS peaks detected in the apex of the curve of the aortic arch. These may be an overestimation resultant for any error in the geometry, and it has been reported in previous studies [87]. Higher values of magnitude can be found for Data B, mainly concentrated in the artery LCA.
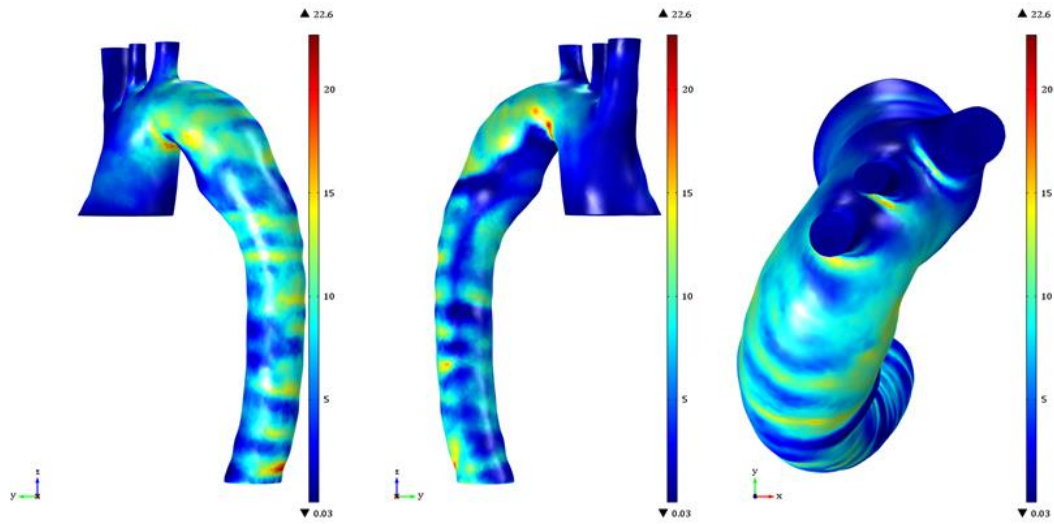
(A) Data A: anterior view   (B) Data A: posterior view   (C) Data A: superior view

Figure 27: WSS magnitude distribution computed from the solution of study using in-silico Data A. Scale units: Pa.
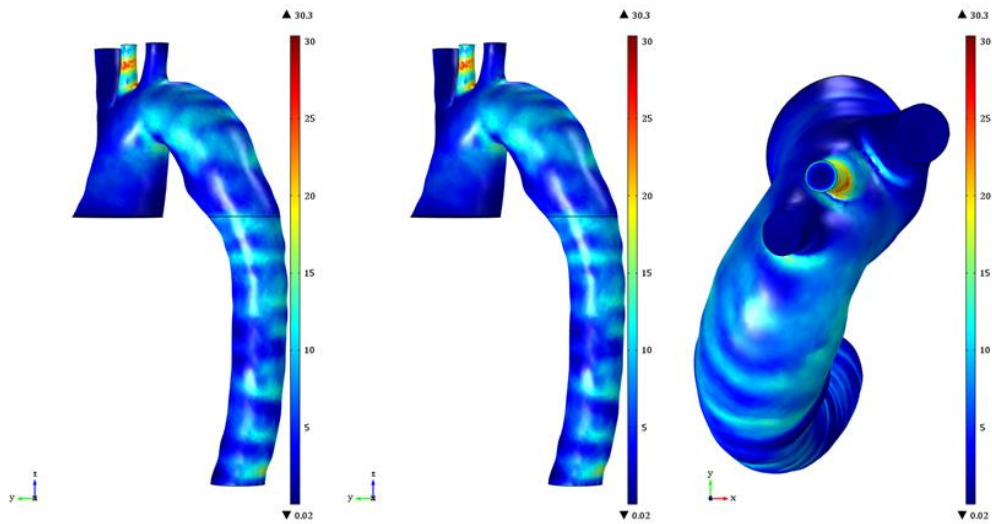
(A) Data B: anterior view   (B) Data B: posterior view   (C) Data C: superior view

Figure 28: WSS magnitude distribution computed from the solution of study using in-silico Data B. Scale units: Pa.
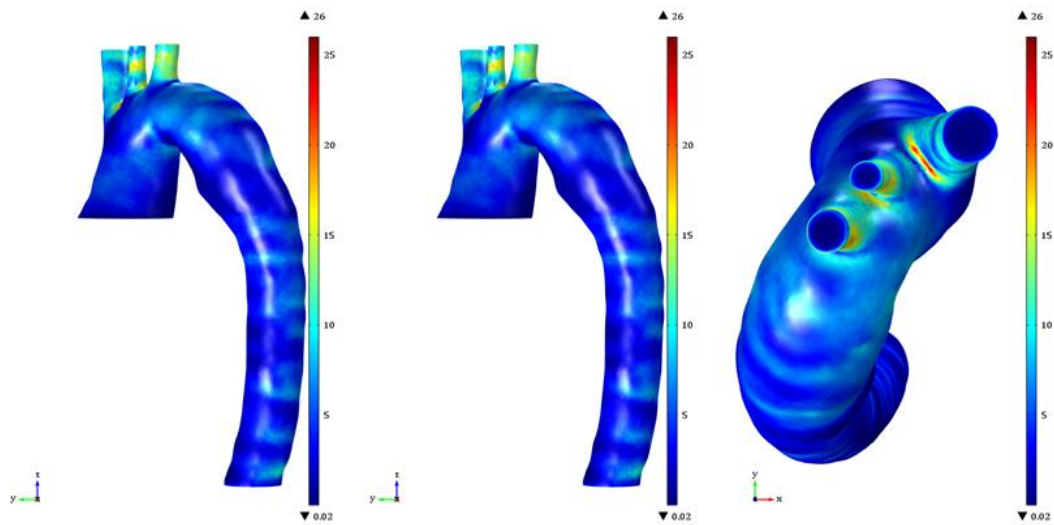
(A) Data C: anterior view   (B) Data C: posterior view   (C) Data C: superior view

Figure 29: WSS magnitude distribution computed from the solution of study using in-silico Data C. Scale units: Pa.

4.2. Simulations with controlled parameter

4.2.1. Recovering Data A

Data A was proxied as real data by attributing to the supra-aortic outlets (BA, LCA and LSA) MLBC, with the exponent defined by Cecil Murray [94] ($\alpha = 3$). The recovery of the flow in all three outlets was made by applying the optimisation study using either one control optimising a single parameter (α_1) common to all outlets, for Test A₁, or a using three controls optimising a different parameter in each outlet ($\alpha_1, \alpha_2, \alpha_3$), for Test A₃. These simulations function as a validation of the method since the same flow characteristics given in Data A were also attributed to the tests.

Table 9 contains the optimized ML exponent parameters for each test. Table 10 contains the errors of the domain, of the section used for the optimisation problem (S_{obs}) and the descendent aorta. Lastly, Table 11 contains the errors from the optimisation study of the supra-aortic outlets.

Table 9: Murray's Law parameters obtained by solving Test A₁, with and without noise, and Test A₃.

Test	α_1	α_2	α_3
A₁	3.0000	-	-
A₁ + noise	2.9831	-	-
A₃	2.9996	3.0005	3.0005

Table 10: Absolute errors, relative errors and magnitude in the domain, section S_{obs} and outlet DA of the controlled solutions obtained by solving Test A₁, with and without noise, and Test A₃.

Test	Domain		S_{obs} Section			Outlet DA		
	Abs. Error	Rel. Error	Abs. Error	Rel. Error	Mag.	Abs. Error	Rel. Error	Mag.
A₁	1.1E-07	3.0E-05	7.9E-07	7.8E-05	1.3E-11	2.0E-07	1.7E-05	-6.5E-07
A₁ + noise	6.9E-06	1.8E-03	1.6E-05	1.6E-03	1.5E-03	1.6E-05	1.4E-03	1.4E-03
A₃	1.5E-07	4.0E-05	7.9E-07	7.8E-05	-9.3E-11	1.6E-07	1.4E-05	-2.1E-06

Table 11: Absolute errors, relative errors and magnitude in the supra-aortic outlets (Outlet BA, Outlet LCA and Outlet LSA) of the controlled solutions obtained by solving Test A₁, with and without noise, and Test A₃.

Test	Outlet BA			Outlet LCA			Outlet LSA		
	Abs. Error	Rel. Error	Mag.	Abs. Error	Rel. Error	Mag.	Abs. Error	Rel. Error	Mag.
A₁	5.8E-09	6.0E-06	5.9E-06	2.8E-09	9.1E-06	9.1E-06	4.1E-09	7.5E-06	7.5E-06
A₁ + noise	1.8E-05	1.8E-02	-1.8E-02	8.6E-06	2.8E-02	-2.8E-02	1.3E-05	2.3E-02	-2.3E-02
A₃	3.9E-07	4.0E-04	-4.0E-04	2.6E-07	8.5E-04	8.5E-04	8.5E-04	7.0E-04	7.0E-04

The expected value for all controls, in this simulation, would be $\alpha_x = 3$ since it is the value given for the exponent of Murray's Law in Data A. Both tests served as a validation of the method. While for Test A₁, the exact value was obtained, for Test A₃, the values obtained for the three parameters were: $\alpha_1 = 2.9996$ for outlet BA, $\alpha_2 = 3.0005$ for outlet LCA, and $\alpha_3 = 3.0005$ for outlet LSA.

A more thorough approach of the errors used can be found in Section 3.2.2. For all tests, the error in the section S_{obs} is negligible since it was the section used in the objective function. Meaning, the optimisation would be achieved when the error in that section would be small enough.

For Test A$_1$, given that the obtained parameter α_1 is the same as the one used to obtain the in-silico Data A, the errors in all geometries are insignificant. Regarding Test A$_3$, absolute errors are also negligible, in the order of 10^{-7}, except for the absolute error in LSA (10^{-4}). Regarding relative errors, the outlet DA shows lower values than for the supra-aortic outlets (BA, LCA, LSA) - while the former has a relative error of 10^{-5} the error in the secondary outlets is in the order 10^{-4}.

Regarding the magnitude, for Test A$_3$, the imposition of a Murray's Law boundary condition in Data A and the optimisation study forces a parabolic flow in those sections (Figure 30). Therefore, the velocities in both studies have the same direction but with different magnitudes since $\alpha_x \neq 3$. This results in a similar relative and magnitude error, which can be observed in Table 11.
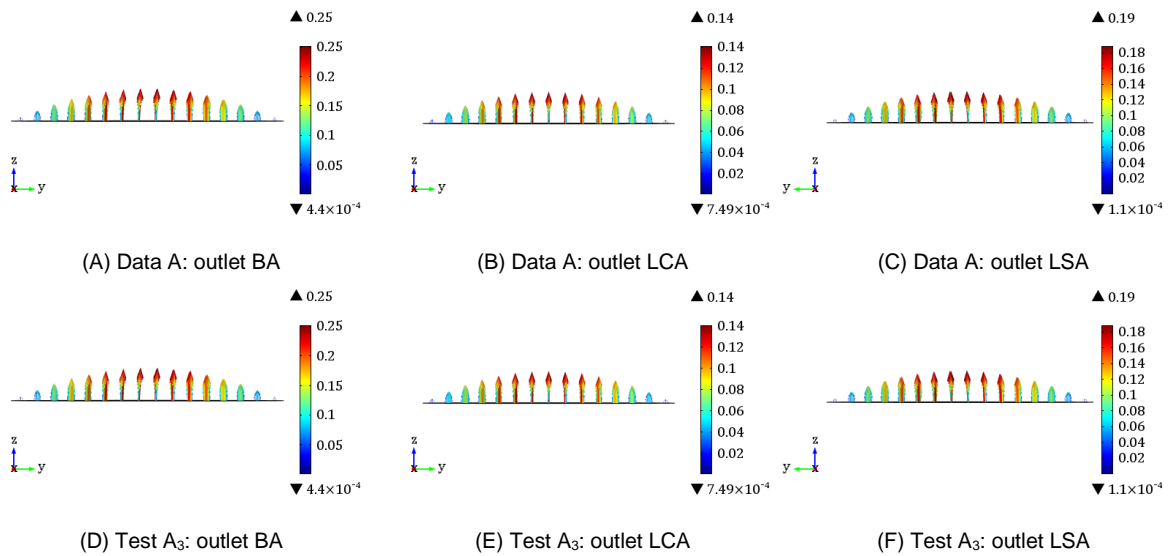
Figure 30: Velocity magnitude (colour range) and direction (arrows) in each supra-aortic outlet for Data A (top row) and Test A$_3$ (bottom row). Scale units: m/s.

When adding the variable noise to the study (A$_1$ + noise), the absolute error over the domain increases in the order of 10^1 and the relative error by 10^2. Regarding the supra-aortic outlets, the relative error is 10^4 times higher when compared with the test without noise (A$_1$). Nevertheless, the errors obtained for this test are negligible.

4.2.2. Recovering Data B

In this section, the recovery of the flow from Data B, which was produced by attributing TFBC ($P = 0$) to one chosen outlet and attributing to the remaining supra-aortic outlets, MLBC with $\alpha = 3$. For Data B, the outlet chosen was outlet LCA.

Three optimisation tests were performed to recover Data B. Firstly, MLBC was attributed with one control optimising a single parameter (α_1) to the outlet with TFBC in the in-silico data – Test B$_1^{\text{LCA}}$. Secondly, MLBC was attributed to the three supra-aortic outlets, with one control optimising a single parameter (α_1) common to all outlets - Test B$_1$ – or with three controls optimising a different parameter in each of the supra-aortic outlets ($\alpha_1, \alpha_2, \alpha_3$) - Test B$_3$. Additionally, both tests Test B$_1^{\text{LCA}}$ and Test B$_1$

were repeated considering noise (Test B_1^{LCA} + noise and Test B_1 + noise). The ranges of the controls used can be found in Section 3.1.1.2.

Table 12 contains the obtained optimized ML exponent parameters for each test. Values when applying a control in only one outlet (Test B_1^{LCA}) are around 60% lower than when applying controls in all three supra-aortic outlets (Test B_1 and Test B_3). Therefore, the velocities obtained in the outlet LCA will be higher for Test B_1^{LCA}. On the other hand, since the remaining boundary conditions for Test B_1^{LCA} have $\alpha = 3$ and $\alpha_1 < 3$, in Test B_1 and Test B_3, outlets LSA and BA will have higher values for both tests. For Test B_3, as the diameter decreases, $D_{BA} > D_{LSA} > D_{LCA}$, the value of the parameter increases, $\alpha_1 < \alpha_3 < \alpha_2$. Considering the equation (39), as the diameter of a daughter's vessel increases the flow entering that vessel also increases. Additionally, as the parameter of ML increases, the flow declines, since it is powered to a number < 1. Therefore, as the diameter increases, the parameter adapts to the largest daughter's flow is proportional high. For Tests B_1/B_3, where the flow in all outlets was subjected to optimisation, the parameters obtained for Test B_3 are analogous between them - $\alpha_1 = 2.3107$, $\alpha_2 = 2.3122$ and $\alpha_3 = 2.3118$ – and between the parameter obtained for Test B_1 ($\alpha_1 = 2.3114$). Since the parameters are very close to each other, the velocity, pressure, and WSS solutions will be the same. Therefore, the errors derived will also be similar. As seen previously, the noise added to the simulations does not impact the control obtained – while, for Test B_1^{LCA} the difference between the parameters obtained with and without noise is around -0.03%, for Test B_1 is 0.33%.

Table 12: Murray's Law parameters obtained by solving Test B_1^{LCA}, with and without noise, Test B_1, with and without noise, and Test B_3.

Test	α_1	α_2	α_3
B_1^{LCA}	1.4437	-	-
B_1^{LCA} + noise	1.4441	-	-
B_1	2.3114	-	-
B_1 + noise	2.3039	-	-
B_3	2.3107	2.3122	2.3118

Table 13 contains the errors of the domain, of the section used for the optimisation problem (S_{obs}), and of the descendent aorta. As seen before, the errors in S_{obs} can be neglected since it is used as the optimisation stop and therefore need to be as small as defined in the Objective Function.

The three tests have a low absolute error in the domain, with Test B_1^{LCA} presenting 0.002% and Tests B_1/B_3 0.034%. Tests B_1/B_3, nonetheless, present a considerable relative error (9.7%) while Test B_1^{LCA} a small one (0.678%). Since the same BC was attributed for outlets BA and LSA, in Test B_1^{LCA}, this relative error is only driven by the solution in outlet LCA while for Tests B_1/B_3 all outlets contribute to the error. The attribution of the same boundary conditions from Data B explains the neglectable error found for B_1^{LCA} in Table *14*, for those two outlets, in both absolute error (0.00% for BA and LSA) and relative error (0.06% for BA and 0.02% for LSA). On the other hand, for LCA – the outlet where the parameter was imposed – the absolute error is around 0.12% and the relative error 32.58%. This value of error means that the velocity in these outlets, with an optimised parameter, is 1/3 higher or lower than the velocity obtained in the controlled solution. Relative errors take into consideration the differences in the magnitude of the velocity vectors and their direction. Since the MLBC was imposed in the optimised

solution, this solution must have a parabolic shape while in the controlled solution, the flow does not necessarily achieve a parabolic flow.

Table 13: Absolute errors, relative errors and magnitude in the domain, section S_{obs} and outlet DA of the controlled solutions obtained by solving Test B_1^{LCA}, with and without noise, Test B₁, with and without noise, and Test B₃.

Test	Domain		S_{obs} Section			Outlet DA		
	Abs. Error	Rel. Error	Abs. Error	Rel. Error	Mag.	Abs. Error	Rel. Error	Mag.
B_1^{LCA}	2.4E-05	6.8E-03	6.8E-07	7.4E-05	-8.2E-12	3.3E-07	3.2E-05	3.8E-06
B_1^{LCA} + noise	2.4E-05	6.8E-03	9.6E-07	1.0E-04	-6.3E-05	6.7E-07	6.4E-05	-5.9E-05
B₁	3.4E-04	9.7E-02	6.6E-05	7.2E-03	-1.2E-10	2.7E-05	2.6E-03	1.5E-04
B₁ + noise	3.4E-04	9.7E-02	7.1E-05	7.7E-03	1.6E-03	3.3E-05	3.2E-03	1.8E-03
B₃	3.4E-04	9.7E-02	6.6E-05	7.2E-03	-9.0E-11	2.7E-05	2.6E-03	1.4E-04

Table 14: Absolute errors, relative errors and magnitude in the supra-aortic outlets (Outlet BA, Outlet LCA and Outlet LSA) of the controlled solutions obtained by solving Test B_1^{LCA}, with and without noise, Test B₁, with and without noise, and Test B₃.

Test	Outlet BA			Outlet LCA			Outlet LSA		
	Abs. Error	Rel. Error	Mag.	Abs. Error	Rel. Error	Mag.	Abs. Error	Rel. Error	Mag.
B_1^{LCA}	5.6E-09	5.8E-06	-9.5E-08	1.2E-03	3.3E-01	2.2E-02	1.1E-09	1.9E-06	-3.5E-08
B_1^{LCA} + noise	7.2E-09	7.4E-06	-3.3E-08	1.2E-03	3.3E-01	2.3E-02	2.5E-09	4.5E-06	-3.0E-08
B₁	1.1E-03	1.1E+00	-1.1E+00	2.8E-03	7.6E-01	7.7E-01	8.4E-04	1.5E+00	-1.5E+00
B₁ + noise	1.1E-03	1.1E+00	-1.1E+00	2.8E-03	7.6E-01	7.6E-01	8.6E-04	1.6E+00	-1.6E+00
B₃	1.1E-03	1.1E+00	-1.1E+00	2.9E-03	7.6E-01	7.7E-01	8.4E-04	1.5E+00	-1.5E+00

The high values in the relative error can be explained in Figure 31. This figure shows the magnitude of the velocity using an arrow; this will draw the shape of the profile in the graph, and a parabolic profile from a flat velocity profile can be easily distinguished. The controlled solution shows a flat profile with a parabolic profile with the optimisation solution, with higher and lower values of velocity in the centre and wall, respectively. To better understand the discrepancies between the two solutions, the magnitude of the velocity should be considered by itself. The magnitude for Test B_1^{LCA} is 2.23%, comparing to a relative error of 35.28%. To better understand the differences between the relative error and the magnitude, please refer to section 3.2.2.

(A) Data B: outlet LCA   (B) Test B_1^{LCA} : outlet LCA
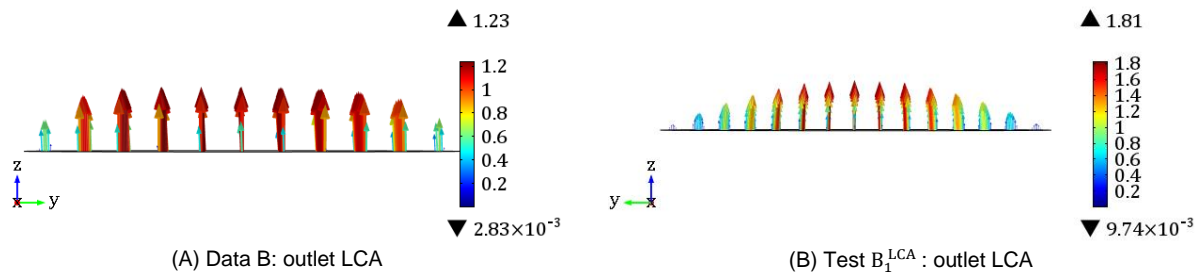
Figure 31: Velocity magnitude (colour range) and direction (arrows) in each supra-aortic outlet for (A) Data B and (B) Test B_1^{LCA}. Scale units: m/s.

For Tests B₁/B₃, while the absolute error is relatively small (ranging from 0.08% in LSA to 0.28% in LCA) in all supra-aortic outlets, relative errors and magnitude are significant, ranging from 76% in LCA, outlet with the TFBC, to 153% in LSA. LCA shows the highest absolute error but the lowest relative

error. Relative error and magnitude show the same value, in absolute values, driven by the same imposition of a fully-developed flow in outlets BA and LSA.

Relatively to the errors obtained using a noise component in the objective function, Table 14 shows that they are in the same order of the errors obtained for the same tests without noise. Therefore, in the remaining part of the section, the tests without noise will be the focus.

The solutions at several cross-sections along the aorta, representing both velocity's magnitude and direction, can be found in Figure 32, for Test B_1^{LCA} (Figure 32-B), Test B_1 (Figure 32-C) and for comparison with the in-silico data, solution for Data B is also represented in Figure 32-A. The solutions for Test B_3 will not be present since its values are very similar to Test B_1.

A non-slip condition can be observed in the wall and a parabolic flow profile near the inlet as seen for the forward problem. Moreover, for all solutions, the ascending aorta reporting lower values of velocity compared to the remaining portions of the aorta.

When reaching the aortic arch's base, velocities slightly skew along with the aortic arch's interior, with the skewness being more evident in which the direction of velocity follows the vessel's curvature. This skewness is most pronounced for Test B_1. Test B_1^{LCA}, similar to Data B, presents a flatter velocity profile justified by the significant amount of blood exiting towards the LCA outlet.

When reaching the apex of the aortic arch, part of the flow exits towards the outlet where the traction free boundary condition was given – LCA – for Test B_1^{LCA}. Table 16 shows that 9.2% of the outflow exists through the boundary LCA, compared to 4.0% for BA and 1.7% for LSA.

For Test B_1, the flow exiting towards the outlets is proportional to its diameter since the parameters are similar. The outlet BA retains 8.3% of the flow, and the outlet LSA retains 4.3% and the outlet LCA 2.2.%. Neither test gives a good estimate of the percentage of flow rate in LCA, on the one hand, Test B_1^{LCA} overestimates (9.2% vs 4.2%), on the other, Test B_1 underestimates (2.2% vs. 4.2%). In the remaining supra-aortic outlets, Test B_1 overestimates the flow rate comparing to Data B. According to the literature, BA should have the sum of the remaining (6.5%).

In Test B_1^{LCA}, a fully-developed high-velocity flow exists towards LCA, for Test B_1 the flow keeps low velocity towards the outlets with higher velocities being only found in the arch's interior. Since the parameter of ML applied in Test B_1 is the same for all outlets (and >1), it is expected that vessels with higher diameter show the highest velocities. The characteristic crescent-shaped axial velocity profile when exiting the aortic arch seen for Test B_1^{LCA} is lesser prominent for Test B_1.

The velocity distribution exhibits the development of a characteristic crescent-shaped axial velocity profile when exiting the aortic arch, next to the 180-degree turn, towards the descending aorta. These swirling velocity components often arise in arteries and may be induced by rapid turning of the flow direction as arteries bend along their length. When a non-uniform flow is forced to turn, the balance of angular momentum will cause rotational or swirl velocity components to develop. [24]

When the flow reaches the descending aorta, it becomes more uniform as it goes towards the abdominal aorta. Velocities are higher than in the thoracic aorta, and the flow shows a flatter profile, slight skewing to the curve of the aorta. Again, Test B_1 shows the highest velocity values.

As seen for Test B_1^{LCA}, in the descending aorta, the flow skews towards the curve of the aorta. The values of velocity along the aorta, except for the outlet LCA, are similar for the three studies. While

maximum velocity for Data B and Test B_1^{LCA} is reached in the outlet, for Tests B_1 is in the descent aorta. Values, nevertheless, a similar for all three solutions.

(A) Data B   (B) Test B_1^{LCA} (C) Test B_1^{LCA} + noise

(D) Test B_1 (E) Test B_1 + noise
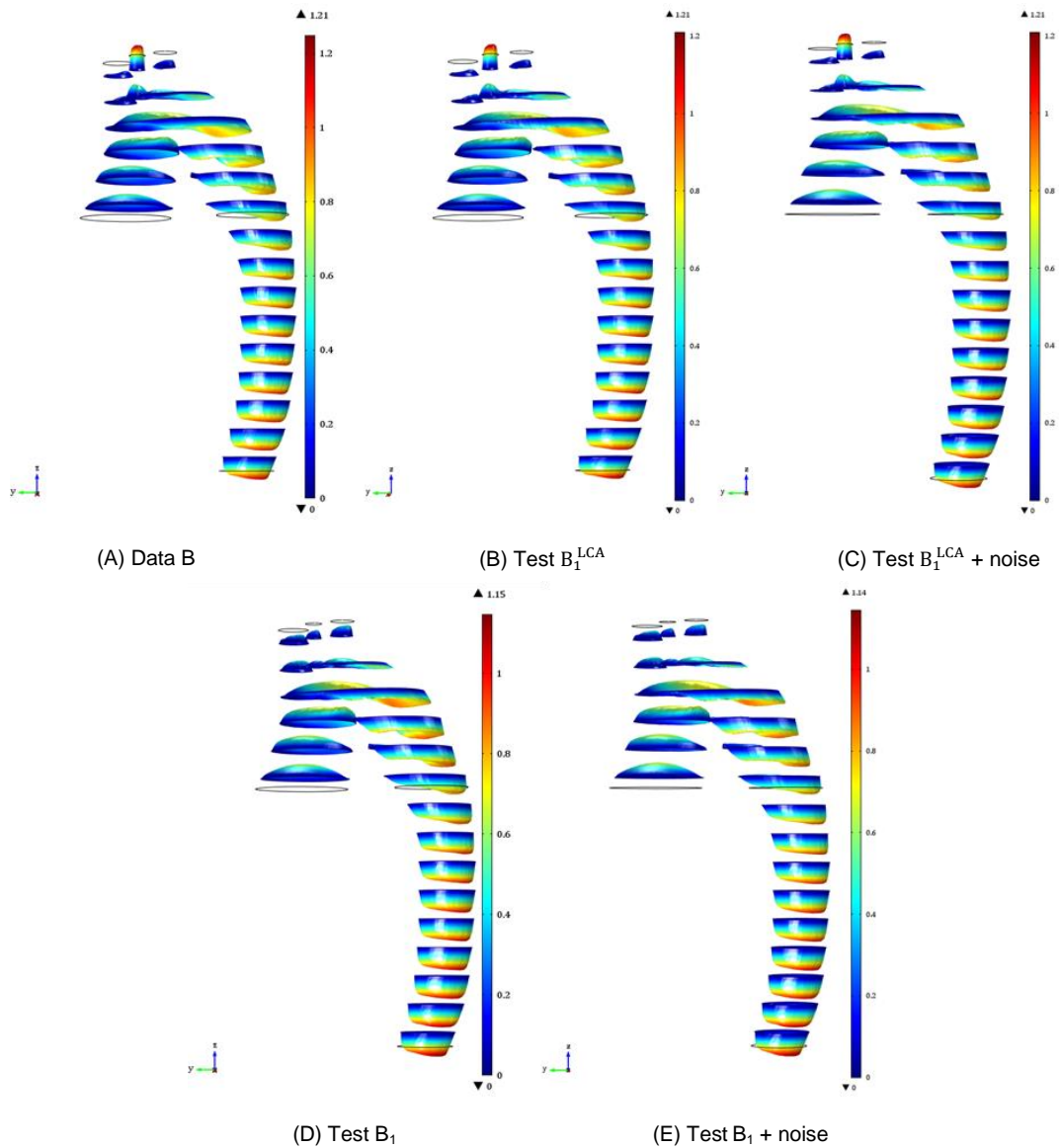
Figure 32: Distribution of velocity magnitude and direction on 15 slices of the domain, computed from the solution of the studies: (A) in-silico Data B, generated with MLBC with exponent $\alpha = 3$ in LCA, and TFBC in the outlets BA and LSA; (B) controlled Test B_1^{LCA}, (C) controlled Test B_1^{LCA} with noise, (D) controlled Test B_1 and (E) controlled Test B_1 with noise. Scale units: m/s.

Table 15: Average flow rate of the controlled solutions obtained by solving Test B_1^{LCA}, with and without noise, Test B_1, with and without noise, and Test B_3, in the supra-aortic outlets (Outlet BA, Outlet LCA and Outlet LSA), in the descendent aorta (Outlet DA) and the total outflow. Corresponding proportion (%) of flow rate in each outlet in relation to the outflow. The flow rate of Data B solution for comparison.

Test	Outlet BA		Outflow LCA		Outflow LSA		Outlet DA		Total Outflow
	(m/s^2)	(%)	(m/s^2)	(%)	(m/s^2)	(m/s^2)	(%)	(m/s^2)	(m/s^2)
B_1^{LCA}	5.7E-06	4.0%	1.31E-05	9.2%	2.41E-06	1.7%	1.22E-04	85.9%	1.4E-04
B_1^{LCA} + noise	5.7E-06	4.0%	1.30E-05	9.1%	2.41E-06	1.7%	1.22E-04	85.3%	1.4E-04
B_1	1.2E-05	8.3%	3.12E-06	2.2%	6.12E-06	4.3%	1.22E-04	85.3%	1.4E-04
B_1 + noise	1.2E-05	8.3%	3.16E-06	2.2%	6.18E-06	4.3%	1.22E-04	85.2%	1.4E-04
B_3	1.2E-05	8.3%	3.12E-06	2.2%	6.12E-06	4.3%	1.22E-04	85.3%	1.4E-04
Data B	5.7E-06	4.2%	5.7E-06	4.2%	2.41E-06	1.8%	1.22E-04	89.9%	1.4E-04

In Figure *33* to Figure *37*, the velocity distribution among the supra-aortic outlets (column 1) and for the inlet and outlet DA (column 2), for Data B (Figure *33*), Test B_1^{LCA} (Figure *34*), Test B_1^{LCA} with noise (Figure *35*), Test B_1 (Figure *36*) and Test B_1 with noise (Figure *37*) can be seen. Colour ranges were kept independent for a better understanding of the behaviour in each test.

For Data B, a flat profile can be observed in the outlet with traction free boundary condition (LCA), and a fully-developed profile is assumed for the remaining outlets as imposed by its boundary condition.

For Test B_1^{LCA}, by applying TFBC in LCA, a large proportion of the flow exist the aorta through this outlet, achieving a fully developed profile. For the remaining outlets, due to the range of the legend, is challenging to study their profiles. The maximum velocity achieved for LCA in Test B_1^{LCA} is significantly higher than the one obtained for Data B. Since the control obtained was smaller than 3, the velocity will reach higher values here.

For Tests B_1, since the MLBC is being imposed in all outlets, the proportion of flow is directly related to the diameter; therefore, the velocities reached are the same for all of them. Again, due to the range in the visualisation, a fully developed flow cannot be predicted. Nevertheless, by ML, the flow should be parabolic. Velocities in BA and LSA are higher in these studies than for Data B and Test B_1^{LCA}. In the aorta descendent, a similar profile, as seen in the in-silico data., was obtained.

(A) Data B: superior view   (B) Data B: inferior view
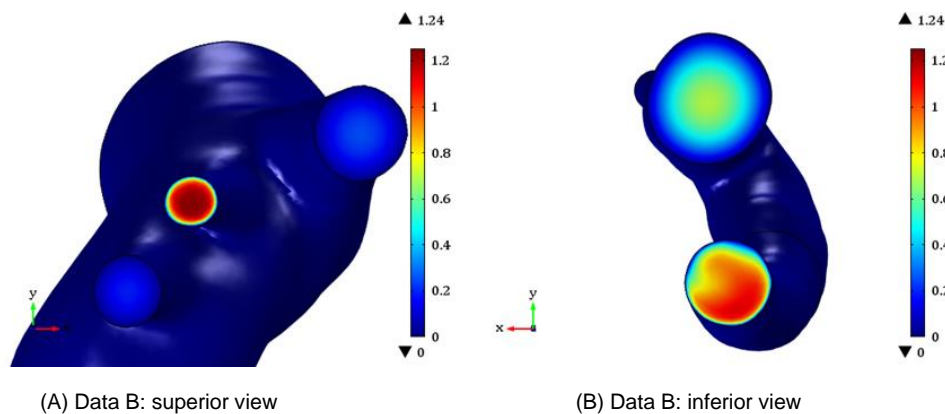
Figure 33: Distribution of the magnitude of velocity at (A) the surface of the supra-aortic outlets (B) and descendent aorta and inlet, computed from the solution of the study using in-silico Data B, generated with MLBC with exponent $\alpha = 3$ in LCA. Scale units: m/s.

(A) Test B_1^{LCA}: superior view

(B) Test B_1^{LCA}: inferior view
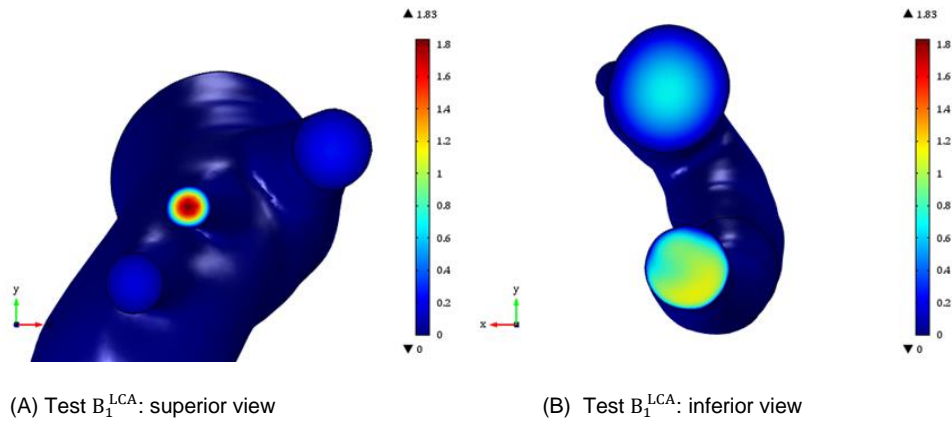
Figure 34: Distribution of the magnitude of velocity at (A) the surface of the supra-aortic outlets (B) and descendent aorta and inlet, computed from the solution of the controlled Test B_1^{LCA}. Scale units: m/s.

(A) Test B_1^{LCA}+ noise: superior view

(B) Test B_1^{LCA}+ noise: inferior view
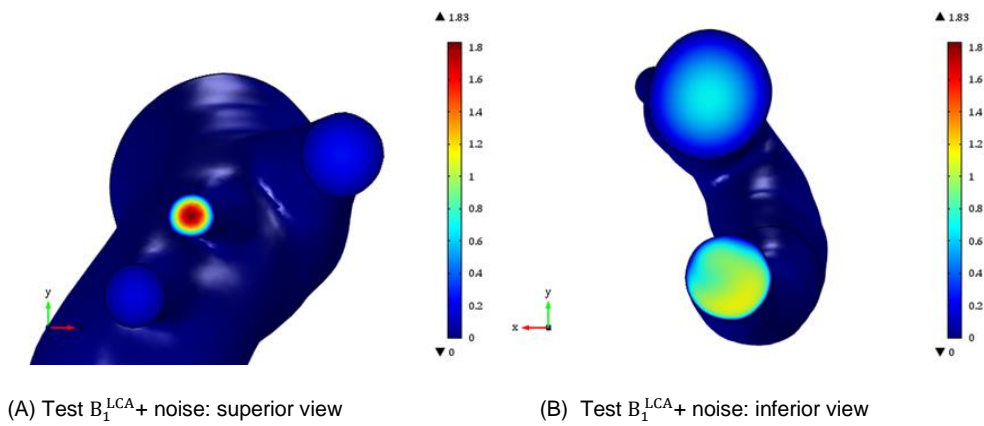
Figure 35: Distribution of the magnitude of velocity at (A) the surface of the supra-aortic outlets (B) and descendent aorta and inlet, computed from the solution of the controlled Test B_1^{LCA} with noise. Scale units: m/s.

(A) Test B_1: superior view

(B) Test B_1: inferior view
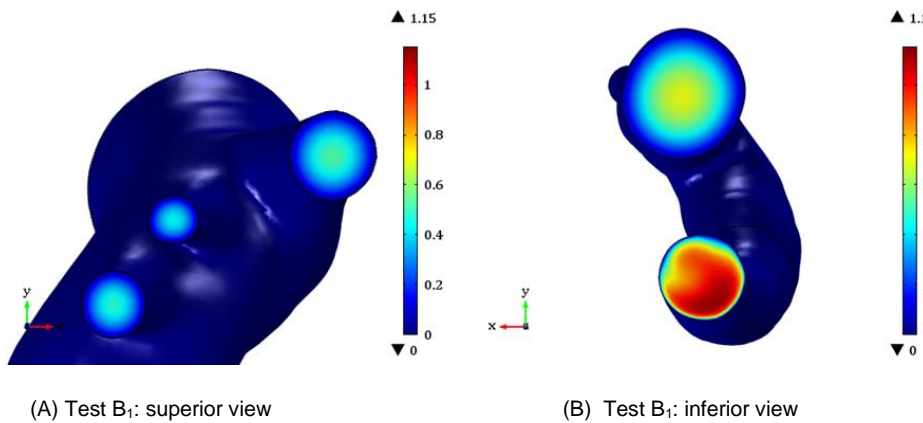
Figure 36: Distribution of the magnitude of velocity at (A) the surface of the supra-aortic outlets (B) and descendent aorta and inlet, computed from the solution of the controlled Test B_1. Scale units: m/s.

(A) Test B_1 + noise: superior view   (B) Test B_1 + noise: inferior view
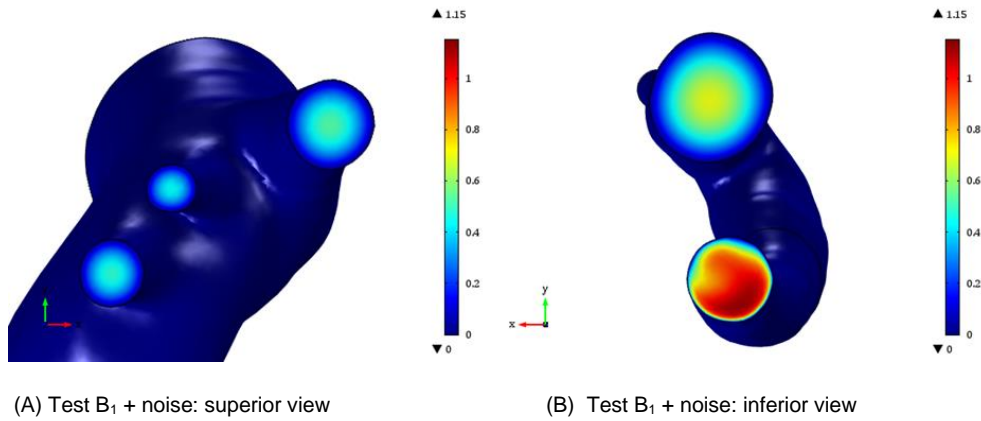
Figure 37: Distribution of the magnitude of velocity at (A) the surface of the supra-aortic outlets (B) and descendent aorta and inlet, computed from the solution of the controlled Test B_1 with noise. Scale units: m/s.

To better understand the flow behaviour in the supra-aortic outlets, the cross-section of BA, LCA, and LSA is compared for each study. These representations will allow for a better comparison between the real data solution and the optimisation solution.

(A) Data B   (B) Test B_1^{LCA} (C) Test B_1^{LCA} + noise   (D) Test B_1 (E) Test B_{1} + noise
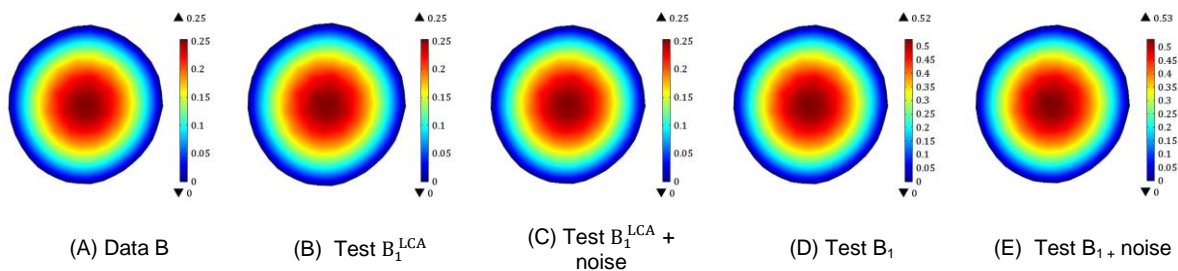
Figure 38: Distribution of velocity magnitude on the outlet BA cross-section, computed from (A) in-silico Data B, generated with MLBC with exponent $\alpha = 3$ in LCA, and TFBC in the outlets BA and LSA; (B) controlled Test B_1^{LCA}, (C) controlled Test B_1^{LCA} with noise, (D) controlled Test B_1 and (E) controlled Test B_1 with noise. Scale units: m/s.

(A) Test B_1^{LCA} (B) Test B_1^{LCA} + noise   (C) Test B_1 (D) Test B_{1} + noise
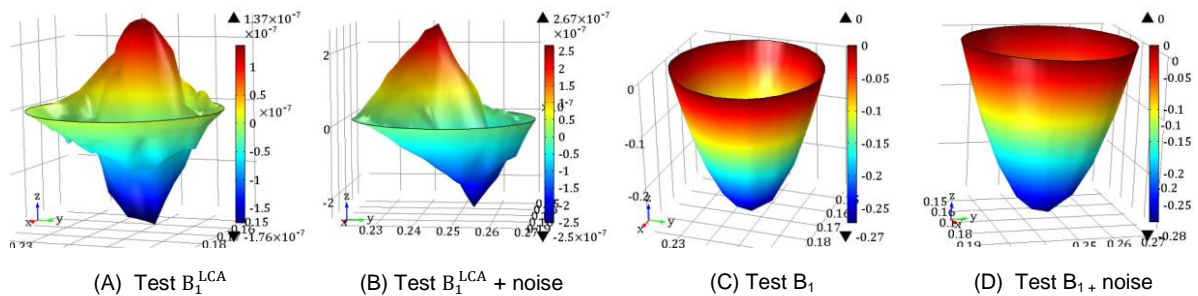
Figure 39: Difference between velocity magnitude of the solution of the study using in-silico Data B and velocity magnitude computed from controlled (A) controlled Test B_1^{LCA}, (B) controlled Test B_1^{LCA} with noise, (C) controlled Test B_1 and (D) controlled Test B_1 with noise, at outlet BA cross-section. Scale units: m/s.

In Figure 38, the outlet BA cross-section is represented for Data B (Figure 38 - A), Test B_1^{LCA} (Figure 38 - B) , Test B_1^{LCA} with noise (Figure 38 - C), Test B_1 (Figure 38 - D) and Test B_1 with noise (Figure 38 - E). A fully developed profile can be observed for all studies, with maximum velocity obtained at the artery's centre. Maximum velocity is higher for Test B_1 (0.52 m/s) than for Test B_1^{LCA} (0.25 m/s), which show similar values to the in-silico Data B because the same BC was attributed.

In Figure 39, the difference between the in-silico data and (A) Test B_1^{LCA} , (B) Test B_1^{LCA} with noise, (C) Test B_1 and (D) Test B_1 with noise, at outlet BA, is presented. While differences in (A) and (Figure 39 - B) are negligible ($\sim 10^{-7}$ m/s), in (Figure 39 - C) and (Figure 39 - D) are in the same order as the velocity and showing a parabolic profile. Higher differences can be found at the centre of the vessel (-0.25 m/s), while the wall, due to the same imposed no-slip condition, does not show any difference.

(A) Data B   (B) Test B_1^{LCA} (C) Test B_1^{LCA} + noise   (D) Test B_1 (E) Test B_{1+} noise
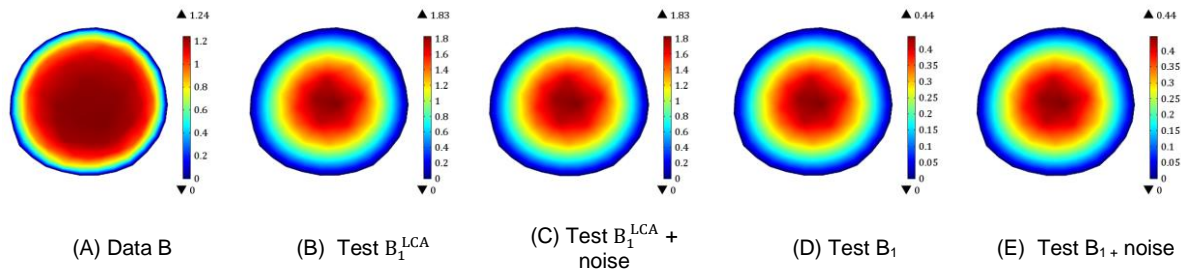
Figure 40: Distribution of velocity magnitude on the outlet LCA cross-section, computed from (A) in-silico Data B, generated with MLBC with exponent $\alpha = 3$ in LCA, and TFBC in the outlets BA and LSA; (B) controlled Test B_1^{LCA} , (C) controlled Test B_1^{LCA} with noise, (D) controlled Test B_1 and (E) controlled Test B_1 with noise. Scale units: m/s.

(A) Test B_1^{LCA} (B) Test B_1^{LCA} + noise   (C) Test B_1 (D) Test B_{1+} noise
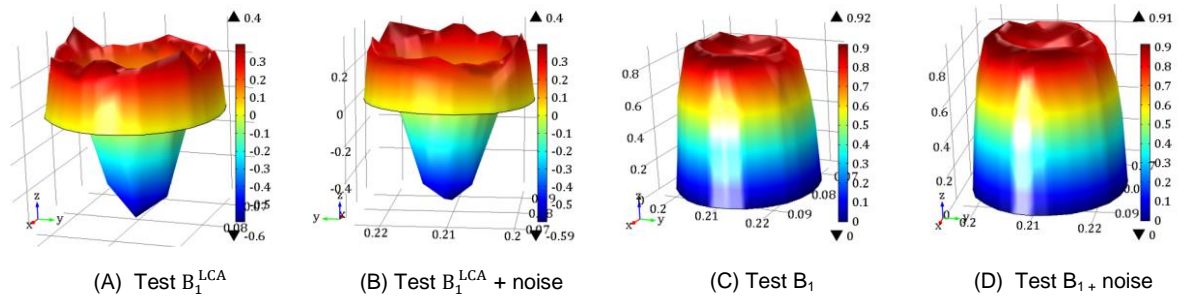
Figure 41: Difference between velocity magnitude of the solution of the study using in-silico Data B and velocity magnitude computed from controlled (A) controlled Test B_1^{LCA} , (B) controlled Test B_1^{LCA} with noise, (C) controlled Test B_1 and (D) controlled Test B_1 with noise, at outlet LCA cross-section. Scale units: m/s.

In Figure 40, the cross-section at LCA is studied, which was the outlet where TFBC was attributed when generating the in-silico data (Data B). For Data B, a flatter profile is observed compared to the optimisation tests. For in-silico data solution there are fewer levels of segmentation of the velocity magnitude, with the highest value being reached closer to the vessel wall; for the tests' solutions, there is an apparent and paced increase of the velocity until a maximum velocity closer to the centre. In this outlet, a more considerable discrepancy can be seen between the different solutions. Test B_1^{LCA}, where the only unknown parameter was imposed, shows higher velocities ($1.83\ \mathrm{ms^{-1}}$), followed by Data B ($1.24\ \mathrm{ms^{-1}}$) and finally, Test B_1 ($0.44\ \mathrm{ms^{-1}}$).

In Figure 41, the difference between the in-silico data and (Figure 41 - A) Test B_1^{LCA} , (Figure 41 - B) Test B_1^{LCA} with noise, (Figure 41 - C) Test B_1 and (Figure 41 - D) Test B_1 with noise, at outlet LCA, is compared. All differences are in the same order as the velocity. For differences in (A) and (B), values range from -0.5 m/s in centre of the vessel to 0.4 m/s closer to the wall (but not in the wall due to non-slip condition).

As seen before, for Data B, velocity achieves higher values closer to the wall, therefore, in order for Test B_1^{LCA} become more parabolic in comparison to Data B, needs to have lower values in the zone

(positive difference), while the centre of Test B_1^{LCA} needs an increase in velocity (negative difference). For Test B_1, the flow imposed by a parameter much higher than the one obtained for Test B_1^{LCA}, implies much lower velocity in this outlet. For the flow to become more parabolic than Data B, larger decreases must happen closer to the wall, as seen in Figure 41.

Finally, in Figure 42, section LSA is observed. Again, in all studies, a fully developed flow can be seen with Test B_1 achieving higher velocities (0.48 m/s) than Data B/ Test B_1^{LCA} (0.19 m/s), which again have the same velocity because the boundary condition is the same.

(A) Data B   (B) Test B_1^{LCA} (C) Test B_1^{LCA} + noise   (D) Test B_1 (E) Test B_{1+} noise
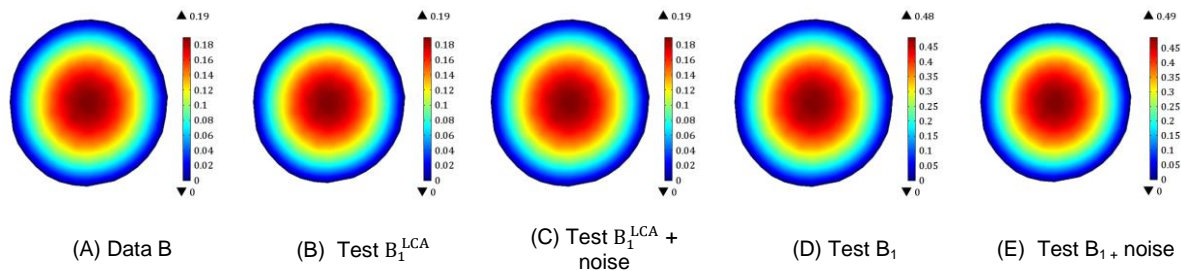
Figure 42: Distribution of velocity magnitude on the outlet LSA cross-section, computed from (A) in-silico Data B, generated with MLBC with exponent $\alpha = 3$ in LCA, and TFBC in the outlets BA and LSA; (B) controlled Test B_1^{LCA} , (C) controlled Test B_1^{LCA} with noise, (D) controlled Test B_1 and (E) controlled Test B_1 with noise. Scale units: m/s.

The differences between the in-silico data and the tests, Figure 43, follow the same patterns and magnitude as seen for outlet BA (Figure 39).

(A) Test B_1^{LCA} (B) Test B_1^{LCA} + noise   (C) Test B_1 (D) Test B_{1+} noise
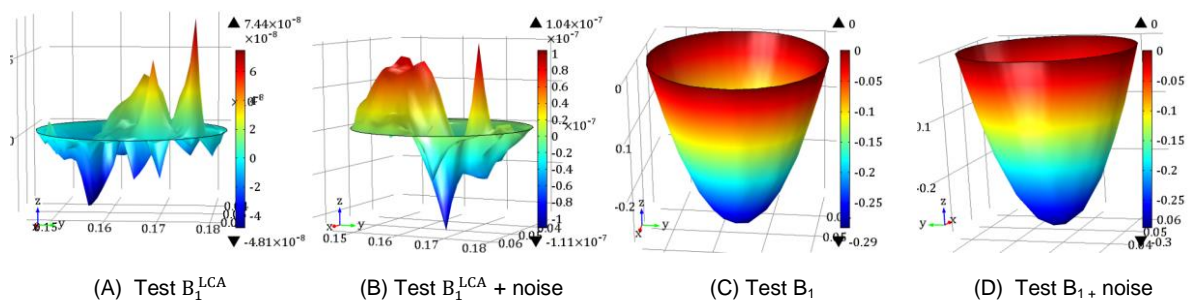
Figure 43: Difference between velocity magnitude of the solution of the study using in-silico Data B and velocity magnitude computed from controlled (A) controlled Test B_1^{LCA} , (B) controlled Test B_1^{LCA} with noise, (C) controlled Test B_1 and (D) controlled Test B_1 with noise, at outlet LSA cross-section. Scale units: m/s.

Studying each outlet alone is easier to understand that maximum velocities obtained for Test B_1 are similar in all outlets, as expected. For these studies, while for outlets BA and LSA, there is an overestimation of the velocity compared to Data B, for LCA, the velocity is underestimated.

In Figure 44, the streamlines for Data B (Figure 38 - A), Test B_1^{LCA} (Figure 44 - B) , Test B_1^{LCA} with noise (Figure 44- C), Test B_1 (Figure 44 - D) and Test B_1 with noise (Figure 44- E), are following the literature that states that highest velocities are seen in the descending aorta and lowest in the ascending aorta. [117], [118]

Also, as noticed in previous visualisations, at the inlet, the velocity profile is fully developed. Some recirculation of the flow can be observed, with insignificant velocities, in the aortic arch exit. Higher velocities can occur in the descendant aorta closer to the outer wall of the curvature. This phenomenon appears due to the initial fully-developed flow, characterised by high velocities in the centre, which imply

high inertia, and lower velocities near the wall, subjected to less inertia. For this reason, when the blood is forced to change its direction and accelerate, due to the curvature of the geometry, the most significant displacements occur where there is less inertia, near the outer vessel wall.

For Test B_1^{LCA} despite higher velocities, those are concentrated only in the outlet LCA.

(A) Data B   (B) Test B_1^{LCA} (C) Test B_1^{LCA} + noise

(D) Test B_1 (E) Test B_1 + noise
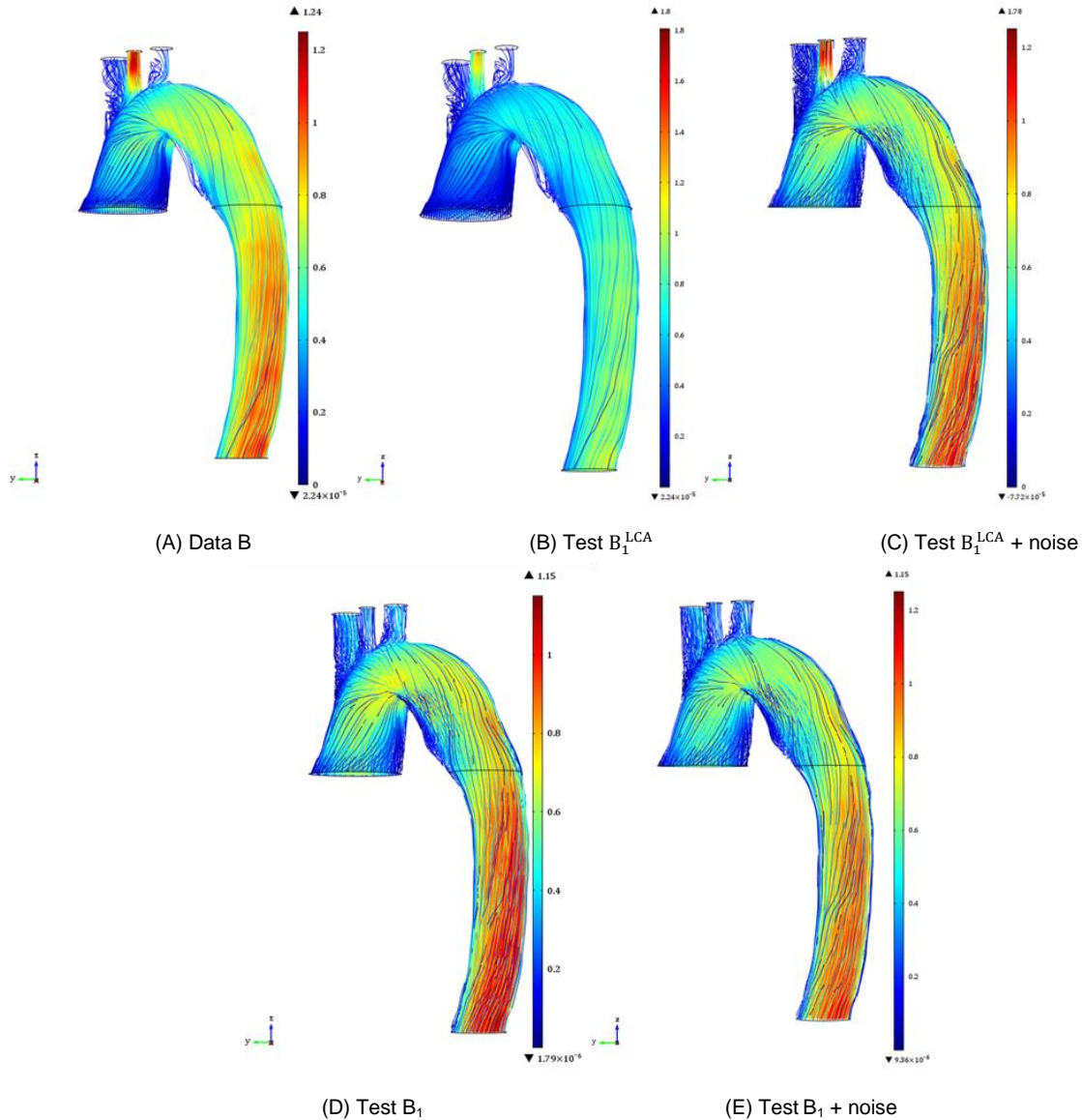
Figure 44: Streamline plots on the fluid domain, computed from the solution of the studies: (A) in-silico Data B, generated with MLBC with exponent $\alpha = 3$ in LCA, and TFBC in the outlets BA and LSA; (B) controlled Test B_1^{LCA} , (C) controlled Test B_1^{LCA} with noise, (D) controlled Test B_1 and (E) controlled Test B_1 with noise. Scale units: m/s. The streamlines have a colour expressing the velocity magnitude in m/s.

4.2.3. Recovering Data C

In this section, the flow will be recovered from Data C, generated by attributing TFBC $(P = 0)$ to all supra-aortic outlets. Again, the MLBC was attributed to the three supra-aortic outlets, with one control optimising a single parameter (α_1) - Test C_1 - or with three controls optimising a different parameter in each of the supra-aortic outlets $(\alpha_1, \alpha_2, \alpha_3)$ - Test C_3. Test C_1 was also repeated, considering noise (Test C_1 + noise). The ranges of the controls used can be found in Section 3.1.1.2.

Table 16 contains the optimised exponent parameters of ML for each test. As seen for the two previous sections, the parameters obtained for the two tests (Test C_1 and Test C_3) are similar, and as the diameter decreases, the parameters value increase. The results between Test C_1 and Test C_2 and Test C_1 and Test C_1 + noise are very similar. Therefore, only Test C_1 will be analysed in detail.

Table 16: Murray's Law parameters obtained by solving Test C_1, with and without noise, and Test C_3.

Test	α_1	α_2	α_3
C_1	1.4731	-	-
C_1 + noise	1.4734	-	-
C_3	1.4722	1.4742	1.4733

Table 17 contains the errors of the domain, of the section used for the optimisation problem (S_{obs}), and of the descendent aorta, as well as the objective value obtained. An additional test was added (Test $C_{control}$) as a comparison. In this test, the supra-aortic outlets' BCs were forced to be the classic ML with $\alpha = 3$. In general, errors are considerably greater in this test than the ones where the parameters were adjusted automatically. Absolute errors for all tests are around 0.01%, while for the control is 0.15%. The relative error in the domain is around 3.8%, for all tests, which is considered acceptable and is lower than seen for Test B_1 and B_3. For Test $C_{control}$, the relative error is 58%. As seen before, S_{obs}'s errors can be neglected since it is used as the optimisation stop and needs to be as small as defined in the Objective Function. The relative error in the descent aorta is significantly lower than the domain's (~0.2%), in all tests.

Table 18 refers to the errors in the supra-aortic outlets. Higher relative errors can be seen for all outlets with outlet LCA with the highest (~45%), followed by LSA (~35%) and BA (~34%). Here is observable again the significant drop in the magnitude error, driven by the imposition of a parabolic profile in the control outlet. The error magnitude for LSA is around 3.2% while for BA is 8.4%. Larger errors are still seen for LCA (20.8%).

Table 17 Absolute errors, relative errors and magnitude in the domain, section S_{obs} and outlet DA of the controlled solutions obtained by solving Test C_1, with and without noise, and Test C_3.

Test	Domain		S_{obs} Section			Outlet DA		
	Abs. Error	Rel. Error	Abs. Error	Rel. Error	Mag.	Abs. Error	Rel. Error	Mag.
C_1	1.0E-04	3.8E-02	2.3E-05	3.7E-03	5.3E-12	1.7E-05	2.4E-03	8.3E-04
C_1 + noise	1.0E-04	3.8E-02	2.3E-05	3.7E-03	-2.9E-04	1.6E-05	2.3E-03	5.3E-04
C_3	1.0E-04	3.7E-02	2.3E-05	3.7E-03	1.4E-12	1.6E-05	2.3E-03	8.1E-04
$C_{control}$	1.5E-03	5.8E-01	4.1E-03	6.5E-01	-6.4E-01	4.5E-03	6.3E-01	-6.5E-01

Table 18: Absolute errors, relative errors and magnitude in the supra-aortic outlets (Outlet BA, Outlet LCA and Outlet LSA) of the controlled solutions obtained by solving Test C_1, with and without noise, and Test C_3.

Test	Outlet BA			Outlet LCA			Outlet LSA		
	Abs. Error	Rel. Error	Mag.	Abs. Error	Rel. Error	Mag.	Abs. Error	Rel. Error	Mag.
C_1	1.7E-03	3.4E-01	8.4E-02	1.3E-03	4.5E-01	-2.1E-01	1.4E-03	3.5E-01	3.2E-02
C_1 + noise	1.7E-03	3.4E-01	8.4E-02	1.3E-03	4.5E-01	-2.1E-01	1.4E-03	3.5E-01	3.2E-02
C_3	1.7E-03	3.4E-01	8.3E-02	1.3E-03	4.5E-01	-2.1E-01	1.4E-03	3.5E-01	3.2E-02
$C_{control}$	4.1E-03	8.2E-01	8.2E-01	2.6E-03	9.0E-01	9.0E-01	3.6E-03	8.8E-01	8.8E-01

We can observe that higher velocities are achieved before reaching the outlets in both solutions (Figure 45). For Test C_1 the flow is less skewed along the curvature of the aorta.

(A) Data C   (B) Test C_1 (C) Test C_1 + noise
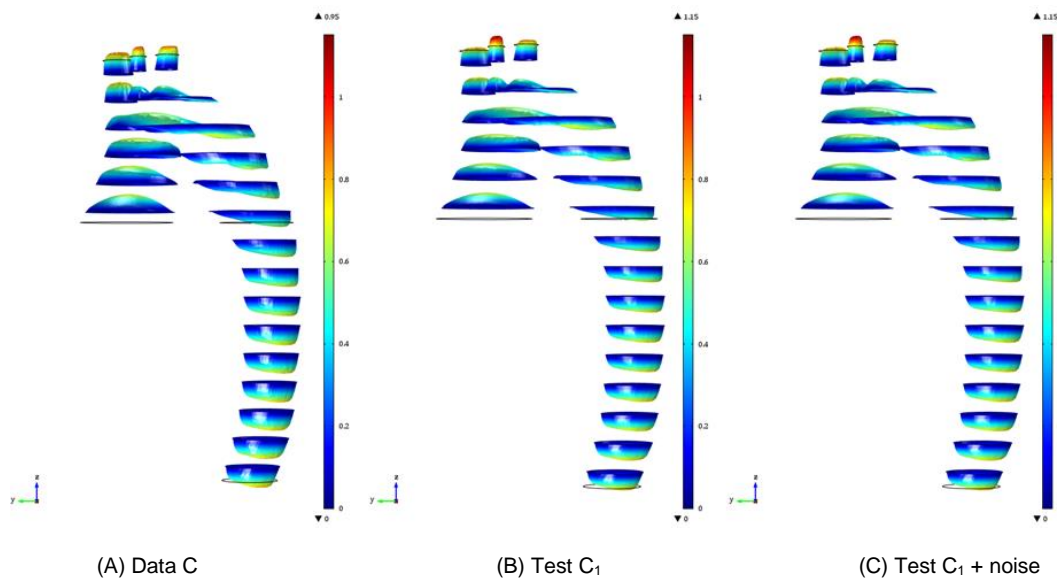
Figure 45: Distribution of velocity magnitude and direction on 15 slices of the domain, computed from the solution of the studies: (A) in-silico Data C, generated with TFBC in the supra-aortic outlets; (B) controlled Test C_1 and (C) controlled Test C_1 with noise. Scale units: m/s.

The next three figures (Figure 46 - Figure 48) show the distribution of flow across the supra-aortic outlets (column A) and the inlet and descendent aorta (column B), for Data C (Figure 46), Test C_1 (Figure 47) and Test C_1 with noise (Figure 48).

In Data C (Figure 46), there is a skew of velocity in BA towards the aorta's interior. Differences between the velocity obtain in LCA in both studies is higher, with LCA showing in Test C_1 (Figure 47) the maximum velocity and significantly higher than in the remaining outlets. While for the in-silico data, the velocities among outlets are similar. For the in-silico Data C, the maximum velocities obtained were similar for all outlets – ranging from 0.93 m/s for LSA, 0.98 m/s for BA and 0.99 m/s for LCA. On the other hand, the range for velocities for the Test C_1 is winder – 1.27 m/s for outlet BA, 1.49 m/s for outlet LSA and finally, 1.74 m/s for outlet LCA. The larger the diameter, the lower was the velocities obtained. The non-split condition for all figures is also observed, with velocities being zero in the vessel wall.

(A) Data C: superior view   (B) Data C: inferior view
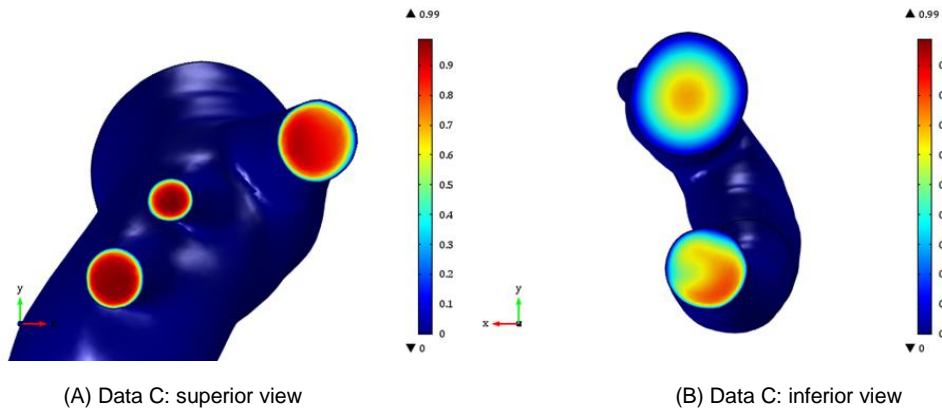
Figure 46: Distribution of the magnitude of velocity at (A) the surface of the supra-aortic outlets (B) and descendent aorta and inlet, computed from the solution of the study using in-silico Data C, generated with TFBC in the supra-aortic outlets. Scale units: m/s.

(A) Test C_1: superior view   (B) Test C_1: inferior view
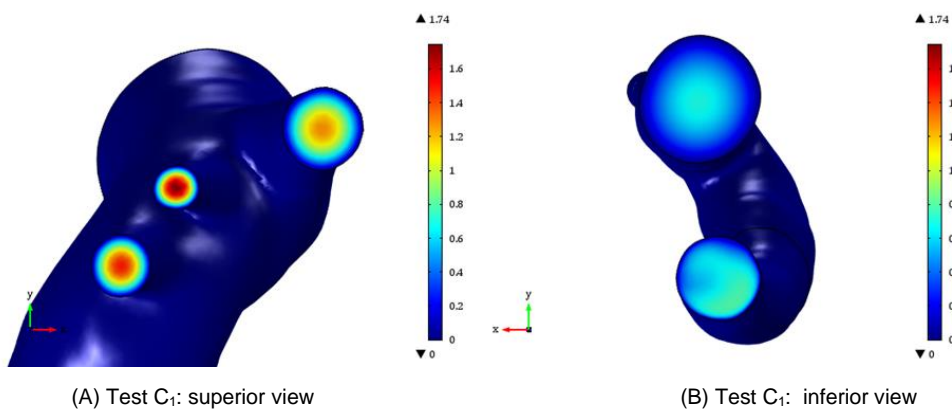
Figure 47: Distribution of the magnitude of velocity at (A) the surface of the supra-aortic outlets (B) and descendent aorta and inlet, computed from the solution of the controlled Test C_1. Scale units: m/s.

(A) Test C_1 + noise: superior view   (B) Test C_1 + noise: inferior view
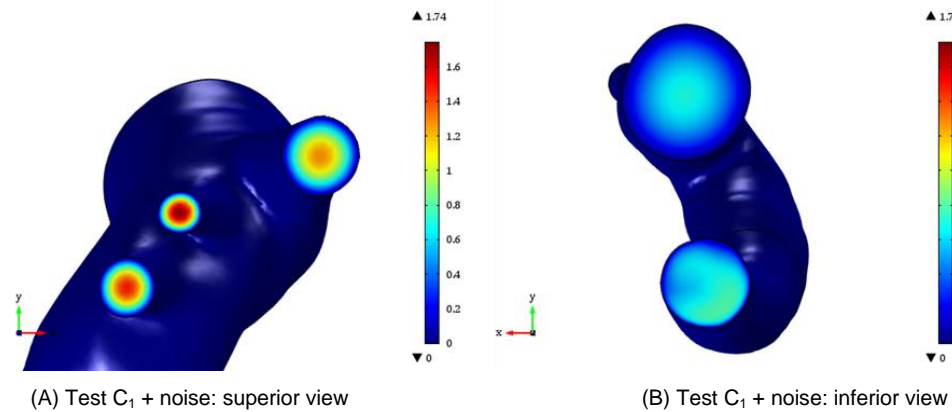
Figure 48: Distribution of the magnitude of velocity at (A) the surface of the supra-aortic outlets (B) and descendent aorta and inlet, computed from the solution of the controlled Test C_1 with noise. Scale units: m/s.

As seen before, the traction free boundary condition results in a flatter profile than the Murray's Law boundary condition. This can be easily observed in Figure 49 - Figure 51, for all outlets, where for Data C, the maximum velocity is achieved closer to the wall and occupies a more significant proportion of the vessel. For Test C_1, the transition between velocities is more defined by a circular 'doughnut' for each velocity, from zero in the wall to the maximum at the centre. This is the description of a parabolic profile. Additionally, a slight skew of maximum velocities can be observed, in both outlet BA and LSA,

72

which is confirmed in column 3, where the highest positive values of difference are not across the entire vessel. On the other hand, for outlet LCA, the difference can be seen all around the aorta next to the wall.

In Figure 49 (BA), Figure 50 (LCA) and Figure 51 (LSA), the difference between the in-silico data and (A) Test C_1 and (B) Test C_1 with noise at each respective outlet, can be observed.

As seen in Section 4.2.2, for outlet LCA, the velocity profile from the in-silico data is different from the one obtained as the solution for the tests. In these figures. All differences are in the same order as the velocity. For differences in (A) and (B), values range from -0.4 m/s in centre of the vessel to 0.4 m/s closer to the wall (but not in the wall due to non-slip condition). As seen before, for Data C, velocity achieves higher values closer to the wall, and therefore, in order for any test to become more parabolic in comparison to Data C, it needs to have lower values in the zone (positive difference), while the centre needs an increase in velocity (negative difference).

| (A) Data C | (B) Test C_1 | (C) Test C_1 + noise | (D) Test C_1 | (E) Test C_1 + noise |
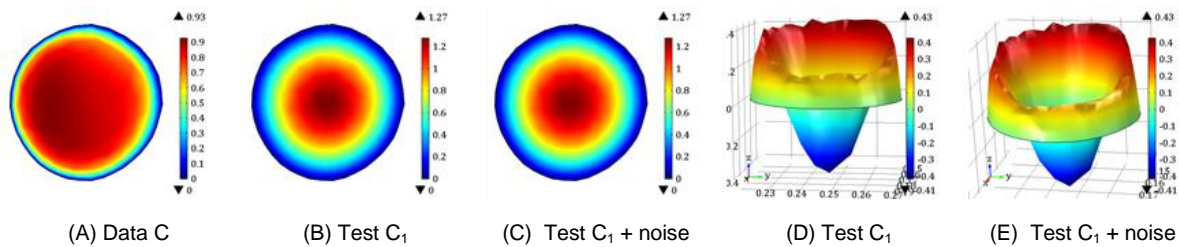
Figure 49: Distribution of velocity magnitude on the outlet BA cross-section, computed from (A) Data C, (B) Test C_1, (C) Test C_1 with noise. Difference between velocity magnitude of the study's solution using in-silico Data C and velocity magnitude computed from (D) controlled Test C_1 and (E) controlled Test C_1 with noise, at outlet BA cross-section. Scale units: m/s.

| (A) Data C | (B) Test C_1 | (C) Test C_1 + noise | (D) Test C_1 | (E) Test C_1 + noise |
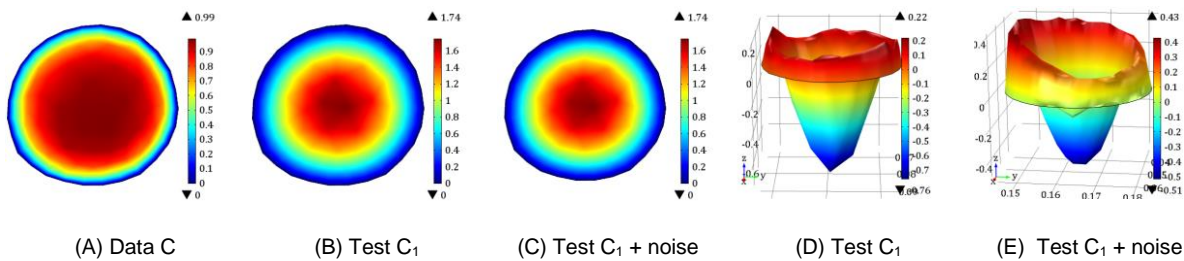
Figure 50: Distribution of velocity magnitude on the outlet LCA cross-section, computed from (A) Data C, (B) Test C_1, (C) Test C_1 with noise. Difference between velocity magnitude of the solution of the study using in-silico Data C and velocity magnitude computed from (D) controlled Test C_1 and (E) controlled Test C_1 with noise, at outlet LCA cross-section. Scale units: m/s.

| (A) Data C | (B) Test C_1 | (C) Test C_1 + noise | (D) Test C_1 | (E) Test C_1 + noise |
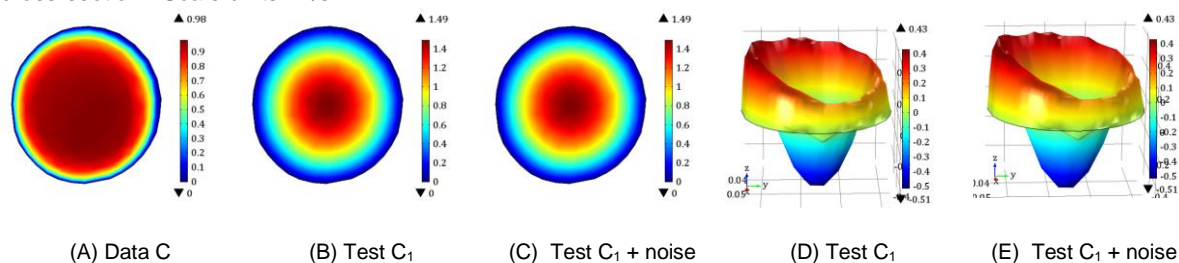
Figure 51: Distribution of velocity magnitude on the outlet LSA cross-section, computed from (A) Data C, (B) Test C_1, (D) Test C_1 with noise. Difference between velocity magnitude of the solution of the study using in-silico Data C and velocity magnitude computed from (D) controlled Test C_1 and (E) controlled Test C_1 with noise, at outlet LSA cross-section. Scale units: m/s.

The flow in LCA is overestimated, while in BA and LSA is underestimated, according to Table 19.

Table 19: Average flow rate of the controlled solutions obtained by solving Test C_1, with and without noise, and Test C_3, in the supra-aortic outlets (Outlet BA, Outlet LCA and Outlet LSA), in the descendent aorta (Outlet DA) and the total outflow. Corresponding proportion (%) of flow rate in each outlet in relation to the outflow. The flow rate of Data C solution for comparison.

Test	Outlet BA		Outflow LCA		Outflow LSA		Outlet DA		Total Outflow
	(m/s^2)	(%)	(m/s^2)	(%)	(m/s^2)	(%)	(m/s^2)	(%)	(m/s^2)
C_1	2.9E-05	20.4%	1.24E-05	8.7%	1.91E-05	13.4%	8.20E-05	57.5%	1.4E-04
C_1 + noise	2.9E-05	20.4%	1.24E-05	8.7%	1.91E-05	13.4%	8.19E-05	57.5%	1.4E-04
C_3	2.9E-05	20.5%	1.24E-05	8.7%	1.91E-05	13.4%	8.18E-05	57.4%	1.4E-04
Data C	3.2E-05	22.1%	1.0E-05	7.2%	1.97E-05	13.7%	8.19E-05	57.0%	1.4E-04

4.3. Validation with aortic coarctation

In this section, the framework developed in Section 3.1 will be applied to an aorta with coarctation (CoA). The flow will be recovered from data (Data P) generated by attributing patient-specific data as the inflow BC and using patient-specific data in the objective function. The remaining supra-aortic outlets were given MLBC with $\alpha = 3$, and the outlet DA was left with a 'do-nothing' approach. For the controlled study, the MLBC was attributed to the three supra-aortic outlets, associated with a single optimising parameter (α_1) - Test P_1. In this section, a detailed analysis will be done for Test P_1.

As a comparison, two additional tests (Test P_3, Test P_v) were performed using Data P and three tests (Test Q_1, Test Q_3 and Test Q_v) with Data Q, which was generated with TFBC in all supra-outlets instead for MLBC. In Test P_v and Q_v, instead of a BC assuming a laminar profile (where L_{entr} is given, and therefore the flow is fully-developed), a velocity BC was attributed.

The bounds for the controls used in this section can be found in Table 6 (Section 3.3.2.), and the detailed tests in Table 5. A brief comparison between these tests will be made at the end of this section.

Table 20 contains the optimised exponent parameters of ML for all tests performed. For Test P_1, the obtained parameter $(\alpha = 5.5296)$ is considerably higher when comparing to the tests done in Section 4.2. With the abrupt decline in the aorta radius in the coarctation area, the velocity significantly increases $(V_{mean}^{in} = 0.3539\,m/s, V_{mean}^{coart} = 2.76\,m/s)$, therefore the majority of the flow must go into the DA instead of into the supra-aortic outlets. For that to happen, the ratio $(D_i/D_{in})^{\alpha}, i \in (BA, LCA, LSA)$ needs to be small, which is accomplished by a higher α (since $D_{in} > D_i$).

Table 20: Murray's Law parameters obtained by solving the CoA tests mentioned in Section 3.3.2.

Test	α_1/β_1	α_2	α_3
P_1	5.5296	-	-
P_3	5.9972	4.2723	4.3380
P_v	3.3576	-	-
Q_1	5.4765	-	-
Q_3	5.9972	4.2723	4.3380
Q_v	3.3576	-	-

Table 21 shows that by having a much larger α, around 99% of the flow goes towards the DA while for an $\alpha = 3$ that number drops to 91%. For both Data P and Test P_1, outlet BA obtains almost all the flow that goes into the supra-aortic outlets, which from a physiological point of view is not true. The difference in the flow rate from Data P to Test P_1 is around 98% for outlets LSA and LCA, 90% for outlet BA and 9.3% outlet DA.

Table 21: Average flow rate of the controlled solutions obtained by solving the CoA tests mentioned in Section 3.3.2. in the supra-aortic outlets (Outlet BA, Outlet LCA and Outlet LSA), in the descendent aorta (Outlet DA) and the total outflow. Corresponding proportion (%) of flow rate in each outlet in relation to the outflow.

| Test | Outlet BA | | Outflow LCA | | Outflow LSA | | Outlet DA | | Total Outflow |
	(m/s^2)	(%)	(m/s^2)	(%)	(m/s^2)	(%)	(m/s^2)	(%)	(m/s^2)
Data P	2.1E-05	6.7%	3.39E-06	1.1%	3.70E-06	1.2%	2.80E-04	91.0%	3.1E-04
Test P_1	2.1E-06	0.7%	7.71E-08	0.0%	9.00E-08	0.0%	3.06E-04	99.3%	3.1E-04
Test P_3	1.4E-06	0.5%	5.05E-07	0.2%	5.18E-07	0.2%	3.06E-04	99.2%	3.1E-04
Test P_v	2.2E-06	0.7%	8.11E-08	0.0%	9.47E-08	0.0%	3.05E-04	99.2%	3.1E-04
Data Q	1.5E-04	43.7%	4.75E-05	13.8%	4.49E-05	13.1%	1.01E-04	29.4%	3.4E-04
Test Q_1	2.2E-06	0.7%	8.35E-08	0.0%	9.73E-08	0.0%	3.05E-04	99.2%	3.1E-04
Test Q_3	1.4E-06	0.5%	5.05E-07	0.2%	5.18E-07	0.2%	3.06E-04	99.2%	3.1E-04
Test Q_v	2.2E-06	0.7%	8.11E-08	0.0%	9.47E-08	0.0%	3.05E-04	99.2%	3.1E-04

Table 22 contains the errors of the domain, of the section used for the optimisation problem (S_{obs}), and of the descendent aorta. Absolute error is around 0.1%, which, although very small, is higher than what was seen for the tests presented in (Section 4.2). The relative error in the domain is around 9.8%. This is driven by the errors in the supra-aortic outlets (Table 23) because an MLBC with $\alpha = 3$ was imposed in Data P, which might not be the reality and it is difficult to confirm due to the complexity of acquiring patient-specific data. The discrepancy in the patient-specific data might also drive these errors: while the literature gives the velocity at the inlet, the pressure at the S_{obs} is obtained by the patient's hemodynamic gradient test.

Table 22: Absolute errors, relative errors and magnitude in the domain, section S_{obs} and outlet DA of the controlled solutions obtained by solving the CoA tests mentioned in Section 3.3.2.

| Test | Domain | | S_{obs} Section | | | Outlet DA | | |
	Abs. Error	Rel. Error	Abs. Error	Rel. Error	Mag.	Abs. Error	Rel. Error	Mag.
P_1	1.1E-03	9.8E-02	2.6E-03	9.4E-02	-9.4E-02	1.6E-03	9.3E-02	-9.3E-02
P_3	1.1E-03	9.7E-02	2.6E-03	9.4E-02	-9.3E-02	1.6E-03	9.3E-02	-9.3E-02
P_v	1.1E-03	9.7E-02	2.6E-03	9.4E-02	-9.3E-02	1.6E-03	9.3E-02	-9.3E-02
Q_1	8.4E-03	1.5E+00	2.0E-02	2.0E+00	-2.0E+00	1.2E-02	2.0E+00	-2.0E+00
Q_3	8.4E-03	1.5E+00	2.0E-02	2.0E+00	-2.0E+00	1.2E-02	2.0E+00	-2.0E+00
Q_v	8.4E-03	1.5E+00	2.0E-02	2.0E+00	-2.0E+00	1.2E-02	2.0E+00	-2.0E+00

For the errors at the supra-aortic outlets (Table 23), as explained before, are driven by the big discrepancy in the obtained parameter α. Nevertheless, since we attributed a laminar outflow profile, the errors and the magnitudes are in the same order. This can be confirmed in Figure 53 (Data P) and Figure 54 (Test P_1), where the profiles in each outlet and S_{obs} are similar, but the magnitude of the velocity different. Also, ML assumes a circular vessel, which is not the case for outlet BA and could be

an additional factor of higher error values. Despite considerably high errors in the supra-aortic outlets, the absolute error in the outlet DA is around 0.2%, and the relative error around 9.3% (<10%).

Table 23: Absolute error, relative error, and magnitude in the supra-aortic outlets (Outlet BA, Outlet LCA and Outlet LSA) of the controlled solutions obtained by solving the CoA tests mentioned in Section 3.3.2.

Test	Outlet BA			Outlet LCA			Outlet LSA		
	Abs. Error	Rel. Error	Mag.	Abs. Error	Rel. Error	Mag.	Abs. Error	Rel. Error	Mag.
P_1	1.6E-03	9.3E-02	-9.3E-02	1.6E-03	9.3E-02	-9.3E-02	1.6E-03	9.3E-02	-9.3E-02
P_3	1.6E-03	9.3E-02	-9.3E-02	1.6E-03	9.3E-02	-9.3E-02	1.6E-03	9.3E-02	-9.3E-02
P_v	1.6E-03	9.3E-02	-9.3E-02	1.6E-03	9.3E-02	-9.3E-02	1.6E-03	9.3E-02	-9.3E-02
Q_1	1.2E-02	2.0E+00	-2.0E+00	1.2E-02	2.0E+00	-2.0E+00	1.2E-02	2.0E+00	-2.0E+00
Q_3	1.2E-02	2.0E+00	-2.0E+00	1.2E-02	2.0E+00	-2.0E+00	1.2E-02	2.0E+00	-2.0E+00
Q_v	1.2E-02	2.0E+00	-2.0E+00	1.2E-02	2.0E+00	-2.0E+00	1.2E-02	2.0E+00	-2.0E+00

The solutions at several cross-sections along the aorta, representing both velocity's magnitude and direction, can be found in Figure 52, for Data P (Figure 52-A) and Test P_1 (Figure 52-C). As expected, maximum velocities are found near the coarctation, with the flow higher at the end of the aortic arch skewing towards the interior of the aorta, unlike what was seen in the previous tests, where the higher values of flow were found near the outer wall in the descending aorta. Also, in Figure 52-C (Data P) and Figure 52-D (Test P_1), despite the higher velocities near the CoA, we can observe some recirculation at the beginning of the descendent aorta but not right after the CoA.

(A) Data P: Velocity Magnitude   (B) Test P_1: Velocity Magnitude   (C) Data P: Streamlines   (D) Test P_1: Streamlines
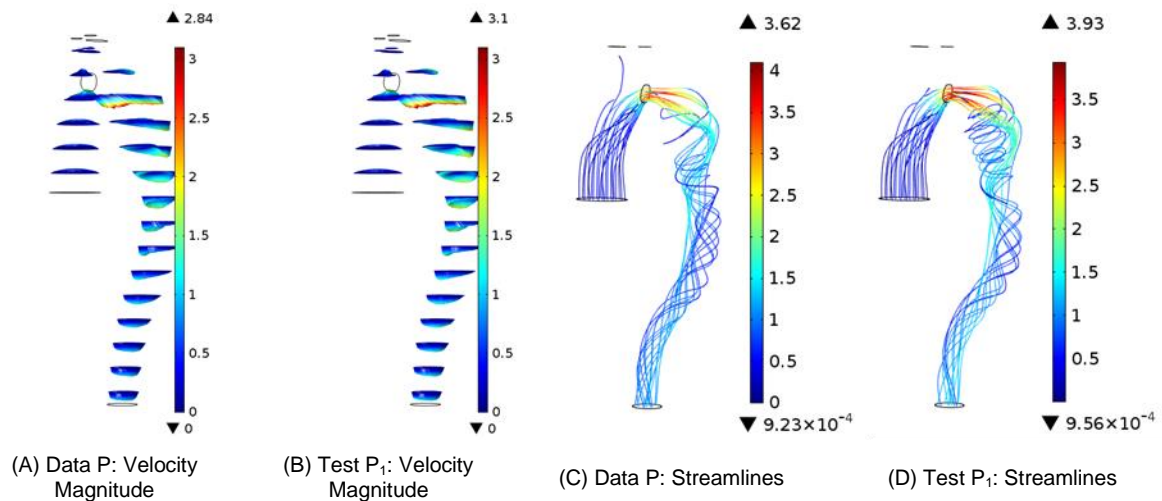
Figure 52: Distribution of velocity magnitude and direction on 15 slices of the domain, computed from the solution of the studies: (A) patient-specific Data P and (B) controlled Test P_1. Scale units: m/s. Streamline plots on the fluid domain, computed from the solution of the studies: (C) patient-specific Data P and (D) controlled Test P_1. The streamlines have a colour expressing the velocity magnitude in m/s. Scale units: m/s.

First, for both Data P (Figure 53 – (A) to (E)) and Test P_1 (Figure 54– (A) to (E)), the profiles seen for all sections are similar. Secondly, the attribution of outflow laminar profiles in outlets BA, LCA and LSA explains the parabolic profile observed in both figures, although much higher values for Data P. For the outlet DA, there is a slight skew of higher velocities towards the aorta's outer wall in both simulations, which was already discussed in previous sections. As expected, velocities in the outlet DA are much higher than velocities in the supra-aortic outlets. Finally, for section S_{obs}, which corresponds to the CoA,

values for Test P_1 are in accordance with the hemodynamic gradient given, as expected. The CoA velocity is much higher (x3) than in the DA driven by the narrowing of the vessel. In this section observable a skew of higher velocity values towards the interior of the aortic arch.

| (A) Data P: Outlet DA | (B) Data P: Outlet BA | (C) Data P: Outlet LCA | (D) Data P: Outlet LSA | (E) Data P: S_{obs} |
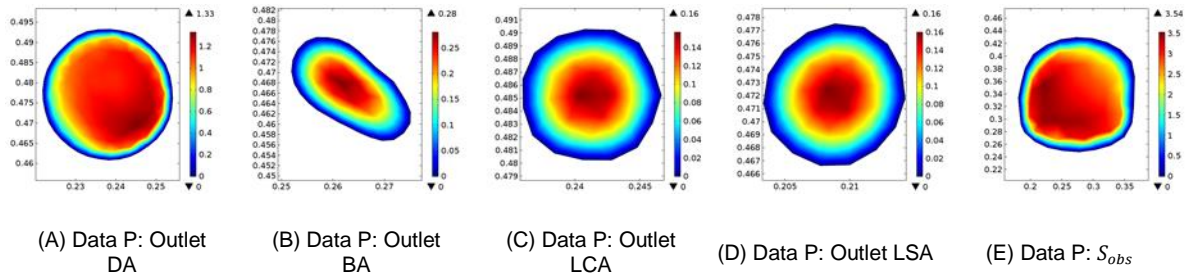
Figure 53: Distribution of velocity magnitude from the patient-specific Data P, on the (A) outlet DA, (B) outlet BA, (C) outlet LCA, (D) outlet LSA and (E) S_{obs}. Scale units: m/s.

| (A) Test P_1: Outlet DA | (B) Test P_1: Outlet BA | (C Test P_1: Outlet LCA | (D) Test P_1: Outlet LSA | (E) Test P_1: S_{obs} |
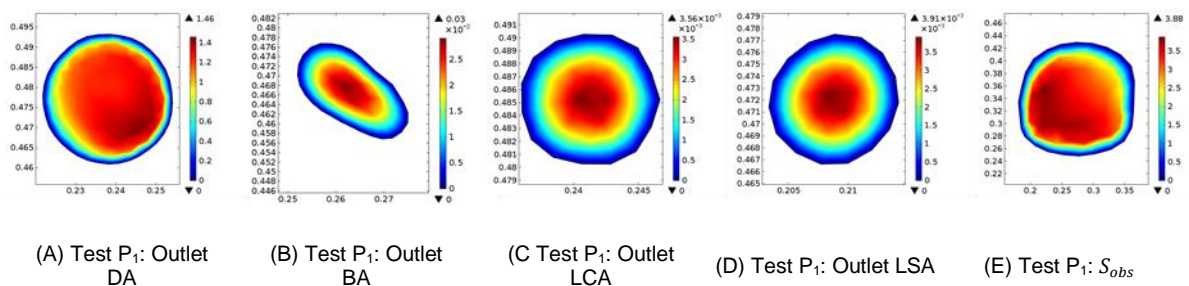
Figure 54: Distribution of velocity magnitude from the controlled Test P_1, on the (A) outlet DA, (B) outlet BA, (C) outlet LCA, (D) outlet LSA and (E) S_{obs}. Scale units: m/s.

When comparing all the CoA tests, the first observation is that the controlled parameter obtained (Table 20) is similar in the same type of tests, regardless of the data used (Data P or Data Q). For example, α_1 in Test Q_3 is similar to α_1 in Test Q_3, while β_1 in Test P_v is similar to β_1 in Test Q_v. The fact that the same values were obtained regardless of the data used confirms the method's validity, even if the flux in the outlets is not well adjusted to the real data. Moreover, as seen in Section 4.2, the parameters show different values as seen in the literature [94], with the tests using a non-laminar profile approach with the closest values to $\alpha = 3$. In this case, the values obtained as parameters for the CoA were higher than the ones for the normal aorta.

Additionally, unlike what was obtained for the tests in the previous section, when using a different control per each outlet (Test P_3 and Test Q_3) the values obtained are considerably difference, mainly between the parameter for the outlet BA (α_1) and the remaining ones. These higher values in α_1 reduce the flow rate going into this outlet which, in the end, approximates the proportion of flow in each supra-aortic outlet to what would be expected. However, this outlet BA does not have a circular shape, but an elliptical one, which might influence the results since Murray's Law was developed in pipes.

Similar parameters lead to the same flow rate in each outlet, which can be observed in Table 21. As seen for Test P_1, the velocity in the coarctation reaches much higher values than the outlets' velocity, which means the majority of the flow is directed to the coarctation and consequently to the outlet DA. This explains the low percentages of flow seen for the supra-aortic outlets. Tests P_1, Q_1, P_v and Q_v present the same values for flow rates in the outlets (Outlet DA ~ 99.2%, Outlet BA ~ 0.7%, Outlet LCA ~ 0.0% and Outlet LSA ~ 0.0%), meaning that different ML parameters might lead to the same velocity

in the boundary. Test P_3 and Q_3, on the other hand, are similar between them (Outlet DA ~ 99.2%, Outlet BA ~ 0.5%, Outlet LCA ~ 0.2% and Outlet LSA ~ 0.2%) and goes according to what is expected in the supra-aortic outlets – the flow in the outlet BA being twice the flow in remaining two. Note that for all tests, the flow in the outlet DA is similar. For Data Q, since a TFBC was attributed, the flow rate in each boundary is not dependent on the outlet's diameter, which explains the discrepancy in percentages of flow rate seen in the table, compared to the remaining tests.

Errors - both absolute and relative – are similar for all test, with the absolute error in the domain < 1%. Nevertheless, for tests with Data P, the relative error in the domain is <10% while for the test with Data Q is ~145%, driven by the errors in the outlet DA and the coarctation section. In the supra-aortic outlets, relative errors are in the order of 10^1 and absolute errors around 0.2% for tests with Data P and 1.4% for tests with Data Q.

5. Conclusions, limitations, and future work

Boundary conditions replace the upstream and downstream vasculatures absent in the region of interest in a numerical simulation; therefore, studying boundary conditions is important to substitute the regions with physically accurate and robust alternatives to driving better and more realist computational results. When patient-specific data is not available, the choice of appropriate boundary conditions has been a subject of intensive research, especially in the outlet boundary conditions, where data is even more limited. In this work, a framework to adjust Murray's law boundary conditions using a variational approach was developed in a normal aorta and validated in an aorta with coarctation.

The absolute errors over the domain obtained for both models are small (< 1%), with the normal aorta (where the framework was developed) showing smaller values (<0.03%). Relative errors in the domain are considerably higher but no more than 10%, for both models except for the tests using traction-free boundary conditions in the aorta with coarctation. In these tests, errors were much higher than in any other test, driven by the section's errors with coarctation and the outlet DA.

In general, relative errors in the supra-aortic outlets were higher driven by the laminar profile forced in the boundary conditions. The magnitude of the error was considered to have a better understanding of the true relative error. The best results of magnitude were obtained for the tests using the in-silico data with a traction-free boundary condition (Tests C). Here, for the outlet LSA, for example, the magnitude was around 3.2%. Worst errors were found for tests using traction-free boundary condition in only the outlet LCA (Tests B), where the relative error in LSA reached 154%. For the aorta with coarctation, all outlets show similar errors (~100%).

For the normal aorta, using a single controlled parameter versus three control parameters does not seem to impact the results since the obtained variables are similar. This goes under Murray's law, where all the vessels radius are powered to the same constant ($\alpha = 3$). Values obtained for the normal aorta were under the $\alpha = 3$, varying from $\alpha_x = 1.4$ to $\alpha_x = 3.0$.

Different results were found when applying the framework to an aorta with coarctation. Firstly, the values of the parameters are higher than $\alpha = 3$. Ranging from $\alpha_x = 3.4$ to $\alpha_x = 6.0$. By increasing the parameter α, the ratio between the outlet's diameter and the inlet's diameter becomes smaller, which decreases the flow in the outlet.

Secondly, the use of one controlled parameter versus three controlled parameters impacted the results. Solutions using three controlled parameters show a more balanced proportion of flow in each outlet, under the aorta's physiology. This is achieved by a much larger α_x in the outlet BA comparing to the remaining two outlets.

Finally, different datasets lead to the same results since the objective function was only dependent on the patient-specific velocity, which helps to validate the method developed.

To conclude, using a variational approach is an acceptable method to attribute boundary conditions when patient-specific is not available to provide individual characteristics to the boundary conditions, particularly when an abnormal or defective anatomy is being studied – such as the case of the coarctation. Nevertheless, this work was only the first stage of developing a method that could help to analyse the anatomy and flow in the CoA, and potentially evaluate the gravity of the disease and assist the surgical planning, including the decision of the stent placement. Surpassing the limitations of the

work and improving some of the assumptions, as a next step, could lead to better and more useful results.

As a first step, to acquire a better understanding of the underlying processes and for the sake of computational savings, several simplifying assumptions were considered.

The first simplification was to model the aortic flow as stationary, which is a valid assumption since the interaction with the aortic wall was not considered. Nevertheless, the inclusion of time dependency would have allowed understanding the implications of the cardiac cycle in the output but, on the other hand, it would drive a significant increase in the computational cost, since it would be associated to each time step iteration. A future step in this work could be applying this framework to a time-dependent simulation and the coupling with additional models describing FSI.

Secondly, the flow was also considered laminar. A turbulence or transition model should be considered when studying the aortic arch's hemodynamics since, in pathologies like the aorta's coarctation, the flow is proved to be turbulent.

Moreover, the mesh densities used in the numerical simulations were not the ideal ones, since they have associated a relatively high error. The choice of a less refined mesh was mainly driven by the lack of computational memory needed to assemble the matrixes with a high number of degrees of freedom. Another type of limitations concerns the numerical data used—the lack of patient-specific data forced to generate in-silico data, for the first part of this work. The use of exclusively realistic data would have been an improvement. Additionally, even in the second part of the work, a proxy using literature data for the inflow boundary condition was needed when testing with patient-specific data. Moreover, for the optimisation problem, an average velocity in the coarctation zone was used. A better approach should include a velocity vector.

Another limitation concerns the aorta's data preparation with coarctation, especially the geometry since the image acquisition could introduce some errors. The CT images include artefacts and that in most of the slices differentiation between the TA and the surrounding tissues barely existed. The images were acquired first for medical diagnosis and not for image segmentation, which influences its processing after the segmentation. On top of that, because of the complexity of the geometry due to high curvature, the bifurcations and the coarctation, the generation of a proper mesh was tricky.

Regarding the validation, another limitation was the lack of data for the inflow boundary condition. A flow rate taken from the literature was used instead while, for the cost function, a patient's hemodynamic gradient was used. Also, the exact plane where the gradient was measured was difficult to select in COMSOL Multiphysics®. The discrepancy in sources and the misalignment of the gradient plane might lead to an increase in error. The use of patient-specific data in the entire model could be the next step in this work. The use of a mean velocity in the coarctation, instead of a vector of velocities, is one of the biggest challenges in CFD.

Finally, since this was a single patient-specific study, the methodology should be applied to more patients with different anatomical and physiological characteristics to draw more substantial conclusions. The conclusion of different simulations will help to understand if the method is reliable and compatible with different subjects.

6. Bibliography

[1]   W. H. Organization, "Cardiovascular diseases (CVDs)." [Online]. Available: https://www.who.int/en/news-room/fact-sheets/detail/cardiovascular-diseases-(cvds). [Accessed: 21-Nov-2020].

[2]   E. Wilkins, L. Wilson, K. Wickramasinghe, and P. Bhatnagar, "European Cardiovascular Disease Statistics 2017," *Eur. Hear. Netw.*, pp. 94–100, 2017.

[3]   Sistema Nacional de Saúde, "Doenças cardiovasculares." [Online]. Available: https://www.sns.gov.pt/noticias/2017/10/04/doencas-cardiovasculares/. [Accessed: 22-Nov-2020].

[4]   British Heart Foundation, "Congenital heart disease." [Online]. Available: https://www.bhf.org.uk/informationsupport/conditions/congenital-heart-disease. [Accessed: 28-Dec-2020].

[5]   H. Baumgartner *et al.*, "2020 ESC Guidelines for the management of adult congenital heart disease," *Eur. Heart J.*, pp. 1–83, 2020.

[6]   R. D. Torok, "Coarctation of the aorta: Management from infancy to adulthood," *World J. Cardiol.*, vol. 7, no. 11, p. 765, 2015.

[7]   A. Pandya, T. A. Gaziano, M. C. Weinstein, and D. Cutler, "More americans living longer with cardiovascular disease will increase costs while lowering quality of life," *Health Aff.*, vol. 32, no. 10, pp. 1706–1714, 2013.

[8]   T. Guerra and J. Tiago, "Improving Blood Flow Simulations Using Known Data," no. 1, 2014.

[9]   M. K. Mokhtar, F. Mohamed, M. N. Zamri, M. S. Sunar, and S. J. H. Chand, "A Review on Fluid Simulation Method for Blood Flow Representation," in *Medical Imaging Technology*, 2015, pp. 129–141.

[10]   J. Janela, A. Moura, and A. Sequeira, "Absorbing boundary conditions for a 3D non-Newtonian fluid-structure interaction model for blood flow in arteries," *Int. J. Eng. Sci.*, vol. 48, no. 11, pp. 1332–1349, 2010.

[11]   B. K. Lee, "Computational fluid dynamics in cardiovascular disease," *Korean Circulation Journal*, vol. 41, no. 8. Korean Circ J, pp. 423–430, Aug-2011.

[12]   C. Nassau, "CFD Simulations of Cardiovascular Devices with Shape Optimization to Reduce Blood Damage Using Genetic Algorithm," *Eng. Appl. Sci. Theses Diss.*, May 2020.

[13]   P. D. Morris *et al.*, "Computational fluid dynamics modelling in cardiovascular medicine," *Heart*, vol. 102, no. 1, pp. 18–28, 2016.

[14]   C. A. Taylor, T. J. R. Hughes, and C. K. Zarins, "Finite element modeling of blood flow in arteries," *Comput. Methods Appl. Mech. Eng.*, vol. 158, no. 1–2, pp. 155–196, 1998.

[15]   J. A. Moore, B. K. Rutt, S. J. Karlik, K. Yin, and C. R. Ethier, "Computational Blood Flow Modeling Based on In Vivo Measurements," *Ann. Biomed. Eng.*, vol. 27, no. 5, pp. 627–640, 1999.

[16]   W. M. DeCampli, I. Ricardo Argueta-Morales, E. Divo, and A. J. Kassab, "Computational fluid dynamics in congenital heart disease," in *Cardiology in the Young*, 2012, vol. 22, no. 6, pp. 800–808.

[17] J. F. Ladisa *et al.*, "Computational simulations for aortic coarctation: Representative results from a sampling of patients," *J. Biomech. Eng.*, vol. 133, no. 9, 2011.

[18] J. Lantz, T. Ebbers, J. Engvall, and M. Karlsson, "Numerical and experimental assessment of turbulent kinetic energy in an aortic coarctation," *J. Biomech.*, vol. 46, no. 11, pp. 1851–1858, Jul. 2013.

[19] A. Rinaudo *et al.*, "Computational fluid dynamics simulation to evaluate aortic coarctation gradient with contrast-enhanced CT," *Comput. Methods Biomech. Biomed. Engin.*, vol. 18, no. 10, pp. 1066–1071, Jul. 2015.

[20] J. S. Coogan, F. P. Chan, C. A. Taylor, and J. A. Feinstein, "Computational fluid dynamic simulations of aortic coarctation comparing the effects of surgical- and stent-based treatments on aortic compliance and ventricular workload," *Catheter. Cardiovasc. Interv.*, vol. 77, no. 5, pp. 680–691, Apr. 2011.

[21] S. Pasta, J. S. Cho, O. Dur, K. Pekkan, and D. A. Vorp, "Computer modeling for the prediction of thoracic aortic stent graft collapse," *J. Vasc. Surg.*, vol. 57, no. 5, pp. 1353–1361, May 2013.

[22] S. Pirola *et al.*, "On the choice of outlet boundary conditions for patient-specific analysis of aortic flow using computational fluid dynamics," *J. Biomech.*, vol. 60, pp. 15–21, 2017.

[23] H. Michael and E. Mcelroy, "Boundary Condition Assessment and Geometrical Accuracy Enhancement for Computational," 2017.

[24] F. Luca, A. Quarteroni, and A. Veneziani, *Cardiovascular Mathematics*. 2010.

[25] J. G. Betts *et al.*, *Anatomy & Physiology*. OpenStax - Rice University, 2013.

[26] K. B. Chandran, A. P. Yoganathan, S. E. Rittgers, A. P. Yoganathan, and S. E. Rittgers, *Biofluid mechanics The human circulation*, vol. 43, no. 4. 2007.

[27] L. S. Athanasiou, D. I. Fotiadis, and L. K. Michalis, "Introduction," in *Atherosclerotic Plaque Characterization Methods Based on Coronary Imaging*, 2017, pp. 1–21.

[28] M. Hoffman, "Picture of the Aorta - Human Anatomy," *WebMed*. [Online]. Available: https://www.webmd.com/heart/picture-of-the-aorta#1. [Accessed: 23-Nov-2020].

[29] D. C. Wendell *et al.*, "Including aortic valve morphology in computational fluid dynamics simulations: Initial findings and application to aortic coarctation," *Med. Eng. Phys.*, vol. 35, no. 6, pp. 723–735, Jun. 2013.

[30] L. Goubergrits *et al.*, "Is MRI-Based CFD Able to Improve Clinical Treatment of Coarctations of Aorta?," *Ann. Biomed. Eng.*, vol. 43, no. 1, pp. 168–176, 2014.

[31] K. Cao, S. K. Atkins, A. McNally, J. Liu, and P. Sucosky, "Simulations of morphotype-dependent hemodynamics in non-dilated bicuspid aortic valve aortas," *J. Biomech.*, vol. 50, pp. 63–70, 2017.

[32] O. H. Toro-Salazar, J. Steinberger, W. Thomas, A. P. Rocchini, B. Carpenter, and J. H. Moller, "Long-term follow-up of patients after coarctation of the aorta repair," *Am. J. Cardiol.*, vol. 89, no. 5, pp. 541–547, Mar. 2002.

[33] Y. C. Fung, *Biomechanics - Mechanical Properties of Living Tissues*. 2010.

[34] B. E. Rapp, "Fluids," in *Microfluidics: Modelling, Mechanics and Mathematics*, Elsevier, 2017, pp. 243–263.

[35] B. Rehm and A. Haghshenas, "Flow Drilling: Underbalance Drilling with Liquid Single-Phase Systems," in *Underbalanced Drilling: Limits and Extremes*, Elsevier Inc., 2012, pp. 39–58.

[36] W. Y. and M. D. F. David Rubenstein, *Biofluid Mechanics An Introduction to Fluid Mechanics , Macrocirculation , and Microcirculation A volume in Biomedical Engineering*, 2nd editio. 2012.

[37] A. Arzani, P. Dyverfeldt, T. Ebbers, and S. C. Shadden, "In vivo validation of numerical prediction for turbulence intensity in an aortic coarctation," *Ann. Biomed. Eng.*, vol. 40, no. 4, pp. 860–870, 2012.

[38] H.O. Fatoyinbo, "Microfluidic devices for cell manipulation," in *Microfluidic Devices for Biomedical Applications*, X. (James) Li and Y. Zhou, Eds. Woodhead, 2013, pp. 283–350.

[39] A. Ostadfar, *Biofluid Mechanics: Principles and Applications*. 2016.

[40] Y. A. Cengel, "Fluid Mechanics: Fundamentals and Application," p. 342, 2006.

[41] SimScale, "NS Explanation." [Online]. Available: https://www.simscale.com/docs/content/simwiki/numerics/what-are-the-navier-stokes-equations.html.

[42] M. H. of Mathematics, "Claude-Louis Navier (1785 - 1836) - Biography." [Online]. Available: https://mathshistory.st-andrews.ac.uk/Biographies/Navier/. [Accessed: 15-Dec-2020].

[43] M. H. of Mathematics, "George Stokes (1819 - 1903) - Biography." [Online]. Available: https://mathshistory.st-andrews.ac.uk/Biographies/Stokes/. [Accessed: 15-Dec-2020].

[44] A. Quarteroni, *Numerical Models for Differential Problems*, vol. 2. 2009.

[45] Clay Mathematics Institute, "Navier–Stokes Equation." [Online]. Available: https://www.claymath.org/millennium-problems/navier–stokes-equation. [Accessed: 15-Dec-2020].

[46] Weierstrass Institute for Applied Analysis and Stochastics, "The Navier-Stokes Equations."

[47] COMSOL, "Introduction to the Optimization Module," pp. 1–69.

[48] J. Pfitzner, "Poiseuille and his law," *Anaesthesia*, vol. 31, no. 2, pp. 273–275, 1976.

[49] S. P. Sutera and R. Skalak, "The History of Poiseuille's Law," *Annu. Rev. Fluid Mech.*, vol. 25, no. 1, pp. 1–20, Jan. 1993.

[50] Y. Ma, Z. He, X. Peng, and Z. Xing, *Fundamentals of Heat and Mass*, vol. 32, no. 1. 2012.

[51] L. Waite and J. Fine, *Applied Biofluid Mechanics*. McGraw-Hill, 2007.

[52] T. F. Sherman, "On Connecting Large Vessels to Small - The Meaning of Murray's Law," *J. Gen. Physiol.*, 1981.

[53] P. R. Painter, P. Edén, and H. Bengtsson, "Pulsatile blood flow, shear force, energy dissipation and Murray's Law," *Theor. Biol. Med. Model.*, vol. 10, 2006.

[54] D. Stephenson, A. Patronis, D. M. Holland, and D. A. Lockerby, "Generalizing Murray's law: An optimization principle for fluidic networks of arbitrary shape and scale," *J. Appl. Phys.*, vol. 174302, no. October, 2015.

[55] R. M. Romarowski, A. Lefieux, S. Morganti, A. Veneziani, and F. Auricchio, "Patient-specific CFD modelling in the thoracic aorta with PC-MRI-based boundary conditions: A least-square three-element Windkessel approach," *Int. j. numer. method. biomed. eng.*, vol. 34, no. 11, p. e3134, Nov. 2018.

[56]　L. Formaggia and C. Vergara, "Prescription of General Defective Boundary Conditions in Fluid-Dynamics," *Milan J. Math.*, vol. 80, no. 2, pp. 333–350, 2012.

[57]　B. Liu, J. Zheng, R. Bach, and D. Tang, "Influence of model boundary conditions on blood flow patterns in a patient specific stenotic right coronary artery," *Biomed. Eng. Online*, vol. 14, no. Suppl 1, p. S6, 2015.

[58]　E. Soudah, E. Y. K. Ng, T. H. Loong, M. Bordone, U. Pua, and S. Narayanan, "CFD modelling of abdominal aortic aneurysm on hemodynamic loads using a realistic geometry with CT," *Comput. Math. Methods Med.*, vol. 2013, 2013.

[59]　P. Vasava, P. Jalali, M. Dabagh, and P. J. Kolari, "Finite Element Modelling of Pulsatile Blood Flow in Idealized Model of Human Aortic Arch: Study of Hypotension and Hypertension," *Comput. Math. Methods Med.*, vol. 2012, pp. 1–14, 2012.

[60]　P. Crosetto, P. Reymond, S. Deparis, D. Kontaxakis, N. Stergiopulos, and A. Quarteroni, "Fluid-structure interaction simulation of aortic blood flow," *Comput. Fluids*, vol. 43, no. 1, pp. 46–57, 2011.

[61]　J. Alastruey, J. H. Siggers, V. Peiffer, D. J. Doorly, and S. J. Sherwin, "Reducing the data: Analysis of the role of vascular geometry on blood flow patterns in curved vessels," *Phys. Fluids*, vol. 24, no. 3, p. 031902, Mar. 2012.

[62]　"Computational viscoelastic fluid dynamics," in *Rheology Series*, vol. 6, no. C, Elsevier, 1997, pp. 397–472.

[63]　S. Madhavan and E. M. C. Kemmerling, "The effect of inlet and outlet boundary conditions in image-based CFD modeling of aortic flow," *Biomed. Eng. Online*, vol. 17, no. 1, pp. 1–20, 2018.

[64]　D. Gallo *et al.*, "On the use of in vivo measured flow rates as boundary conditions for image-based hemodynamic models of the human aorta: Implications for indicators of abnormal flow," *Ann. Biomed. Eng.*, vol. 40, no. 3, pp. 729–741, 2012.

[65]　I. C. Campbell, J. Ries, S. S. Dhawan, A. A. Quyyumi, W. R. Taylor, and J. N. Oshinski, "Effect of inlet velocity profiles on patient-specific computational fluid dynamics simulations of the carotid bifurcation," *J. Biomech. Eng.*, vol. 134, no. 5, pp. 1–8, 2012.

[66]　U. Morbiducci *et al.*, "Outflow conditions for image-based hemodynamic models of the carotid bifurcation: Implications for indicators of abnormal flow," *J. Biomech. Eng.*, vol. 132, no. 9, pp. 1–11, 2010.

[67]　P. E. Vincent, A. M. Plata, A. A. E. Hunt, P. D. Weinberg, and S. J. Sherwin, "Blood flow in the rabbit aortic arch and descending thoracic aorta," *J. R. Soc. Interface*, vol. 8, no. 65, pp. 1708–1719, 2011.

[68]　N. Shahcheranhi, H. A. Dwyer, A. Y. Cheer, A. I. Barakat, and T. Rutaganira, "Unsteady and three-dimensional simulation of blood flow in the human aortic arch," *J. Biomech. Eng.*, vol. 124, no. 4, pp. 378–387, 2002.

[69]　G. Shuang, "Computational Fluid Dynamics for Coronary Diseases: Analysis of Different Murray's Law Based Boundary Conditions," *J. Res. Midwifery Politek. Tegal*, 2017.

[70]　M. McElroy and A. Keshmiri, "Impact of Using Conventional Inlet/Outlet Boundary Conditions

on Haemodynamic Metrics in a Subject-Specific Rabbit Aorta," *Proc. Inst. Mech. Eng. Part H J. Eng. Med.*, vol. 232, no. 2, pp. 103–113, Feb. 2018.

[71] U. Morbiducci *et al.*, "Outflow conditions for image-based hemodynamic models of the carotid bifurcation: Implications for indicators of abnormal flow," *J. Biomech. Eng.*, vol. 132, no. 9, Sep. 2010.

[72] M. Alimohammadi, O. Agu, S. Balabani, and V. Díaz-Zuccarini, "Development of a patient-specific simulation tool to analyse aortic dissections: Assessment of mixed patient-specific flow and pressure boundary conditions," *Med. Eng. Phys.*, vol. 36, no. 3, pp. 275–284, 2014.

[73] S. Madhavan and E. M. C. Kemmerling, "The effect of inlet and outlet boundary conditions in image-based CFD modeling of aortic flow," *Biomed. Eng. Online*, vol. 17, no. 1, p. 66, May 2018.

[74] T. Guerra, A. Sequeira, and J. Tiago, "Existence of optimal boundary control for the navier-stokes equations with mixed boundary conditions," *Port. Math.*, vol. 72, no. 2–3, pp. 267–283, 2015.

[75] M. D'Elia, M. Perego, and A. Veneziani, "A variational data assimilation procedure for the incompressible Navier-Stokes equations in hemodynamics," *J. Sci. Comput.*, vol. 52, no. 2, pp. 340–359, 2012.

[76] A. Sequeira, V. Volpert, J. Tiago, A. Gambaruto, and A. Sequeira, "Patient-specific blood flow simulations: Setting Dirichlet boundary conditions for minimal error with respect to measured data," *Math. Model. Nat. Phenom.*, vol. 9, no. 6, pp. 98–116, 2014.

[77] J. Tiago, T. Guerra, and A. Sequeira, "A velocity tracking approach for the data assimilation problem in blood flow simulations," *Int. j. numer. method. biomed. eng.*, vol. 33, no. 10, pp. 1–17, 2017.

[78] P. Moireau *et al.*, "Sequential identification of boundary support parameters in a fluid-structure vascular model using patient image data," *Biomech. Model. Mechanobiol.*, vol. 12, no. 3, pp. 475–496, 2013.

[79] K. Ghobadi, N. S. Nedialkov, and T. Terlaky, "On the Discretize then Optimize Approach," *Ind. Syst. Eng.*

[80] J. Nocedal and S. J. Wright, *Numerical Optimization*, 2nd Editio. 2006.

[81] Indian Institute of Technology Madras - Department of Mechanical Engineering, "Optimization Methods."

[82] P. E. Gill, W. Murray, and M. A. Saunders, "User's Guide for SNOPT Version 7: Software for Large-Scale Nonlinear Programming," 2008.

[83] P. E. Gill, W. Murray, and M. A. Saunders, "SNOPT: An SQP algorithm for large-scale constrained optimization," *SIAM Rev.*, vol. 47, no. 1, pp. 99–131, 2005.

[84] L. Barreto, "Computational analysis of aortic hemodynamics - comparison of outflow modelling strategies," Universidade de Lisboa - Instituto Superior Técnico, 2019.

[85] H. X. U. Uijuan, M. A. P. Iccinelli, B. R. G. L. Eshnower, A. D. L. Efieux, W. R. O. T. Aylor, and A. L. V Eneziani, "Coupled Morphological – Hemodynamic Computational Analysis of Type B Aortic Dissection : A Longitudinal Study," *Ann. Biomed. Eng.*, vol. 46, no. 7, pp. 927–939,

2018.

[86]   C. H. Armour *et al.*, "The influence of inlet velocity profile on predicted flow in type B aortic dissection," *Biomech. Model. Mechanobiol.*, pp. 1–10, Oct. 2020.

[87]   P. Reymond, P. Crosetto, S. Deparis, A. Quarteroni, and N. Stergiopulos, "Physiological simulation of blood flow in the aorta: Comparison of hemodynamic indices as predicted by 3-D FSI, 3-D rigid wall and 1-D models," *Med. Eng. Phys.*, vol. 35, no. 6, pp. 784–791, 2013.

[88]   K. Ming, P. Chiu, H. Pueh, and P. Ho, "Investigation of hemodynamics in the development of dissecting aneurysm within patient-specific dissecting aneurismal aortas using computational fluid dynamics (CFD) simulations," *J. Biomech.*, vol. 44, no. 5, pp. 827–836, 2011.

[89]   C. Celestin, M. Guillot, N. Ross-Ascuitto, and R. Ascuitto, "Computational Fluid Dynamics Characterization of Blood Flow in Central Aorta to Pulmonary Artery Connections: Importance of Shunt Angulation as a Determinant of Shear Stress-Induced Thrombosis," *Pediatr. Cardiol.*, vol. 36, no. 3, pp. 600–615, Feb. 2015.

[90]   D. Oliveira, S. A. Rosa, J. Tiago, R. C. Ferreira, F. Agapito, and A. Sequeira, "Bicuspid aortic valve aortopathies : An hemodynamics characterization in dilated aortas," *Comput. Methods Biomech. Biomed. Engin.*, vol. 22, no. 8, pp. 815–826, 2019.

[91]   G. Y. Suh *et al.*, "Hemodynamic changes quantified in abdominal aortic aneurysms with increasing exercise intensity using MR exercise imaging and image-based computational fluid dynamics," *Ann. Biomed. Eng.*, vol. 39, no. 8, pp. 2186–2202, 2011.

[92]   J. Svensson *et al.*, "Feasibility of patient specific aortic blood flow CFD simulation," in *International Conference on Medical Image Computing and Computer-Assisted Intervention*, 2006, vol. 4190 LNCS, pp. 257–263.

[93]   M. S. Rahman and M. A. Haque, "Mathematical modeling of blood flow," *2012 Int. Conf. Informatics, Electron. Vision, ICIEV 2012*, no. May, pp. 672–676, 2012.

[94]   C. D. Murray, "The physiological principle of minimum work applied to the angle branching of arteries," 1926.

[95]   G. P. Nikishkov, "Introduction to the finite element method," 2004.

[96]   D. W. Pepper and J. C. Heinrich, "The Finite Element Method Basic Concepts and Applications with MATLAB, MAPLE, and COMSOL." p. 628, 2017.

[97]   Z. Li, Z. Qiao, and T. Tang, "Finite Element Methods for 1D Boundary Value Problems," *Numer. Solut. Differ. Equations*, vol. 1, pp. 135–157, 2017.

[98]   M. Asadzadeh, "An Introduction to the Finite Element Method (FEM) for Differential Equations in 1D," 2015.

[99]   COMSOL Multiphysics, "Introduction To Comsol Multiphysics," 2014.

[100]   COMSOL Multiphysics, "Optimization Module User's Guide," 1998.

[101]   A. Harish, "How to Choose a Solver for FEM Problems: Direct or Iterative?," *Simscale Blog*. [Online]. Available: https://www.simscale.com/blog/2016/08/how-to-choose-solvers-for-fem/. [Accessed: 17-Nov-2020].

[102]   PARDISO, "User Guide Version 6.0.0."

[103]   COMSOL Multiphysics, "Choosing the Right Linear System Solver." [Online]. Available:

https://doc.comsol.com/5.5/doc/com.comsol.help.comsol/comsol_ref_solver.27.118.html. [Accessed: 17-Nov-2020].

[104] National Institute of Biomedical Imaging and Bioengineering, "Computed Tomography (CT)." [Online]. Available: https://www.nibib.nih.gov/science-education/science-topics/computed-tomography-ct. [Accessed: 11-Dec-2020].

[105] National Library of Medicine - Nacional Center for Biotechnology Information, "Iopromide | C18H24I3N3O8 - PubChem." [Online]. Available: https://pubchem.ncbi.nlm.nih.gov/compound/Iopromide. [Accessed: 11-Dec-2020].

[106] DrugBank Online, "Iopromide." [Online]. Available: https://go.drugbank.com/drugs/DB09156. [Accessed: 02-Nov-2020].

[107] Y. Tan, *GPU-Based Parallel Implementation of Swarm Intelligence Algorithms.* Elsevier Inc., 2016.

[108] Y. Guo and Amira S. Ashour, *Neutrosophic Set in Medical Image Analysis*. Elsevier, 2019.

[109] N. Sharma *et al.*, "Automated medical image segmentation techniques," *Journal of Medical Physics*, vol. 35, no. 1. Wolters Kluwer -- Medknow Publications, pp. 3–14, 01-Jan-2010.

[110] DICOM, "Introduction and Overview," 2020.

[111] K. T. Bae, "Intravenous contrast medium administration and scan timing at CT: Considerations and approaches," *Radiology*, vol. 256, no. 1, pp. 32–61, Jul. 2010.

[112] University of Edinburgh - School of Informatics, "Spatial Filters - Gaussian Smoothing." [Online]. Available: https://homepages.inf.ed.ac.uk/rbf/HIPR2/gsmooth.htm. [Accessed: 11-Dec-2020].

[113] Gabriel Taubin, "Curve and surface smoothing without shrinkage," *IEEE Int. Conf. Comput. Vis.*, pp. 852–857, 1995.

[114] "Autoconverter Software." .

[115] J. Brüning, F. Hellmeier, P. Yevtushenko, T. Kühne, and L. Goubergrits, "Uncertainty Quantification for Non-invasive Assessment of Pressure Drop Across a Coarctation of the Aorta Using CFD," *Cardiovasc. Eng. Technol.*, vol. 9, no. 4, pp. 582–596, 2018.

[116] Princeton, "Streamlines and Streamtubes." [Online]. Available: https://www.princeton.edu/~asmits/Bicycle_web/streamline.html. [Accessed: 29-Nov-2020].

[117] ScienceDirect, "Aortic Flow - an overview." [Online]. Available: https://www.sciencedirect.com/topics/medicine-and-dentistry/aortic-flow. [Accessed: 20-Dec-2020].

[118] M. Seear, S. Webber, and J. Leblanc, "Pediatric Cardiology Descending Aortic Blood Flow Velocity as a Noninvasive Measure of Cardiac Output in Children," 1994.

[119] MacTutor History of Mathematics, "Osborne Reynolds (1842 - 1912) - Biography." [Online]. Available: https://mathshistory.st-andrews.ac.uk/Biographies/Reynolds/. [Accessed: 15-Dec-2020].

[120] S. Karmakar, "Equations Governing Hydrologic and Hydraulic Routing."

[121] The Cambridge - MIT Institute, "System and Control Volume." [Online]. Available: http://www-mdp.eng.cam.ac.uk/web/library/enginfo/aerothermal_dvd_only/aero/fprops/cvanalysis/node10.

html. [Accessed: 23-Nov-2020].

[122] G. Dairbayeva, "The Cauchy problem for the Stokes equations," *J. Math. Mech. Comput. Sci.*, vol. 95, no. 3, pp. 78–89, 2017.

Annexes

Annexe A: Navier-Stokes equations

Reynold's Transport Theorem

The Reynold's Transport Theorem (RTT) formulation, named after Osborne Reynolds (1842 − 1912), an Irish mathematician and physicist [119], is the relationship that relates the time rate of change of an extensive property (N) as a function of the intensive property (η). While the extensive property is a property that depends on the mass contained in a fluid, the intensive property corresponds to the same property per unit mass of volume and therefore does not depend on the mass. [36], [120]

The RTT is used to compute the derivatives of integrated quantities, which is needed to derivate the basic conservation laws of fluid mechanics. In this study, the RTT will be used to derivate the Navier-Stokes equations from the mass, linear momentum, and energy conservation laws. These conservation laws are adopted from classical mechanics and classic thermodynamics where the system approach is usually applied. The system approach refers to a fixed mass within a boundary where the mass remains constant with time, even if the system's boundary changes [121]. On the other hand, in fluid mechanics, the control volume approach is usually chosen because it is challenging to recognize and keep track of a system of fluid particles. In the control volume approach, a fixed volume enclosed by a control surface is either standing still in space or moving with a constant velocity through which the fluid flows. Therefore, the RTT will be used to link the system equations and the corresponding control volume equations. [36], [120]

The RTT states that the total rate of change of an extensive property of a system occupying a control volume (Ω) at time t is equal to the sum of the 1) temporal rate of change of N within the control volume and 2) the net flux of the property N through the control surface ($\partial\Omega$) that surrounds the control volume. It is expressed in terms of a substantive derivative on the left-hand side:

$$\frac{DN}{Dt} = \int_{\Omega} \frac{\partial}{\partial t}(\rho\eta)dV + \int_{\partial\Omega} \rho\eta\overrightarrow{v_b} \cdot \hat{n}\,dA + \int_{\partial\Omega} \rho\eta\overrightarrow{v_r} \cdot \hat{n}\,dA \tag{76}$$

Here ρ is the fluid density, V is the volume, v_b is the velocity of the control surface, v_r is the velocity of the fluid in the control surface, n is the outward pointing normal vector on the control surface, and A is the area of the $\partial\Omega$. [36], [120]

From the relationship defined by the RTT, all conservation laws can be derived by substituting the appropriate extensive and intensive properties.

Navier-Stokes equations

As seen in Section 2.2.2.1, the NS equations correspond to the continuity equation and the conservation of linear momentum, which will be derived in the following two sections.

- Continuity Equation for Conservation of Mass

To derive the continuity equation for the conservation of mass, Reynolds's Transport Theorem is applied. Substituting the extensive property (N) by the mass, the intensive property by $\eta = 1$ and the right-side to zero due to the conservation of mass, the following general expression for conservation of mass applied to a control volume is obtained:

$$0 = \int\limits_{CV} \frac{\partial \rho}{\partial t} dV + \int\limits_{CS} \rho \vec{V} \cdot \vec{n} \, dA \tag{77}$$

If there are well-defined inlets and outlets, the net rate of change of mass within the control volume is equal to the rate at which mass flows into the control volume minus the rate at which mass flows out of the control volume, which is written as:

$$\int\limits_{CV} \frac{\partial \rho}{\partial t} dV = \sum_{in} \dot{m} - \sum_{out} \dot{m} \tag{78}$$

Considering the control volume as an infinitesimal cubed control volume, with dimensions dx, dy and dz and volume $V = dx\, dy\, dz$, aligned with the axes in Cartesian coordinates. The centre of the cube is revealed at some arbitrary point P from the origin, and its density and velocity components are ρ, u, v, and w, respectively. To generate a differential equation for conservation of mass, the control volume is considered to diminish to infinitesimal size, shrinking in the limit to a point in the flow.

At locations distant from the centre of the cube, a Taylor series expansion is used about the centre of the cube (point P) to define mass flow rate ($\dot{m}$). As the cube representing the control volume shrinks to a point, second-order and higher terms of the expansion become negligible. For example, the centre of the right-most face of the cube is located a distance $dx/2$ from the middle of the cube in the x-direction; the value of ρu at that point is:

$$(\rho u)_{centre\,of\,right\,face} = \rho u + \frac{\partial(\rho u)}{\partial x}\frac{dx}{2} + \frac{1}{2!}\frac{\partial^2(\rho u)}{\partial x^2}\left(\frac{dx}{2}\right)^2 + \ldots \cong \rho u + \frac{\partial(\rho u)}{\partial x}\frac{dx}{2} \tag{79}$$

Applying this truncated Taylor series expansion to the density times the normal velocity component at the centre point of each of the six faces of the cube, it becomes:

$$(\rho u)_{centre\,of\,right\,face} \cong \rho u + \frac{\partial(\rho u)}{\partial x}\frac{dx}{2} \tag{80}$$

$$(\rho u)_{centre\,of\,left\,face} \cong \rho u - \frac{\partial(\rho u)}{\partial x}\frac{dx}{2} \tag{81}$$

$$(\rho v)_{centre\,of\,top\,face} \cong \rho v + \frac{\partial(\rho v)}{\partial y}\frac{dy}{2} \tag{82}$$

$$(\rho v)_{centre\,of\,bottom\,face} \cong \rho v - \frac{\partial(\rho v)}{\partial y}\frac{dy}{2} \tag{83}$$

$$(\rho w)_{centre\,of\,front\,face} \cong \rho w + \frac{\partial(\rho w)}{\partial z}\frac{dz}{2} \tag{84}$$

$$(\rho w)_{centre\,of\,back\,face} \cong \rho w - \frac{\partial(\rho w)}{\partial z}\frac{dz}{2} \tag{85}$$

The mass flow rate into or out of one of the faces is equal to the density times the normal velocity component at the centre point of the face times the surface area of the face

$$\dot{m} = \rho V_n A \tag{86}$$

Where V_n is the magnitude of the normal velocity through the face and A is the surface area of the face. As the control volume shrinks to an infinitesimal point, the rate of change of mass within the control volume becomes:

$$\int_{\Omega} \frac{\partial \rho}{\partial t} dV \cong \frac{\partial \rho}{\partial t} dx\, dy\, dz \tag{87}$$

Applying the normal velocity components in each face, given above, and adding up all the mass flow rates into (left, back and bottom faces) and out (right, front and top faces) of the control volume through the faces, the net mass flow rate into CV becomes:

$$\sum_{in} \dot{m} \cong \left(\rho u - \frac{\partial(\rho u)}{\partial x} \frac{dx}{2} \right) dy\, dz + \left(\rho v - \frac{\partial(\rho v)}{\partial y} \frac{dy}{2} \right) dx\, dz + \left(\rho w - \frac{\partial(\rho w)}{\partial z} \frac{dz}{2} \right) dx\, dy \tag{88}$$

And the net mass flow rate out of CV:

$$\sum_{out} \dot{m} \cong \left(\rho u + \frac{\partial(\rho u)}{\partial x} \frac{dx}{2} \right) dy\, dz + \left(\rho v + \frac{\partial(\rho v)}{\partial y} \frac{dy}{2} \right) dx\, dz + \left(\rho w + \frac{\partial(\rho w)}{\partial z} \frac{dz}{2} \right) dx\, dy \tag{89}$$

Inserting these two terms into the equation (78), and considering all the needed combinations and simplifications, the Continuity Equation in Cartesian Coordinates is given by:

$$\frac{\partial \rho}{\partial t} dx\, dy\, dz = -\frac{\partial(\rho u)}{\partial x} dx\, dy\, dz - \frac{\partial(\rho v)}{\partial y} dx\, dy\, dz - \frac{\partial(\rho w)}{\partial z} dx\, dy\, dz$$

$$\frac{\partial \rho}{\partial t} + \frac{\partial(\rho u)}{\partial x} + \frac{\partial(\rho v)}{\partial y} + \frac{\partial(\rho w)}{\partial z} = 0 \tag{90}$$

When the fluid is incompressible, the density is constant:

$$\frac{\partial u}{\partial x} + \frac{\partial v}{\partial y} + \frac{\partial w}{\partial z} = 0 \tag{91}$$

- Conservation of Linear Momentum

To derive Cauchy's equation, once again, the Reynolds Transport Theorem is again the starting point. Considering the extensive parameter (N) as linear momentum, velocity (v) as the intensive parameter (η), σ_{ij} as the stress tensor and well-defined inlets and outlets.

$$\sum \vec{F} = \int_{CV} \rho \vec{g}\, dV + \int_{CS} \sigma_{ij} \cdot \vec{n}\, dA = \int_{CV} \frac{\partial}{\partial t} \left(\rho \vec{V} \right) dV + \int_{CS} \left(\rho \vec{V} \right) \vec{V} \cdot \vec{n}\, dA \tag{92}$$

$$\sum \vec{F} = \sum \vec{F}_{body} + \sum \vec{F}_{surface} = \int_{CV} \frac{\partial}{\partial t} \left(\rho \vec{V} \right) dV + \sum_{out} \beta \dot{m} \vec{V} - \sum_{in} \beta \dot{m} \vec{V} \tag{93}$$

Where $\vec{V}$ in the last two terms is taken as the average velocity at an inlet or outlet, and β is the momentum flux correction factor. From Newton's second law, the total force acting on the control volume is equal to the rate at which momentum changes within the control volume plus the rate at which momentum flows out of the control volume minus the rate at which momentum flows into the control volume.

Considering, once more, the control volume as an infinitesimal cube-shaped control volume, with dimensions dx, dy and dz and volume $V = dx\, dy\, dz$, aligned with the axes in Cartesian coordinates. The centre of the cube is revealed at some arbitrary point P from the origin and where the density (ρ), velocity components (u, v and w) and stress tensor (σ_{ij}) are defined. To generate a differential equation for conservation of linear momentum, one imagines the control volume shrinking to infinitesimal size and the limit to a point in the flow.

Considering the x-component of the equation (93), for simplicity, and u as the x-direction of $\vec{V}$, the total forces in the system become:

$$\sum \vec{F}_x = \sum \vec{F}_{x,body} + \sum \vec{F}_{x,surface} = \int_{CV} \frac{\partial}{\partial t}(\rho u)\, dV + \sum_{out} \beta \dot{m} u - \sum_{in} \beta \dot{m} u \tag{94}$$

As the control volume shrinks to a point, the first term of the right-hand side becomes:

$$\int_{CV} \frac{\partial}{\partial t}(\rho u)\, dV \cong \frac{\partial}{\partial t}(\rho u)\, dx\, dy\, dz \tag{95}$$

Which is the rate of change of x-momentum within the control volume. To obtain the remaining two terms of the right-hand side of the equation (94), first, a first-order truncated Taylor series expansions is applied at locations away from the centre of the cube control volume to approximate the inflow and outflow of momentum in the x-direction obtaining for the six faces:

$$(\rho uu)_{centre\,of\,right\,face} \cong \rho uu + \frac{\partial(\rho uu)}{\partial x}\frac{dx}{2} \tag{96}$$

$$(\rho uu)_{centre\,of\,left\,face} \cong \rho uu - \frac{\partial(\rho uu)}{\partial x}\frac{dx}{2} \tag{97}$$

$$(\rho vu)_{centre\,of\,top\,face} \cong \rho vu + \frac{\partial(\rho vu)}{\partial y}\frac{dy}{2} \tag{98}$$

$$(\rho vu)_{centre\,of\,bottom\,face} \cong \rho vu - \frac{\partial(\rho vu)}{\partial y}\frac{dy}{2} \tag{99}$$

$$(\rho wu)_{centre\,of\,front\,face} \cong \rho wu + \frac{\partial(\rho wu)}{\partial z}\frac{dz}{2} \tag{100}$$

$$(\rho wu)_{centre\,of\,back\,face} \cong \rho wu - \frac{\partial(\rho wu)}{\partial z}\frac{dz}{2} \tag{101}$$

Only the normal velocity component at each face needs to be considered, since the tangential velocity components contribute no mass flow out of (or into) the face, and hence no momentum flow through the face either.

Secondly, summing all outflows and subtracting the all the inflows one obtains and considering β equal in all faces, one has:

$$\sum_{out} \beta \dot{m} u - \sum_{in} \beta \dot{m} u \cong \left(\frac{\partial}{\partial x}(\rho uu) + \frac{\partial}{\partial y}(\rho vu) + \frac{\partial}{\partial z}(\rho wu) \right) dx\, dy\, dz \tag{102}$$

The equation (102) represents the net outflow of x-momentum through the control surface.

To derive the left-hand side of the equation (94), all the forces – body and surface - acting on our infinitesimal control volume in the x-direction need to be summed. The gravity force (weight) is the only body force to be considered, and since the control volume is aligned with the axes, for the x-direction, the body forces become:

$$\sum \vec{F}_{x,body} = \sum \vec{F}_{x,gravity} \cong \rho g_x\, dx\, dy\, dz \tag{103}$$

For the surface forces, each stress component (σ_{ij}) is multiplied by the surface area of the face on which it acts. For the x-direction, the components that point in the x- (or -x-) direction are only

considered. Using truncated Taylor series expansions, all the surface forces contributing to a net x-component of surface force acting can be obtained for the differential fluid element.

Summing all these surface forces, the approximation for the net surface force acting on the differential fluid element in the x-direction is obtained:

$$\sum \vec{F}_{x,surface} \cong \left(\frac{\partial}{\partial x} \sigma_{xx} + \frac{\partial}{\partial y} \sigma_{yx} + \frac{\partial}{\partial z} \sigma_{zx} \right) dx\, dy\, dz \tag{104}$$

Finally, substituting equations (95) and (102) to (104) into equation (94), and eliminating $dx\, dy\, dz$, for the x-direction:

$$\rho g_x + \frac{\partial}{\partial x} \sigma_{xx} + \frac{\partial}{\partial y} \sigma_{yx} + \frac{\partial}{\partial z} \sigma_{zx} = \frac{\partial}{\partial t}(\rho u) + \frac{\partial}{\partial x}(\rho u u) + \frac{\partial}{\partial y}(\rho v u) + \frac{\partial}{\partial z}(\rho w u) \tag{105}$$

Similarly, one can obtain the same equations for the y- and z-directions:

$$\rho g_y + \frac{\partial}{\partial x} \sigma_{xy} + \frac{\partial}{\partial y} \sigma_{yy} + \frac{\partial}{\partial z} \sigma_{zy} = \frac{\partial}{\partial t}(\rho v) + \frac{\partial}{\partial x}(\rho u v) + \frac{\partial}{\partial y}(\rho v v) + \frac{\partial}{\partial z}(\rho w v) \tag{106}$$

$$\rho g_z + \frac{\partial}{\partial x} \sigma_{xz} + \frac{\partial}{\partial y} \sigma_{yz} + \frac{\partial}{\partial z} \sigma_{zz} = \frac{\partial}{\partial t}(\rho w) + \frac{\partial}{\partial x}(\rho u w) + \frac{\partial}{\partial y}(\rho v w) + \frac{\partial}{\partial z}(\rho w w) \tag{107}$$

And obtain the vector equation for the Cauchy's equation:

$$\rho \vec{g} + \vec{\nabla} \cdot \sigma ij = \frac{\partial}{\partial t}(\rho \vec{V}) + \vec{\nabla} \cdot \left(\rho \vec{V}\vec{V} \right) \tag{108}$$

Which can also be written as:

$$\rho \left[\frac{\partial \vec{V}}{\partial t} + \left(\vec{V} \cdot \vec{\nabla} \right) \vec{V} \right] = \rho \frac{D\vec{V}}{Dt} = \rho \vec{g} + \vec{\nabla} \cdot \sigma ij \tag{109}$$

Since

$$\frac{\partial}{\partial t}\left(\rho \vec{V} \right) = \rho \frac{\partial \vec{V}}{\partial t} + \vec{V} \frac{\partial \rho}{\partial t} \tag{110}$$

$$\vec{\nabla} \cdot \left(\rho \vec{V}\vec{V} \right) = \vec{V}\vec{V} \cdot \left(\rho \vec{V} \right) + \rho \left(\vec{V} \cdot \vec{\nabla} \right) \vec{V} \tag{111}$$

Fluid mechanics problems cannot be solved by using Cauchy's equation by itself, even when combined with the Continuity Equation, since the stress tensor σ_{ij} needs to be expressed in terms of the primary unknowns in the problem: density, pressure, and velocity. [122]

The stress tensor σ_{ij} contains nine components, six of which are independent because of symmetry. Thus, in addition to density and the three velocity components, there are six additional unknowns, for a total of 10 unknowns ($\rho,\ u,\ v,\ w,\ \sigma_{xx},\ \sigma_{xy},\ \sigma_{xz},\ \sigma_{yy}, \sigma_{yz}$ and σ_{zz}).

The Continuity Equation returns one equation while the Cauchy equations return three equations. Since the number of equations needs to be the number of unknowns, six more equations are missing. These additional equations are called constitutive equations and enable writing the stress tensor components in terms of the velocity field and pressure field.

To obtain these constitutive equations, the pressure stresses and the viscous stresses are separated. When a fluid is at rest, the only stress acting at any surface of any fluid element is the local hydrostatic pressure P, which always acts inward and normal to the surface. Therefore, the stress tensor reduces to:

$$\sigma_{ij} = \begin{bmatrix} \sigma_{xx} & \sigma_{xy} & \sigma_{xz} \\ \sigma_{yx} & \sigma_{yy} & \sigma_{yz} \\ \sigma_{zx} & \sigma_{zy} & \sigma_{zz} \end{bmatrix} = \begin{bmatrix} -P & 0 & 0 \\ 0 & -P & 0 \\ 0 & 0 & -P \end{bmatrix} \tag{112}$$

When a fluid is moving, pressure still acts inwardly normal, but viscous stresses may also exist. Therefore, the system can be written as:

$$\sigma_{ij} = \begin{bmatrix} \sigma_{xx} & \sigma_{xy} & \sigma_{xz} \\ \sigma_{yx} & \sigma_{yy} & \sigma_{yz} \\ \sigma_{zx} & \sigma_{zy} & \sigma_{zz} \end{bmatrix} = \begin{bmatrix} -P & 0 & 0 \\ 0 & -P & 0 \\ 0 & 0 & -P \end{bmatrix} + \begin{bmatrix} \tau_{xx} & \tau_{xx} & \tau_{xx} \\ \tau_{yx} & \tau_{yy} & \tau_{yz} \\ \tau_{zx} & \tau_{zy} & \tau_{zz} \end{bmatrix} \tag{113}$$

τ_{ij} is the viscous stress tensor, which can be expressed using constitutive equations in terms of velocity field and measurable fluid properties like viscosity.

If the fluid is incompressible, the equation of state is replaced by the equation $\rho =$ constant, and P cannot be defined as the thermodynamic pressure anymore. Instead, P_m is defined as the mechanical pressure, which is the mean normal stress acting inwardly on a fluid element.

$$P_m = \frac{1}{3}\left(\sigma_{xx} + \sigma_{yy} + \sigma_{zz} \right) \tag{114}$$

Thus, when dealing with incompressible fluid flows, pressure variable P is always interpreted as the mechanical pressure P_m. For compressible flow fields, however, pressure P is the thermodynamic pressure, but the mean normal stress felt on the surfaces of a fluid element is not necessarily the same as P (pressure variable P and mechanical pressure P_m are not necessarily equivalent).

Considering the fluid a Newtonian, therefore the stress tensor is linearly proportional to the strain rate tensor. Additionally, if the fluid isothermal (local temperature changes are small or non-existent) allows assuming properties such as dynamic viscosity μ and kinematic viscosity ν are constant, therefore:

$$\tau_{ij} = 2\mu\varepsilon_{ij} \tag{115}$$

where ε_{ij} is the strain rate tensor.

In Cartesian coordinates, the nine components of the viscous stress tensor are listed, six of which are independent due to symmetry:

$$\tau_{ij} = \begin{bmatrix} \tau_{xx} & \tau_{xx} & \tau_{xx} \\ \tau_{yx} & \tau_{yy} & \tau_{yz} \\ \tau_{zx} & \tau_{zy} & \tau_{zz} \end{bmatrix} = \begin{bmatrix} 2\mu\frac{\partial u}{\partial x} & \mu\left(\frac{\partial u}{\partial y}+\frac{\partial v}{\partial x}\right) & \mu\left(\frac{\partial u}{\partial z}+\frac{\partial w}{\partial x}\right) \\ \mu\left(\frac{\partial v}{\partial x}+\frac{\partial u}{\partial y}\right) & 2\mu\frac{\partial v}{\partial y} & \mu\left(\frac{\partial v}{\partial z}+\frac{\partial w}{\partial y}\right) \\ \mu\left(\frac{\partial w}{\partial x}+\frac{\partial u}{\partial z}\right) & \mu\left(\frac{\partial w}{\partial y}+\frac{\partial v}{\partial z}\right) & 2\mu\frac{\partial w}{\partial z} \end{bmatrix} \tag{116}$$

For the same type of coordinates, the stress tensor becomes:

$$\sigma_{ij} = \begin{bmatrix} -P & 0 & 0 \\ 0 & -P & 0 \\ 0 & 0 & -P \end{bmatrix} + \begin{bmatrix} 2\mu\frac{\partial u}{\partial x} & \mu\left(\frac{\partial u}{\partial y}+\frac{\partial v}{\partial x}\right) & \mu\left(\frac{\partial u}{\partial z}+\frac{\partial w}{\partial x}\right) \\ \mu\left(\frac{\partial v}{\partial x}+\frac{\partial u}{\partial y}\right) & 2\mu\frac{\partial v}{\partial y} & \mu\left(\frac{\partial v}{\partial z}+\frac{\partial w}{\partial y}\right) \\ \mu\left(\frac{\partial w}{\partial x}+\frac{\partial u}{\partial z}\right) & \mu\left(\frac{\partial w}{\partial y}+\frac{\partial v}{\partial z}\right) & 2\mu\frac{\partial w}{\partial z} \end{bmatrix} \tag{117}$$

Substituting these into the three cartesian components of the Cauchy's equation (108):

$$\rho\frac{Du}{Dt} = -\frac{\partial P}{\partial x} + \rho g_x + 2\mu\frac{\partial^2 u}{\partial x_2} + \mu\frac{\partial}{\partial y}\left(\frac{\partial u}{\partial y} + \frac{\partial v}{\partial x}\right) + \mu\frac{\partial}{\partial z}\left(\frac{\partial u}{\partial z} + \frac{\partial w}{\partial x}\right)$$

(118)

$$\rho\frac{Dv}{Dt} = -\frac{\partial P}{\partial y} + \rho g_y + \mu\frac{\partial}{\partial x}\left(\frac{\partial v}{\partial x} + \frac{\partial u}{\partial y}\right) + 2\mu\frac{\partial^2 v}{\partial y^2} + \mu\frac{\partial}{\partial z}\left(\frac{\partial v}{\partial z} + \frac{\partial w}{\partial y}\right)$$

(119)

$$\rho\frac{Dw}{Dt} = -\frac{\partial P}{\partial z} + \rho g_z + \mu\frac{\partial}{\partial x}\left(\frac{\partial w}{\partial x} + \frac{\partial u}{\partial z}\right) + \mu\frac{\partial}{\partial y}\left(\frac{\partial w}{\partial y} + \frac{\partial v}{\partial z}\right) + 2\mu\frac{\partial^2 w}{\partial z^2}$$

(120)

Notice that since pressure consists of normal stress only, it contributes only one term these equations. However, since the viscous stress tensor consists of both normal and shear stresses, it contributes three terms.

Since the velocity components are smooth functions of x, y and z, the order of differentiation is irrelevant, therefore, after some rearrangements equations (118)-(120):

$$\begin{aligned}\rho\frac{Du}{Dt} &= -\frac{\partial P}{\partial x} + \rho g_x + \mu\left[\frac{\partial^2 u}{\partial x^2} + \frac{\partial}{\partial x}\frac{\partial u}{\partial x} + \frac{\partial}{\partial x}\frac{\partial v}{\partial y} + \frac{\partial^2 u}{\partial y^2} + \frac{\partial}{\partial x}\frac{\partial w}{\partial z} + \frac{\partial^2 u}{\partial z^2}\right] \\ &= \frac{\partial P}{\partial x} + \rho g_x + \mu\left[\frac{\partial}{\partial x}\left(\frac{\partial u}{\partial x} + \frac{\partial v}{\partial y} + \frac{\partial w}{\partial z}\right) + \frac{\partial^2 u}{\partial x^2} + \frac{\partial^2 u}{\partial y^2} + \frac{\partial^2 u}{\partial z^2}\right]\end{aligned}$$

(121)

$$\begin{aligned}\rho\frac{Du}{Dt} &= -\frac{\partial P}{\partial y} + \rho g_y + \mu\left[\frac{\partial^2 v}{\partial x^2} + \frac{\partial}{\partial y}\frac{\partial u}{\partial x} + \frac{\partial}{\partial y}\frac{\partial v}{\partial y} + \frac{\partial^2 v}{\partial y^2} + \frac{\partial}{\partial y}\frac{\partial w}{\partial z} + \frac{\partial^2 v}{\partial z^2}\right] \\ &= \frac{\partial P}{\partial y} + \rho g_y + \mu\left[\frac{\partial}{\partial y}\left(\frac{\partial u}{\partial x} + \frac{\partial v}{\partial y} + \frac{\partial w}{\partial z}\right) + \frac{\partial^2 v}{\partial x^2} + \frac{\partial^2 v}{\partial y^2} + \frac{\partial^2 v}{\partial z^2}\right]\end{aligned}$$

(122)

$$\begin{aligned}\rho\frac{Du}{Dt} &= -\frac{\partial P}{\partial z} + \rho g_z + \mu\left[\frac{\partial^2 w}{\partial x^2} + \frac{\partial}{\partial z}\frac{\partial u}{\partial x} + \frac{\partial}{\partial z}\frac{\partial v}{\partial y} + \frac{\partial^2 w}{\partial y^2} + \frac{\partial}{\partial z}\frac{\partial w}{\partial z} + \frac{\partial^2 w}{\partial z^2}\right] \\ &= \frac{\partial P}{\partial z} + \rho g_z + \mu\left[\frac{\partial}{\partial z}\left(\frac{\partial u}{\partial x} + \frac{\partial v}{\partial y} + \frac{\partial w}{\partial z}\right) + \frac{\partial^2 w}{\partial x^2} + \frac{\partial^2 w}{\partial y^2} + \frac{\partial^2 w}{\partial z^2}\right]\end{aligned}$$

(123)

The term in round parenthesis is zero for incompressible flows because of the continuity equation for incompressible flow. The last three terms of each equation are the Laplacian of the correspondent velocity component (u, v or w) in Cartesian coordinates. Therefore the three components of the momentum equation can be written as:

$$\rho\frac{Du}{Dt} = -\frac{\partial P}{\partial x} + \rho g_x + \mu\nabla^2 u$$

(124)

$$\rho\frac{Du}{Dt} = -\frac{\partial P}{\partial y} + \rho g_y + \mu\nabla^2 v$$

(125)

$$\rho\frac{Du}{Dt} = -\frac{\partial P}{\partial z} + \rho g_z + \mu\nabla^2 w$$

(126)

Finally, combining the three components into one vector equation results in the Navier-Stokes (NS) equation for incompressible flow with constant viscosity.

$$\rho\frac{D\vec{V}}{Dt} = -\vec{\nabla}P + \rho\vec{g} + \mu\nabla^2\vec{V}$$

(127)

The equation (127) is an unsteady, non-linear, second-order, partial differential equation. It has four unknows (three velocity components and pressure), yet it represents only three equations. The fourth equation is the incompressible continuity equation:

$$\frac{\partial u}{\partial x} + \frac{\partial v}{\partial y} + \frac{\partial w}{\partial z} = 0 \tag{128}$$

The incompressible NS equation can be represented per each direction in the form:

$$\rho\left(\frac{\partial u}{\partial t} + u\frac{\partial u}{\partial x} + v\frac{\partial u}{\partial y} + w\frac{\partial u}{\partial z}\right) = -\frac{\partial P}{\partial x} + \rho g_x + \mu\left(\frac{\partial^2 u}{\partial x^2} + \frac{\partial^2 u}{\partial y^2} + \frac{\partial^2 u}{\partial z^2}\right) \tag{129}$$

$$\rho\left(\frac{\partial v}{\partial t} + u\frac{\partial v}{\partial x} + v\frac{\partial v}{\partial y} + w\frac{\partial v}{\partial z}\right) = -\frac{\partial P}{\partial y} + \rho g_y + \mu\left(\frac{\partial^2 v}{\partial x^2} + \frac{\partial^2 v}{\partial y^2} + \frac{\partial^2 v}{\partial z^2}\right) \tag{130}$$

$$\rho\left(\frac{\partial w}{\partial t} + u\frac{\partial w}{\partial x} + v\frac{\partial w}{\partial y} + w\frac{\partial w}{\partial z}\right) = -\frac{\partial P}{\partial z} + \rho g_z + \mu\left(\frac{\partial^2 w}{\partial x^2} + \frac{\partial^2 w}{\partial y^2} + \frac{\partial^2 w}{\partial z^2}\right) \tag{131}$$

Annexe B: Womersley pulsatile flow

The blood flow in the heart and arteries is quite pulsatile, meaning that the flow has a periodic behaviour and a net directional motion over the cycle (i.e., the average flow is > 0). When the heart contracts during systole, a pressure originates from the left ventricle and travels out as a wave driven by the arteries' elasticity. The most immediate consequence of the heart contraction is that the pressure in the left ventricle (upstream) exceeds that in the aorta (downstream) resulting in the opening of the aortic valve and the blood being ejected from the heart. The pulsatile nature of blood flow also affects the pressure distribution out into the vessels, the velocity profiles within them and the point of transition from a laminar to a turbulent regime. This later effect is since flow accelerates rapidly in early systole, when, based on the instantaneous Reynolds number in the ascending aorta, the blood flow would be expected to be turbulent during a significant part of systole.

In the tube seen for Section 2.2.2.2, if the flow is pulsatile, the partial derivative of velocity u concerning time is not zero. Moreover, the partial derivative of pressure P with respect to distance along the tube x is non-zero. These were the necessary conditions for Poiseuille's law. Therefore, Poiseuille flow is no longer a reasonable estimate for the case of pulsatile flow.

To estimate flow from a pulsatile driving pressure in rigid tubes, a Newtonian fluid, uniform, laminar, axially symmetric, pipe flow, similar to the Poiseuille flow problem is assumed. However, considering pulsatile flow rather than steady now.

Considering the unsteady Navier-Stokes equations

$$\begin{cases} \dfrac{\partial u}{\partial t} - v\Delta u + (u \bullet \nabla)u + \nabla p = f & \text{in } \Omega_\Gamma \equiv \Omega \times (0,\infty) \\ div\, u = 0 & \text{in } \Omega_\Gamma \end{cases} \tag{132}$$

Where $\Omega \equiv (0,1) \times (0,1)$ with boundary conditions

$$u = 0 \text{ on } \Gamma_D \tag{133}$$

$$pn - v\nabla u \bullet n = -2v\sin(\omega t)n \text{ on } \Gamma_{N1} \tag{134}$$

$$pn - v\nabla u \bullet n = 0 \text{ on } \Gamma_{N2} \tag{135}$$

With initial condition $u_0 = 0$, where Γ_D is given by the sides $x_2 = 0$ and $x_2 = 1$ (with $0 \le x_2 \le 1$), Γ_{N1} is the boundary $\{x_1 = 0, 0 \le x_2 \le 1\}$, Γ_{N2} is the boundary $\{x_1 = 1, 0 \le x_2 \le 1\}$ and n is the outward normal unit vector to $\partial\Omega$.

Considering $u_2 = 0$, the second component of the momentum reduces to $\frac{\partial p}{\partial x_2} = 0$, so that p is only a function of x_1. Continuity equation yields $\frac{\partial u_1}{\partial x_1} = 0$, so u_1 is a function only of x_2.

The first equation, the momentum equation, can be written as:

$$\frac{\partial u_1}{\partial t} - \nu \frac{\partial^2 u_1}{\partial x_2^2} = -\frac{\partial p}{\partial x_1} \tag{136}$$

Since pressure is a linear function of x_1, $\frac{\partial p}{\partial x_1}$ is constant in space and amounts to the difference between outlet and inlet pressure divided by the length of the domain, i.e.

$$\frac{\partial p}{\partial x_1} = -2\nu \sin(\omega t) \tag{137}$$

First momentum equation reduces then to:

$$\frac{\partial u_1}{\partial t} - \nu \frac{\partial^2 u_1}{\partial x_2^2} = 2\nu \sin(\omega t) \tag{138}$$

Expanding the solution $u_1(x_2, t)$ defined in a bounded interval of the independent variable x_2 as a Fourier Series,

$$u_1(x_2, t) = \sum_{k=0}^{\infty} \gamma_k(t) \sin(k\pi x_2) \tag{139}$$

The first momentum equation gives

$$\sum_{k=0}^{\infty} \frac{\partial \gamma_k(t)}{\partial t} \sin(k\pi x_2) + \nu \sum_{k=0}^{\infty} k^2 \pi^2 \gamma_k \sin(k\pi x_2) = 2\nu \sin(\omega t) \tag{140}$$

Sinusoidal functions are orthogonal with respect to the L^2 scalar product, for any integer l and m. Multiplying for $\sin(l\pi x_2)$ for any integer l and integrate over $0 \le x_2 \le 1$, by the orthogonality of sinusoidal functions and assuming:

$$\int_0^1 \sin(l\pi x_2) dx_2 = \begin{cases} 0 & \text{for } l \text{ even,} \\ \dfrac{2}{l\pi} & \text{for } l \text{ odd} \end{cases} \tag{141}$$

We get a decoupled system of ordinary differential equations in the form

$$\gamma_l' + \nu l^2 \pi^2 \gamma_{2k+1} = \begin{cases} 0 & \text{for } l \text{ even,} \\ \dfrac{8\nu}{l\pi} \sin(\omega t) & \text{for } l \text{ odd} \end{cases} \tag{142}$$

With initial conditions $\gamma_l(0) = 0$ since $u_1(x_2, 0) = 0$. For l even,

$$\gamma' + b\gamma = 0 \tag{143}$$

With $b = \nu l^2 \pi^2$. General solution $\gamma = Ce^{-bt}$ reduces to $\gamma = 0$ due to the initial condition.
For l odd,

$$\gamma' + b\gamma = A\sin(\omega t) \tag{144}$$

With $A = \frac{8v}{l\pi}$. The general solution for this type of equations is given by summing a particular solution to the general solution of the homogeneous problem. The right-hand side gives the particular solution:

$$\gamma_{part} = \alpha \sin \omega t + \beta \cos \omega t \tag{145}$$

We have then

$$(\alpha\omega + b\beta)\cos(\omega t) + (b\alpha - \beta\omega)\sin(\omega t) = A\sin(\omega t) \tag{146}$$

Therefore,

$$\begin{cases} \alpha\omega + b\beta = 0 \\ b\alpha - \beta\omega = A \end{cases} \tag{147}$$

$$\alpha = \frac{Ab}{b^2 + \omega^2} \tag{148}$$

$$\beta = -\frac{A\omega}{b^2 + \omega^2} \tag{149}$$

$$\gamma' + b\gamma = A\sin(\omega t) \leftrightarrow \gamma = Ce^{-bt} + \frac{Ab}{b^2 + \omega^2}\sin(\omega t) - \frac{A\omega}{b^2 + \omega^2}\cos(\omega t) \tag{150}$$

For the initial condition,

$$C = \frac{A\omega}{b^2 + \omega^2} \tag{151}$$

$$\gamma = \frac{A}{b^2 + \omega^2}\left(\omega e^{-bt} - \omega\cos(\omega t) + \frac{Ab}{b^2 + \omega^2}\right)\sin(\omega t) \tag{152}$$

Finally,

$$u_1 = \sum_{k=0}^{\infty} \gamma_{2k+1}(t)\sin\left((2k+1)\pi x_2\right) \tag{153}$$

Using

$$\gamma_{2k+1} = -8\,v\,\frac{\omega e^{\left(-v(2k+1)^2\pi^2\right)t} - \omega\cos(\omega t) + v(2k+1)^2\pi^2\sin(\omega t)}{\left(v^2(2k+1)^4\pi^4 + \omega^2\right)(2k+1)\pi} \tag{154}$$

Which is the unsteady counterpart of the Poiseuille's Law for a constant in space and sinusoidal-in-time pressure drop and takes the name of 2D Womersley solution.[26] [51]

Annexe C: Full derivation in 1D of the FEM

To illustrate the FEM, consider the following partial differential equation:

$$-\frac{d}{dx}\left(EA\frac{du}{dx}\right) = f \quad \text{in } \Omega \in [0,L] \tag{155}$$

With boundary conditions

$$u(0) = 0 \tag{156}$$

$$E\frac{du}{dx}(L) = g \tag{157}$$

Assuming $E = 0.1, A = 1, L = 1, f = 1$ and $g = 0.001$, one has:

$$-0.1\frac{d^2u(x)}{dx^2} = 1 \quad \text{in } \Omega \in [0,1] \tag{158}$$

$$u(0) = 0 \tag{159}$$

$$0.1\frac{du(x)}{dx} = 0.001$$

$$0.1\frac{du(x)}{dx} = 0.001 \tag{160}$$

Considering also a mesh with n = 3 elements $\big((x_1, x_2), (x_2, x_3), (x_3, x_4)\big)$ and four nodes (x_1, x_2, x_3, x_4).

The mesh is uniform, therefore $h = \frac{L}{n} = \frac{1}{3}$.

The piecewise functions will be given by:

$$\phi_1 = \begin{cases} \dfrac{\frac{1}{3} - x}{h} & \text{if } 0 \le x < \dfrac{1}{3} \\ 0 & \text{otherwise} \end{cases} \qquad \phi'_1 = \begin{cases} \dfrac{1}{h} & \text{if } 0 \le x < \dfrac{1}{3} \\ 0 & \text{otherwise} \end{cases}$$

$$\phi_2 = \begin{cases} \dfrac{x}{h} & \text{if } 0 \le x < \dfrac{1}{3} \\ \dfrac{\frac{2}{3} - x}{h} & \text{if } \dfrac{1}{3} \le x < \dfrac{2}{3} \\ 0 & \text{otherwise} \end{cases} \qquad \phi'_2 = \begin{cases} \dfrac{1}{h} & \text{if } 0 \le x < \dfrac{1}{3} \\ -\dfrac{1}{h} & \text{if } \dfrac{1}{3} \le x < \dfrac{2}{3} \\ 0 & \text{otherwise} \end{cases}$$

$$\phi_3 = \begin{cases} \dfrac{x - \frac{1}{3}}{h} & \text{if } \dfrac{1}{3} \le x < \dfrac{2}{3} \\ \dfrac{1 - x}{h} & \text{if } \dfrac{2}{3} \le x < 1 \\ 0 & \text{otherwise} \end{cases} \qquad \phi'_3 = \begin{cases} \dfrac{1}{h} & \text{if } \dfrac{1}{3} \le x < \dfrac{2}{3} \\ -\dfrac{1}{h} & \text{if } \dfrac{2}{3} \le x < 1 \\ 0 & \text{otherwise} \end{cases}$$

$$\phi_4 = \begin{cases} \dfrac{x - 1}{h} & \text{if } \dfrac{2}{3} \le x < 1 \\ 0 & \text{otherwise} \end{cases} \qquad \phi'_4 = \begin{cases} \dfrac{1}{h} & \text{if } \dfrac{2}{3} \le x < 1 \\ 0 & \text{otherwise} \end{cases}$$

Since our mesh is uniform $h_i = h$, one has:

$$A = \begin{bmatrix} \dfrac{1}{h} + \dfrac{1}{h} & -\dfrac{1}{h} & 0 & 0 \\ -\dfrac{1}{h} & \dfrac{1}{h} + \dfrac{1}{h} & -\dfrac{1}{h} & 0 \\ 0 & -\dfrac{1}{h} & \dfrac{1}{h} + \dfrac{1}{h} & -\dfrac{1}{h} \\ 0 & 0 & -\dfrac{1}{h} & \dfrac{1}{h} + \dfrac{1}{h} \end{bmatrix} = \dfrac{1}{h}\begin{bmatrix} 2 & -1 & 0 & 0 \\ -1 & 2 & -1 & 0 \\ 0 & -1 & 2 & -1 \\ 0 & 0 & -1 & 2 \end{bmatrix} = 3\begin{bmatrix} 2 & -1 & 0 & 0 \\ -1 & 2 & -1 & 0 \\ 0 & -1 & 2 & -1 \\ 0 & 0 & -1 & 2 \end{bmatrix} \tag{161}$$

$$F = f \times \dfrac{h}{2}\begin{bmatrix} 1 \\ 2 \\ 2 \\ 1 \end{bmatrix} + g\begin{bmatrix} 0 \\ 0 \\ 0 \\ 1 \end{bmatrix} = \begin{bmatrix} \dfrac{h}{2} \\ h \\ h \\ \dfrac{h}{2} + g \end{bmatrix} \tag{162}$$

Finally, the discretization of the equation (155) results in the following linear system, where U is the matrix of the unknown velocities in each node:

$$AU = F \Leftrightarrow 3\begin{bmatrix} 2 & -1 & 0 & 0 \\ -1 & 2 & -1 & 0 \\ 0 & -1 & 2 & -1 \\ 0 & 0 & -1 & 2 \end{bmatrix}\begin{bmatrix} u_1 \\ u_2 \\ u_3 \\ u_4 \end{bmatrix} = \begin{bmatrix} \dfrac{h}{2} \\ h \\ h \\ \dfrac{h}{2} + g \end{bmatrix} \tag{163}$$

Annexe D: Parameters used in COMSOL Multiphysics® for Section 3.2

Table 24: Parameters defined in the Global node.

Parameter	Description	Expression
ρ_{blood}	Blood density	$\rho_{blood} = 1060\ kg \cdot m^{-3}$
μ_{blood}	Blood viscosity	$\mu_{blood} = 0.004\ Pa \cdot s$
V_{max}	Maximum velocity at T_{inlet}	Measured in the patient
V_{mean}	Average velocity at T_{inlet}	$V_{mean} = \dfrac{V_{max}}{2}$
A_{inlet}	Area of the cross-section of T_{inlet}	Measured in the geometry
A_{DA}	Area of the cross-section of T_{DA}	Measured in the geometry
A_{BA}	Area of the cross-section of T_{BA}	Measured in the geometry
A_{LCA}	Area of the cross-section of T_{LCA}	Measured in the geometry
A_{LSA}	Area of the cross-section of T_{LSA}	Measured in the geometry
D_{inlet}	Diameter of the cross-section of T_{inlet}	Measured in the geometry
D_{DA}	Diameter of the cross-section of T_{DA}	$D_{DA} = \sqrt{\dfrac{4 \times A_{DA}}{\pi}}$
D_{BA}	Diameter of the cross-section of T_{BA}	$D_{BA} = \sqrt{\dfrac{4 \times A_{BA}}{\pi}}$
D_{LCA}	Diameter of the cross-section of T_{LCA}	$D_{LCA} = \sqrt{\dfrac{4 \times A_{LCA}}{\pi}}$
D_{LSA}	Diameter of the cross-section of T_{LSA}	$D_{LSA} = \sqrt{\dfrac{4 \times A_{LSA}}{\pi}}$
Re	Reynold's number	$Re = \dfrac{\rho \times V_{max} \times D_{inlet}}{\mu}$